TECHNISCHE UNIVERSITÄT WIEN
Vienna University of Technology

GEOWISSENSCHAFTLICHE MITTEILUNGEN

Heft Nr. 94, 2013

Atmospheric effects on measurements of the Earth gravity field

Maria Karbon

Veröffentlichung des Departments für Geodäsie und Geoinformation
ISSN 1811-8380

Schriftenreihe der Studienrichtung VERMESSUNG UND GEOINFORMATION

TECHNISCHE UNIVERSITÄT WIEN
Vienna University of Technology

GEOWISSENSCHAFTLICHE MITTEILUNGEN

Heft Nr. 94, 2013

Atmospheric effects on measurements of the Earth gravity field

Maria Karbon

Veröffentlichung des Departments für Geodäsie und Geoinformation
ISSN 1811-8380

Schriftenreihe der Studienrichtung VERMESSUNG UND GEOINFORMATION

2013
Published by the Department of Geodesy and Geoinformation
of the Vienna University of Technology
Gußhausstraße 27-29
1040 Vienna, Austria

Responsible for this issue: Prof. Dr. Johannes Böhm
Printed by: Grafisches Zentrum HTU GmbH

The digital version of the full document with colored figures is available online:
http://www.ub.tuwien.ac.at/diss/AC07815618.pdf

Die Kosten für den Druck wurden vom Department für Geodäsie und Geoinformation übernommen.

Diese Arbeit wurde an der Fakultät für Mathematik und Geoinformation der Technischen Universität Wien zur Erlangung des akademischen Grades einer Doktorin der technischen Wissenschaften eingereicht.

Begutachter:

Prof. Dr. Harald Schuh
Department für Geodäsie und Geoinformation der Technischen Universität Wien
Gußhausstraße 27-29, 1040 Vienna, Austria
Department 1 „Geodäsie und Fernerkundung", Deutsches Geoforschungszentrum GFZ
Telegrafenberg, 14473 Potsdam, Germany

Prof. Dr. Frank Flechtner
Section 1.2, Global Geomonitoring and Gravity Field
Helmholtz Centre Potsdam
GFZ German Research Centre for Geosciences
Oberpfaffenhofen, Germany

Tag der mündlichen Prüfung: 12.04.2013

Auflage: 50 Stück

ISSN 1811-8380

Dissertation committee:

Prof. Dr. Georg Gartner
Vienna University of Technology

Prof. Dr. Harald Schuh
GFZ German Research Centre for Geosciences

Prof. Dr. Frank Flechtner
GFZ German Research Centre for Geosciences

Ao.Prof. Dr. Bruno Meurers
University of Vienna

Acknowledgments

I want to express my deepest gratitude to my principal supervisor, Harald Schuh, for his continuous support, guidance, and patience throughout my studies and on this research. I want to thank him for enabling me to present my work at numerous international conferences, allowing me to get into contact with the community and gain further insight into the current research as well as getting new inspiration for my own work.

My great appreciation goes to the other members of my dissertation committee, Frank Flechtner and Bruno Meurers. I thank them for their advices during my studies, for their time, valuable suggestions, and inspiring comments to improve this draft. Special thanks go to Frank Flechtner as second assessor of this work, as he managed to find the time and peace of mind to review this thesis and ensure its correctness and completeness. To Bruno Meurers as he provided me SG data, permitting me to add a highly valuable aspect to this work.

I am truly indebted and thankful to my co-supervisor Johannes Böhm, for his valuable insight and his always open door. He provided great help and valuable discussions as well as a good climate within our project-group. Im obliged to him as well as to Dudy Wijaia and Mischael Schindelegger, who contributed to this work in various ways. Further thanks go to Johannes Böhm for his efforts to bridge the gap between my quite isolated gravity-island at TU Vienna to other groups and persons working on this topic.

My most profound thanks go to my family for their continuous support, encouragement and their solidarity during so many years of study. I am especially thankful for their understanding and the tacit acceptance of my repeated absence from family affairs.

Finally, I acknowledge the Austrian Science Fund (FWF) for their support within the project GGOS-Atmosphere (P20902).

Abstract

Atmospheric pressure variations are one of the major sources of surface gravity perturbations. The varying atmosphere introduces two disturbing forces in the gravity signal, the so called direct effect or Newtonian attraction, where the measuring object is attracted by the atmospheric mass itself, and secondly the indirect effect or atmospheric loading, where the masses deform the Earths surface, what again influences the measured gravity signal due to the slightly changes gravity field.

In satellite gravity missions such signals are referred to as aliasing. To eliminate them, the determination of accurate atmospheric gravity field coefficients (AGC) is indispensable. For the determination of AGC it is state of the art to use high resolution numerical weather models which take into account the time-variable three-dimensional distribution of the atmospheric mass. By subtracting the gravity spherical harmonics of the instantaneous atmosphere from the ones of a long term mean field, the residual gravity spherical harmonic series is obtained. It describe the deviation of the actual gravity field from the mean gravity field due to atmospheric mass variations.

Ground based gravimetric measurements encounter the same difficulty of eliminating the disturbing signal introduced by the atmosphere. Superconducting gravimeters are usually corrected using the local air pressure, which reduces up to 90-95 % of the atmospheric signal. However, modern superconducting gravimeters require an even better atmospheric correction if small signals are to be identified. For this task the use of three-dimensional modeling of atmospheric mass attraction based on operational numerical weather models has shown promising results.

Kurzfassung

Druckvariationen in der Erdatmosphäre sind eine der Hauptverursacher von Schwerefeldänderungen an der Oberfläche. Die sich stetig ändernde Atmosphäre beeinflusst das Schweresignal auf zweierlei Art, einerseits durch Attraktion des Messinstrumentes durch die atmosphärischen Massen, das ist der sogenannte direkte Effekt, und durch die von den atmosphärischen Massen induzierte Verformung der Erdoberfläche und daraus resultierenden Schwereänderungen, den indirekten Effekt.

In der Satellitengravimetrie werden diese kurzzeitige Signale als Aliasing bezeichnet. Um diese zu eliminieren ist die Bestimmung von exakten atmosphärischen Schwerefeld-Koeffizienten (AGC) unverzichtbar. Für die Bestimmung von AGC werden entsprechend dem Stand der Technik hochauflösende numerische Wettermodelle verwendet, welche die zeitvariable drei-dimensionale Massenverteilung innerhalb der Atmosphäre berücksichtigen. Durch Subtraktion der Kugelflächenfunktionen der momentanen Atmosphäre von denen des mittleren Zustands, einem lanzeitigen Mittel, werden die verbleibenden Kugelfunktionen ermittelt. Diese beschreiben die Abweichung des momentanen Schwerefeldes vom mittleren Schwerefeld aufgrund atmosphärischer Massenveränderungen.

Bodenbasierte Schweremessungen begegnen denselben Schwierigkeiten bei der Eliminierung des Störsignals welches durch die Atmosphäre induziert wird. Bei supraleitenden Gravimetern wird die Korrektur üblicherweise über den lokalen Luftdruck ermittelt, wodurch 90-95 % des Atmosphärensignals eliminiert wird. Allerdings reicht diese Korrektur heutzutage nicht mehr aus, da auf die Detektion von sehr schwachen Signalen abgezielt wird. Hier hat die drei-dimensionale Modellierung von atmosphärischer Massenattraktion auf Basis von numerischen Wettermodellen vielversprechende Ergebnisse gezeigt.

Contents

1 Introduction **11**

1.1 Motivation 11

1.2 Outline of the study 13

1.3 Organization of the thesis 14

2 The gravity field of the Earth **15**

2.1 Theory of the gravity field 15

2.1.1 Gravity potential and gravity acceleration 15

2.1.2 Gravity field of the Earth 17

2.1.3 Spherical harmonics 21

2.2 Determination of the Earth gravity field 23

2.2.1 The theories of Bruns and Stokes' formula 23

2.2.2 Terrestrial gravity determination 26

2.2.3 Satellite based gravity determination 33

2.3 Temporal variation of the Earth's gravity field 40

2.3.1 The gravity constant and Earth rotation 42

2.3.2 Gravitational tides of the solid Earth 42

2.3.3 Earth tides 44

2.3.4 Ocean loading tides 46

2.3.5 Mass changes in the System Earth 46

3 Atmospheric effects on the gravity field of the Earth **49**

3.1 Physical and meteorological fundamentals 49

3.1.1 Structure of the atmosphere 49

3.1.2 Pressure, temperature, density and height 50
3.1.3 The atmospheric pressure and its variation 52
3.2 Meteorological analysis-models 56
3.2.1 Numerical weather models 56
3.2.2 Topographical effects on the surface pressure 58
3.2.3 The mean state of the atmosphere 60
3.2.4 Error estimation 61
3.3 Impact of the pressure variation on the gravity field 62
3.3.1 Atmospheric aliasing 63
3.3.2 Atmospheric tides 64
3.3.3 Atmospheric loading and the indirect effect 65
3.4 The atmosphere and the ocean 66

4 Mathematical description of the de-aliasing model for GRACE and its validation 69
4.1 A glimpse into GRACE data analyses 70
4.2 Data processing 71
4.3 From atmosphere to gravity 75
4.3.1 Thin layer approximation 76
4.3.2 3D Atmosphere 77
4.3.3 Indirect effect 78
4.4 Validation and interpretation 78
4.4.1 Impact of constant gravity and mean radius a 79
4.4.2 Thin layer versus vertical integration and the effects of the mean field 81
4.4.3 Impact of atmospheric loading and atmospheric tides 84
4.4.4 Comparison of different NWM 86
4.4.5 Comparison of different de-aliasing products 93
4.4.6 Atmosphere and gradients 96

5 Atmospheric corrections for superconducting gravimeters 101
5.1 Conventional models and new approaches 101
5.1.1 Admittance models 102
5.1.2 Atmospheric Green's functions 104

5.1.3 Geometrical approach 106
5.1.4 ATMACS 108
5.1.5 Atmospheric Gravity Coefficients for SG 109
5.1.6 Elastic contribution 109
5.2 Comparison of the methods and models 110
5.2.1 SG stations and data 110
5.2.2 Comparison of the surface pressure data 111
5.2.3 Comparison of different models 112
5.2.4 Impact of the vertical expansion of the atmosphere 115

6 Summary, conclusions and outlook **117**

Chapter 1

Introduction

1.1 Motivation

The Earth is a dynamic system where different geophysical processes interact resulting in variations with a wide temporal and spatial range, making the study of it a complicated interdisciplinary task. Modeling and separating all the physical processes, including atmospheric and oceanic circulations, redistribution of continental water, ice melting, precipitation, sea level change, global isostatic adjustment, luni-solar tides, and plate tectonics, are a necessity to study one specific process and further to gain deeper understanding of the evolution of each sub-system and their interactions. In the last years one process in particular has caught the attention of many scientists, i.e. the mass redistribution and transfer of water, as it is crucial in understanding the evolution of our climate and the sea level. This signal is directly linked to mass changes in the Earth system, which become visible as gravity variations and can be measured on specific locations on the Earth surface by gravimeter or on a global scale by satellite gravity missions.

The connection between atmospheric pressure and gravity was demonstrated first by Warburton and Goodkind (1977) using superconducting gravimeters (SG). With the development of the Satellite Laser Ranging (SLR) technique in the 60's and then especially with the long-term Lageos observations since the mid 70's, the detection of temporal variations of the low degrees of the spherical harmonic coefficients of the gravity field on a global scale, especially of the geocenter, was possible. Also here the high correlation with the mass

redistribution in the atmosphere, ocean and continental water was confirmed. Since then the global SG network was constantly expanded and three dedicated satellite gravity missions where realized. The first was CHAMP (Challenging Minisatellite Payload) launched in 2000 which reached its end in September 2010. CHAMP was dedicated, besides studying the magnetic field and the atmosphere, to derive a precise static gravity field. The second is GRACE (Gravity Recovery and Climate Experiment), launched in 2002 and still in orbit, designed to detect for the first time variations in the mass flux at wavelength of 300 km or longer. At NASA it is considered to be one of the most important satellite missions in the last decade. The most recent one is GOCE (Gravity field and steady-state Ocean Circulation Explorer), launched in 2009, equipped with a gradiometer to detect the short wavelength of the static gravity field, and thus allowing the determination of the global geoid with high spatial resolution.

What the satellite gravity missions as well the SG detect, is a combined gravity signal from all processes that can perturb the satellites orbit or the gravimeter observation respectively. After removing non-gravitational effects, such as atmospheric drag or solar radiation pressure, the measurements still include various tidal effects (solid Earth, ocean, atmosphere and pole tides), non-tidal atmospheric, oceanic and hydrological variations, postglacial rebound, ice sheet and glacier mass balance, other unmodeled processes or signals, and noise. To obtain any individual contribution, independent knowledge in form of background models is required to separate these signals. Additionally, as the measurement techniques evolve and gain in accuracy, also these background models have be updated up and improved.

The dynamic atmospheric circulation is the most rapidly changing and currently the best measured fluid within the Earths subsystems. Several agencies such as the European Center for Medium-range Weather Forecast (ECMWF) provide Numerical Weather Models (NWM) to reconstruct the current state of the atmosphere and project it into the future (hours to weeks). From such models the atmospheric pressure change can be obtained and introduced as background model for the tidal and non-tidal contribution, during the data processing. Consequently, the unmodeled signals (e.g. from hydrology) along with mis-modeled components in the background models are contained in the estimated gravity

solution. Therefore accurate atmospheric pressure information is very crucial to improve the quality of these models; any error or uncertainty left in the atmospheric correction model will inevitably leak into and deteriorate the hydrological or other derived signals of interest.

1.2 Outline of the study

In 2009 the project 'GGOS Atmosphere', funded by the Austrian Science Fund (FWF), at the Institute of Geodesy and Geophysics (IGG) of TU Wien (`http://ggosatm.hg.tuwien.ac.at/`) was established, with the overall goal of determining consistent and homogeneous models for atmospheric angular momentum, atmospheric pressure loading corrections, atmospheric gravity field coefficients (AGC), and troposphere delays of radio signals, all based on a common data stream with predominantly the same underlying meteorological parameters like pressure, temperature, humidity, and wind velocity. This perfectly corresponds to one of the major objectives of the Global Geodetic Observing System (GGOS), the flagship component of the International Association of Geodesy (IAG): 'GGOS focuses on all aspects to ensure the consistency of geometric and gravimetric products.' (Drewes and Reigber, 2005). The main focus of this thesis will therefore be the model for calculating the effect of the atmosphere on the Earth's gravity field, i.e. the atmospheric gravity field coefficients (AGC).

One emphasis will be the processing of the meteorological data, and the discussion on its advantages with respect to using the raw NWM data. The main difficulty when working with meteorological data is the inconsistency of the models from different providers regarding temporal and spatial resolution and assimilation procedures. Furtheron, the models supplied by one provider can differ significantly and even change with time. Paying special attention to that problem a processing strategy was developed which allows to be independent to any changes within the NWM, especially regarding the topography. The algorithms used to generate our meteorological fields as well as the mean field of the atmosphere which is essential for our studies will be described in detail.
Further a detailed mathematical description of the atmospheric de-aliasing model is given

and evaluated. Thanks to our processing strategy for the meteorological data, we can abandon approximations such as the Earth as a sphere and have consistent gravity acceleration values available. This makes it possible to use a more direct approach for the calculation of the AGC. Internal validations using different approaches and NWM data, as well as external with de-aliasing products provided by other centers are carried out, revealing benefits and weaknesses concerning todays GRACE processing but also giving a heads-up for future reprocessing and missions.

The second part focuses on atmospheric correction for superconducting gravimeters (SG) and the application of AGC as an alternative approach. The most commonly used methods for atmospheric corrections will be introduced and compared to the performance of the AGC on the example of two SG stations. Additionally to a ground proof of the AGC originally developed for satellite missions, it was possible to supply an alternative product available on a global scale making full use of the biggest advantage of NWM.

1.3 Organization of the thesis

The rest of the thesis is organized as follows: Chapter 2 introduces the basics of the theory of the gravity field, including the determination of the Earth gravity field as well as a discussion of the various temporal variations of gravity field.

In Chapter 3 the role of the atmosphere in the determination of the Earth gravity field will be discussed in detail, giving an overview of the atmosphere's structure, state of the art NWM and the various effects of the atmosphere on gravity.

Chapter 4 provides the processing strategy used for the meteorological data as well as a detailed mathematical description of the de-aliasing model. Its internal validation and comparisons with external models is also provided here.

Chapter 5 addresses the methods for atmospheric corrections used for SG and introduces the AGC as an alternative approach. The performance of AGC will be compared and validated in regard to the better established traditional approaches used in the SG processing.

Chapter 6 summarizes the results and the conclusions in this study, along with a discussion and outlook.

Chapter 2

The gravity field of the Earth

2.1 Theory of the gravity field

The purpose of this section is to introduce the fundamentals of the potential theory, i.e. gravity acceleration and gravity potential with their most important relationships. Also an introduction to spherical harmonics is given. The following information can be found in more detail in Torge (1989) and Hofmann-Wellenhof and Moritz (2005).

2.1.1 Gravity potential and gravity acceleration

According to Newton's law of gravitation, two masses m_1 and m_2 separated by a distance r attract each other with a force

$$\vec{F} = G\frac{m_1 m_2}{r^2}\vec{r}_0\,, \tag{2.1}$$

where $G = 6.6742 \cdot 10^{-11}$ m^3 kg^{-1} s^{-2} is the gravitational constant and $\vec{r}_0$ the unit vector between mass m_1 and mass m_2 (Hofmann-Wellenhof and Moritz, 2005). By setting one mass to unity and denoting the attracting mass with m, we express the force $\vec{F}$ exerted by the mass m on a unit mass at location P and distance r as

$$\vec{F} = G\frac{m}{r^2}\vec{r}_0\,. \tag{2.2}$$

This representation of the gravitational attraction can be simplified if instead of the vector quantity acceleration $\vec{F}$ the scalar quantity of the potential V is used. Especially when look-

ing at the attraction of point systems and solid bodies as it is done in geodesy, calculations can be simplified greatly.

In vector calculus, *rot* describes the infinitesimal rotation of a vector field. A vector field whose rotation is equal to zero, is called irrotational or, especially fields of force, conservative. Following (Torge, 1989)

$$rot\ \vec{F} = 0\,. \tag{2.3}$$

meaning the vector field created by $\vec{F}$ is conservative. Following the basic computational rules for vector calculus

$$rot\ \vec{F} = rot(gradV) = 0\,. \tag{2.4}$$

meaning the rotation of a vector field vanishes if and only if there is a gradient, as it is the case for the gravity field. Therefore a corresponding potential V for the gravitational force $\vec{F}$ exists so that

$$\vec{F} = grad\ V\,, \tag{2.5}$$

where

$$V = \frac{Gm}{r}\,. \tag{2.6}$$

If additional point masses are present, it is possible to sum up the individual forces. If the number of point masses is growing beyond all limits the sum can be replaced by the integral, leading for a body v to

$$V = G \iiint_v \frac{\mathrm{d}m}{r} = G \iiint_v \frac{\rho}{r} \mathrm{d}v\,, \tag{2.7}$$

where dm is a mass element, dv a volume element, r the distance between the mass element and the attracted point P and ρ describes the density

$$\rho = \frac{\mathrm{d}m}{\mathrm{d}v}\,. \tag{2.8}$$

The potential V with the unit $\mathrm{m}^2\ \mathrm{s}^{-2}$ is continuous and finite and vanishes following $1/r$ for $r \to \infty$ which allows to approximate a body at large distances as a point mass. Also the first derivatives are continuous and finite in interior and exterior space. But at points where the density changes discontinuously, i.e. at the boundary surface or at density jumps in the interior, the second derivatives show discontinuities. This becomes evident when looking at

Poisson's equation, which has to be satisfied by the potential V

$$\Delta V = -4\pi G\rho\,, \tag{2.9}$$

with

$$\Delta V = \frac{\delta^2 V}{\delta x^2} + \frac{\delta^2 V}{\delta y^2} + \frac{\delta^2 V}{\delta z^2}\,, \tag{2.10}$$

where Δ is the so called Laplace operator. In exterior space, where $\rho = 0$, this equation becomes the Laplace equation:

$$\Delta V = 0\,. \tag{2.11}$$

2.1.2 Gravity field of the Earth

In a rotating system, such as the Earth, the total force acting on a resting mass on the Earth's surface is the sum of the gravitational force and the centrifugal force due to the rotation. This quantity is called gravity vector:

$$\vec{g} = \vec{F} + \vec{F}_z\,. \tag{2.12}$$

In a rectangular coordinate system with its origin in the Earth center, its z-axis coinciding with the rotation axis and assuming that the x-axis points to the Greenwich meridian, the components of the centrifugal force acting on P are given by the vector of Earth rotation $\vec{\omega}$ and the distance $p = \sqrt{x^2 + y^2}$ to the rotation axis (see Fig. 2.1).
The vector $\vec{F}_z$ is given by

$$\vec{F}_z = \omega^2 \vec{p} = \begin{pmatrix} \omega^2 x \\ \omega^2 y \\ 0 \end{pmatrix} = grad\ \Phi = \begin{pmatrix} \frac{\delta\Phi}{\delta x} \\ \frac{\delta\Phi}{\delta y} \\ \frac{\delta\Phi}{\delta x} \end{pmatrix}\,. \tag{2.13}$$

The corresponding centrifugal potential function Φ is

$$\Phi = \frac{1}{2}\omega^2(x^2 + y^2)\,. \tag{2.14}$$

As mentioned above the gravity vector $\vec{g}$ is the sum of the gravitational force $\vec{F}$ and the

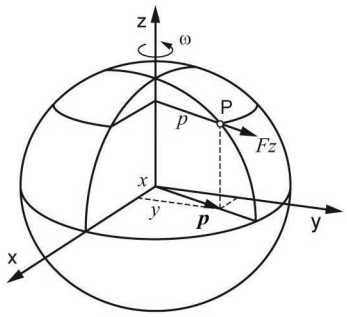

Figure 2.1: Centrifugal Force

centrifugal force $\vec{F}_z$. Accordingly, the potential of gravity W is the sum of the gravitational potential V and the centrifugal potential Φ:

$$W = W(x,y,z) = V + \Phi = G \iiint_v \frac{\rho}{r} \mathrm{d}v + \frac{1}{2}\omega^2(x^2+y^2)\,. \tag{2.15}$$

Combining the Laplace equation of Φ with Poisson's equation for V Eq.(2.9), leads to the generalized Poisson equation for the gravity potential W:

$$\Delta W = -4\pi G\rho + 2\omega^2\,. \tag{2.16}$$

The gradient of W is the gravity vector and describes the total force acting on a unit mass.

$$\vec{g} = grad\ W = \left[\frac{\delta W}{\delta x}\ \frac{\delta W}{\delta y}\ \frac{\delta W}{\delta z}\right]. \tag{2.17}$$

The vector magnitude is called gravity and has the unit of an acceleration, and the direction of the vector is the direction of the plumb line, see Fig. 2.2.

Additionally to the centrifugal force $\vec{F}_z$ another fictitious force is acting on a moving body, the Coriolis force. It is proportional to the velocity of a moving mass within a rotating reference system.

$$\vec{F}_c = -2m\vec{\omega}\times\vec{v} = 2m\vec{\omega}\begin{bmatrix}\vec{v}_n\sin\phi - \vec{v}_u\cos\phi\\ -\vec{v}_e\sin\phi\\ \vec{v}_e\cos\phi\end{bmatrix}, \tag{2.18}$$

with m denoting the mass of the moving object, $\vec{\omega}$ the rotation vector and $\vec{v}$ the velocity vector

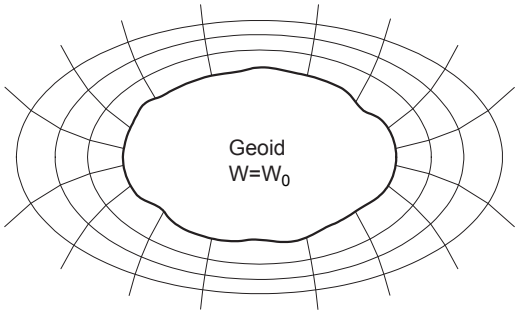

Figure 2.2: Equipotential surfaces and plumb lines

of the object in respect to the rotating system. In the right part of Eq. 2.18 the indexes n, e, u indicate the direction of the velocity vector $\vec{v}$, i.e. north, east, up. In case of the Earth it can be observed at clouds. As air moves from high to low pressure in the northern hemisphere, it is deflected to the right by the Coriolis force, in the southern hemisphere to the left. It also is the force that causes the rotation of the Foucault pendulum (Hofmann-Wellenhof and Moritz, 2005).

The geometry of the gravity field

The gravity field can be described by surfaces of constant gravitational potential (see Fig. 2.2), i.e. equipotential surfaces or level surfaces, where

$$W(x,y,z) = const. \tag{2.19}$$

The surface of the oceans in a first approximation is part of such an equipotential surface. This particular surface was proposed by Carl Friedrich Gauss as the ”mathematical figure of the Earth” and was later named geoid by the mathematician Johann Benedict Listing (Torge, 1989). Lines that intersect all equipotential surfaces orthogonally are called lines of force or plumb lines. The tangent to such a plumb line at any point equals the gravity vector at that point.

The differentiation of Eq. (2.17) leads to the gravity gradient tensor, also called Eötvös

tensor:

$$grad\ \vec{g} = \Delta W = \begin{bmatrix} W_{xx} W_{xy} W_{xz} \\ W_{yx} W_{yy} W_{yz} \\ W_{zx} W_{zy} W_{zz} \end{bmatrix} . \tag{2.20}$$

The unit of the components is 1 Eötvös corresponding to 10^{-9} s^{-2} in SI-units. Due to the irrotational nature of the gravity field,

$$rot\ \vec{g} = rot\ grad\ W = 0\,, \tag{2.21}$$

and considering Poisson's differential in Eq. (2.9) and the centrifugal potential Φ in Eq. (2.14),

$$\Delta W = W_{xx} + W_{yy} + W_{zz} = -4\pi G\rho + 2\omega^2\,, \tag{2.22}$$

the gravity gradient tensor Eq. (2.20) contains only five independent elements. Also the tensor is symmetric: $W_{xy} = W_{yx}$,$W_{xz} = W_{zx}$ and $W_{yz} = W_{zy}$. The third line of the tensor represents the gravity gradient

$$grad\ \vec{g} = \begin{bmatrix} W_{zx} W_{zy} W_{zz} \end{bmatrix} , \tag{2.23}$$

which describes the changes of gravity with respect to the coordinate axes. W_{zx} and W_{zy} are the two components of the horizontal gradient lying in a local horizontal plane and W_{zz} describes the vertical gradient, respectively. The vertical component is fundamental for the interpretation of gravity data. With Eq. (2.22) we get

$$W_{zz} = \frac{\delta^2 W}{\delta z^2} = \frac{\delta g}{\delta z} = -(W_{xx} + W_{yy}) - 4\pi G\rho + 2\omega^2\,. \tag{2.24}$$

$(W_{yy} - W_{xx})$ and 2 W_{xy} characterize the curvature of potential surfaces, i.e. how the shape of potential surfaces differs from the shape of a sphere, W_{xy} and W_{zy} characterize how potential surfaces are not parallel to each other (Völgyesi, 2001). The elements of the Eötvös tensor can be measured directly in space (see Chap. 2.2.3) or derived from gravity measurements. The torsion balance, also called torsion pendulum used for geodetic application is usually credited to Loránd Eötvös (1848-1919) and can measure the components of the horizontal gradient W_{zx}, W_{zy} as well as the curvature $(W_{yy} - W_{xx})$ and W_{xy}, but not the vertical gradient

W_{zz}.

2.1.3 Spherical harmonics

Given that outside the attracting masses the gravitational potential V is a harmonic function, it is easier to handle if it is expanded into a series of spherical harmonics. Spherical harmonics are a special solution of the Laplace's equation; for the full derivation see (Hofmann-Wellenhof and Moritz, 2005).

In the exterior space V can be represented as

$$V(r,\theta,\lambda) = \frac{GM}{r}\sum_{n=0}^{\infty}\sum_{m=0}^{n}\left(\frac{a}{r}\right)^n P_{nm}(\cos\theta)(C_{nm}\cos m\lambda + S_{nm}\sin m\lambda)\,, \tag{2.25}$$

where G is the gravitational constant and M the total mass of the Earth (solid, liquid and gaseous portions) and a is the mean radius of the Earth. The associated Legendre functions P_{nm} of degree n and order m are given for the argument $t = \cos\theta$ by:

$$P_{nm}(t) = (1-t^2)^{\frac{m}{2}}\frac{\mathrm{d}^m}{\mathrm{d}t^n}P_n(t)\,, \tag{2.26}$$

with the Legendre polynomials P_n

$$P_n(t) = P_{n0}(t) = \frac{1}{2^n n!}\frac{\mathrm{d}^n}{\mathrm{d}t^n}(t^2-1)^n\,. \tag{2.27}$$

For the gravity field determination, fully normalized spherical harmonics $\overline{P}_{nm}$ are usually used, meaning the average square of any fully normalized harmonic is unity:

$$\overline{P}_{nm}(t) = \sqrt{\frac{k(2n+1)(n-m)!}{(n+m)!}}P_{nm}(t)\,. \tag{2.28}$$

Legendre functions multiplied by $\cos m\lambda$ or $\sin m\lambda$ are called surface spherical harmonics and are used as in Eq. (2.25) to describe the spatial characteristics of V on a spherical surface. The associated Legendre functions change their sign $(n-m)$ times within the interval $0 \leq \theta \leq \pi$ and the functions $\cos m\lambda$ and $\sin m\lambda$ do change their sign $2m$ times in the interval $0 \leq \lambda \leq 2\pi$, dividing the surface at geodetic parallels and meridians into cells which are

alternatingly positive and negative. For $m \neq 0$ they divide the sphere into a chequered pattern and are called tesseral harmonics (Fig. 2.3b). For special cases $m = 0$ the spherical harmonics do not depend on the longitude and divide the sphere into zones parallel to the equator and are called zonal (Fig. 2.3a). If $n = m$, the spherical harmonics degenerate into functions that divide the sphere into sectors following the meridians and are thus named sectoral (Fig. 2.3c).

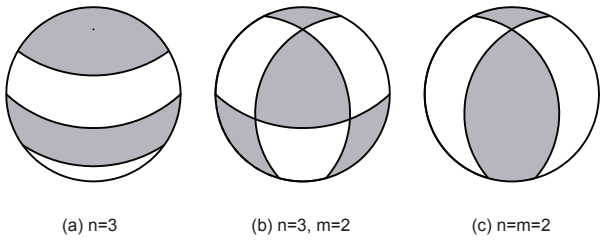

Figure 2.3: Spherical harmonics: (a) zonal, (b) tesseral, (c) sectoral

Comparing Eq. (2.25) with Eq. (2.7) it becomes clear that the spherical harmonic coefficients C_{nm} and S_{nm} in Eq. 2.25 are mass integrals of the Earth gravity field with

$$\begin{Bmatrix} C_{nm} \\ S_{nm} \end{Bmatrix} = \frac{1}{(2n+1)Ma^n} \iiint\limits_{Earth} r^n \overline{P}_{nm}(\cos\theta) \begin{Bmatrix} \cos m\lambda \\ \sin m\lambda \end{Bmatrix} \mathrm{d}M\,. \tag{2.29}$$

The first degree coefficients are related to the rectangular coordinates of the center of gravity, i.e. the geocenter. Following Hofmann-Wellenhof and Moritz (2005) and Torge (1989) we get:

$$C_{10} = \frac{1}{a^2 M} \iiint\limits_{Earth} z' \mathrm{d}M\,, \qquad C_{11} = \frac{1}{a^2 M} \iiint\limits_{Earth} x' \mathrm{d}M\,,$$

$$S_{10} = \frac{1}{a^2 M} \iiint\limits_{Earth} y' \mathrm{d}M\,. \tag{2.30}$$

If the origin of the coordinate system coincides with the center of gravity, meaning x', y', z' are equal to zero, then these coordinates and thus the degree 1 coefficients are zero. The second degree Stokes' coefficients (Eq.2.31) are related to the moments and products of Inertia I_{ij} with respect to the axes of the reference system and thus predominantly driven by variations in the moment of inertia tensor.

$$C_{20} = -\frac{1}{a^2 M}[I_{33} - \frac{1}{2}(I_{11} + I_{22})]\,,$$
$$C_{21} = \frac{I_{13}}{a^2 M}\,, \qquad S_{21} = \frac{I_{23}}{a^2 M}\,. \tag{2.31}$$

C_{20} can be related directly to the figure of the Earth as it describes the flattening of it and corresponds to the dynamic form factor $J_2 \widehat{=} -C_{20}$. C_{21} and S_{21} describe the deviation of the instantaneous axis of rotation with respect to the polar principal axis of inertia. If these axes coincide, the coefficients in Eq. 2.31 will be zero. C_{22} and S_{22} describe the asymmetry of the equatorial mass in relation to the rotation axis and the torsion of the corresponding principal axes of inertia (Hofmann-Wellenhof and Moritz, 2005; Torge, 1989).

2.2 Determination of the Earth gravity field

In this chapter the methods and instruments used for gravity field determination will be described as well as the theory behind. The first part is dedicated to the theories of Bruns and to Stokes' formula, which make the determination of the geoid through gravity measurements possible. The second part gives an insight into the practical gravity field determination using ground- and satellite-based instruments. Whereas ground-based instruments deliver gravity values at very high accuracies for discrete points, satellite measurements have the advantage of global coverage. Both strategies are indispensable for a geoid determination of highest accuracy.

2.2.1 The theories of Bruns and Stokes' formula

The theory of Bruns is defined as the comparison of the equipotential surface $W = W_0$ with the equipotential ellipsoid (or sphere) with the same potential $U = W_0$. U describes an approximation of W and can be set equal to

$$W = U + T\,, \tag{2.32}$$

with T being the perturbation potential, depending in general on the irregularities of the density of the Earth. The point P on W_0 and Q on $U = W_0$ are separated by the distance N,

the so called geoid undulation, positive if the geoid is above the ellipsoid, otherwise negative. Due to the fact that U and W are equipotential surfaces of two different mass assemblies, they seldom coincide.

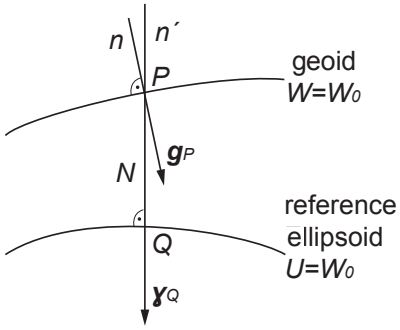

Figure 2.4: Geoid and reference ellipsoid.

The gravity vector $\vec{g}_P = -grad\ W_0$ is defined on the geoid, the theoretical $\vec{\gamma}_P = -grad\ U$ on the ellipsoid. The difference of the two vectors is called gravity anomaly vector

$$\Delta\vec{g} = \vec{g}_P - \vec{\gamma}_Q\,, \tag{2.33}$$

the difference in magnitude gravity anomaly

$$\Delta g = g_P - \gamma_Q\,. \tag{2.34}$$

The difference in direction of the plumb lines is called gravimetric deflection of the vertical, which has a north and south component. If both vectors are compared in P we get the gravity disturbance vector

$$\delta g = \vec{g}_P - \vec{\gamma}_P\,. \tag{2.35}$$

Since

$$W_P = U_P + T_P = U_Q - \gamma\, N + T_P\,, \tag{2.36}$$

and

$$W_P = U_Q = W_0\,, \tag{2.37}$$

we find

$$N = \frac{T}{\gamma}\,. \tag{2.38}$$

This is the famous Bruns formula, linking the geoid undulation to the disturbing potential. Taking into account the definition of the gravity anomaly (Eq. 2.34), the fundamental equation of physical geodesy, relating the measurable quantity Δg to the unknown anomalous potential T can be found

$$\frac{\delta T}{\delta h} - \frac{1}{\gamma}\frac{\delta \gamma}{\delta h} T + \Delta g = 0\,. \tag{2.39}$$

Since Δg is only known on a surface, i.e. the geoid, and not throughout space, the fundamental equation 2.39 can only be used as a boundary condition. However, reducing all the measured gravity values to the geoid and assuming that all masses are enclosed by the geoid, the effect of the masses outside can be removed. For that case the anomalous potential T is harmonic and satisfies Laplace's equation (Eq. 2.11). If the boundary condition is written in the form

$$-\frac{\delta T}{\delta h} + \frac{1}{\gamma}\frac{\delta \gamma}{\delta h} T = \Delta g\,, \tag{2.40}$$

where we assume that Δg is known at every point of the geoid, the linear combination of $\frac{\delta T}{\delta h}$ and T is given on the surface. This defines the determination of T as a third boundary-value problem of potential theory. If it can be solved for T, the geoidal height, the most important geometric quantity in physical geodesy, can be computed by Bruns formula (Hofmann-Wellenhof and Moritz, 2005).

By introducing a mean radius of the Earth a and a mean value of gravity γ_0 Eq. 2.40 can be rewritten as

$$\Delta g = -\frac{\delta T}{\delta h} - \frac{2}{a} T\,. \tag{2.41}$$

Outside the Earth it becomes

$$\Delta g = -\frac{\delta T}{\delta h} - \frac{2}{r} T\,, \tag{2.42}$$

expanded into a series of spherical harmonics we get

$$\Delta g = -\frac{1}{r}\sum_{n=0}^{\infty}(n-1)\frac{a^{n+1}}{r} T_n(\phi,\lambda)\,. \tag{2.43}$$

This formula allows to compute gravity anomalies Δg from satellite based spherical harmonic series of the external gravitational potential. By upward continuation and integration of Eq.

2.42 we obtain Pizzetti's formula

$$T(r,\phi,\lambda) = \frac{a}{4\pi}\iint_{\sigma} \Delta g\, S(r,\psi)\mathrm{d}\sigma\,, \tag{2.44}$$

where $S(r,\psi)$ is called Stokes' function,

$$S(r,\psi) = \frac{2a}{l} + \frac{a}{r} - 3\frac{al}{r^2} - \frac{a^2}{r^2}\cos\psi(5 + 3\ln\frac{r - a\cos\psi + l}{2r})\,. \tag{2.45}$$

On the geoid where $r = a$ it becomes

$$T(r,\phi,\lambda) = \frac{a}{2\pi}\iint_{\sigma} \Delta g\, S(r,\psi)\mathrm{d}\sigma\,, \tag{2.46}$$

with

$$S(r,\psi) = \frac{1}{\sin(\psi/2)} - 6\sin\frac{\psi}{2} + 1 - 5\cos\psi - 3\cos\psi\ln(\sin\frac{\psi}{2} + \sin^2\frac{\psi}{2})\,. \tag{2.47}$$

Applying Bruns' theorem, we get

$$N = \frac{a}{4\pi\gamma_0}\iint_{\sigma} \Delta g\, S(\psi)\mathrm{d}\sigma\,. \tag{2.48}$$

This formula is called the Stokes' formula or Stokes' integral, named after G.G. Stokes, who published it in 1849. It is considered to be the most important formula of physical geodesy because it allows to determine the geoid from gravity data. It shall be mentioned that in this original form the Stokes' integral only applies for a reference ellipsoid that has the same potential $U_0 = W_0$ as the geoid, encloses the same mass as the Earth and has its center at the center of mass of the Earth. The latter applies because T contains no spherical harmonic of degree one, otherwise the term $\Delta g_n/(n-1)$ would be infinite for $n = 1$.

2.2.2 Terrestrial gravity determination

Absolute gravimeter

The determination of the absolute gravity value with absolute gravimeters makes use of the so called free fall method, based on the second law of Newton, stating that the acceleration

of a mass m is proportional to the acting force $\vec{F}$. Is the falling mass within the Earth gravity field, the acceleration of the free fall equals $\vec{g}$:

$$\vec{F} = \vec{g}m\,. \tag{2.49}$$

Under the assumption of a constant $\vec{g}$ along the distance of fall, the equation of motion can be determined by integrating twice:

$$\ddot{z} = g\,,$$

$$\dot{z} = gt + c_0\,, \qquad \text{with } c_0 = v_0\,,$$

$$z = \frac{1}{2}gt^2 + c_0 t + c_1\,, \qquad \text{with } c_1 = z_0\,,$$

leading to:

$$z = \frac{1}{2}g\,t^2 + v_0\,t + z_0\,. \tag{2.50}$$

The integration constants are the initial values z_0 and v_0 which describe the position and velocity of the falling mass at the time-epoch $t = 0$. Equation 2.50 describes the free fall as a function of time through a parabola.

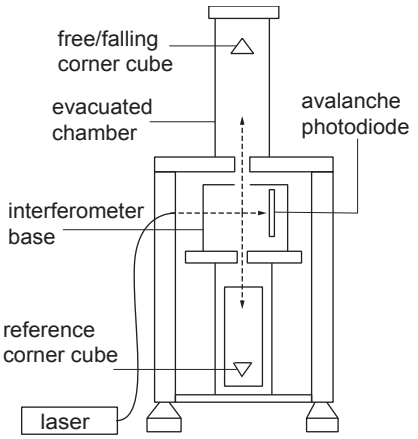

Figure 2.5: Schematics of the FG5 absolute gravimeter

The movement, thus the position of the falling mass, i.e. the corner cube, is observed at several points through simultaneous path and time measurements z and t. With an adjustment procedure it is then possible to determine the unknowns z_0 and v_0 as well as the gravity acceleration g. The needed accuracy of the path and time measurement can be estimated

with

$$\frac{\mathrm{d}g}{g} = \frac{\mathrm{d}z}{z} - 2\frac{\mathrm{d}t}{t}. \tag{2.51}$$

With a desired accuracy of dg of 10 nm s^{-2} for $g \cong 10$ m s^{-2}, the distance of fall $z = 0.2$ m and the fall time of t=0.2 s, the necessary accuracies of the path and time measurements are dz = 0.2 nm and dt = 0.1 ns. These high requirements are ensured through laser interferometry and atomic clocks. The FG5, one of the most widely used portable absolute gravimeters manufactured by Micro-g LaCoste, achieves a precision of 21 nm s^{-2}, equivalent to a 6 mm change in elevation. Figure 2.5 shows the basic schematics of it.

For completeness also the nowadays outdated pendulum method should be mentioned, which is based on the observation of the oscillation time of a pendulum of known length within the gravity field (Torge, 1989). With this methods accuracies up to $\pm 5\ \mu$ m s^{-2} could be reached. Absolute gravimeters are a necessity to calibrate relative gravimeters introduced later in this chapter.

Atom interferometer for g measurements

Atom interferometry is based on the deBroglie hypothesis (deBroglie, 1924), which states that the coexistence of waves and particles, discovered by Einstein in 1905 in case of light and photons, is valid for all matter. His work was supported by Einstein, confirmed by the electron diffraction experiments of Davisson and Germer (1927), and generalized by the work of Schrödinger (1926). But it hasn't been possible until 1991 that interference with whole atoms could be observed (Carnal and Mlynek, 1991). From then atom interferometry developed into a powerful ultra precise tool for acceleration and rotation measurements, e.g. local gravity (Peters et al, 2001) and its gradient (Snadden et al, 1998). In theory atom interferometers have the potential to exceed the performance of the existing gravity meters (Le Gouet et al, 2008), however up until now these experiments are mainly confined to laboratories. But in the recent years great efforts are undertaken to develop mobile atom interferometers which also might be used on satellite missions (Yu et al, 2006; Tino et al, 2007). Fig. 2.6 depicts the basic principle of an atom interferometer.

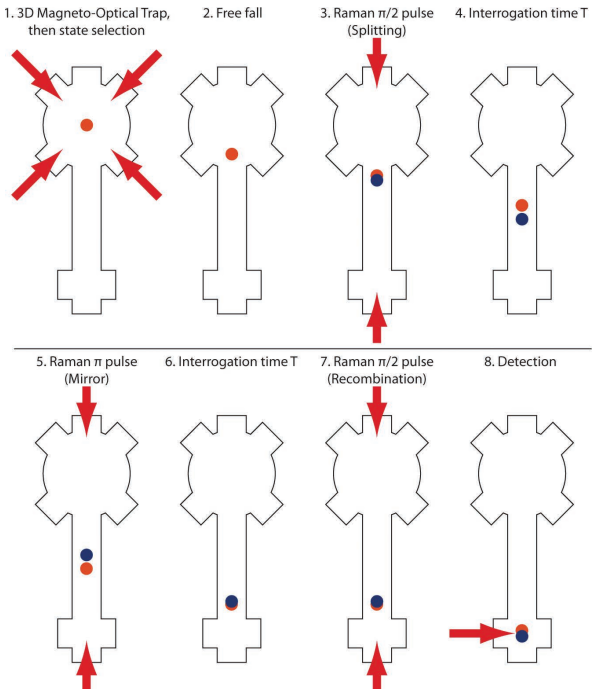

Figure 2.6: Scheme of an atomic gravimeter, from Schmidt (2011).

While classical gravimeters use a macroscopic test mass (see Chap. 2.2.2) atom interferometers use an ensemble (mostly 10^8) of laser-cooled atoms whose change in position is monitored by their interaction with a stationary Raman laser wave (Peters et al, 2001). During the fall, the atoms are subjected to three laser pulses, parallel to the direction of the free fall (see. Fig. 2.6). The first pulse causes half of the atoms to be transferred to the other hyperfine ground state F, thus during an interrogation time T both clouds will separate in space. The second pulse exchanges internal and momentum states of the two clouds, acting as a mirror. The third pulse recombines the atoms again. At the output the population ratio between atoms in both hyperfine states are measured, which are related to the gravity acceleration $\vec{g}$:

$$P_{|F=2\rangle} = \frac{1}{2}[1 - cos(\vec{k_{eff}}\vec{g}T^2)]\,, \tag{2.52}$$

where $\vec{k_{eff}}$ denotes the Raman laser vector.

Starting with two atomic clouds this concept can be extended to measure the local gravity gradient (Snadden et al, 1998). The difference in the resulting signal of both clouds is

proportional to the difference in gravity acceleration between the two clouds:

$$\Delta\Phi_2 - \Delta\Phi_1 = \vec{k_{eff}}(\vec{g}_2 - \vec{g}_1)T^2\,, \tag{2.53}$$

with $\Delta\Phi$ being the phase difference between the two packages of each cloud after the third pulse. Existing ground based atom interferometers reach an accuracy of Δg=4 μGal and a resolution of Δg=8 μGal/$\sqrt{\text{Hz}}$ (Mueller et al, 2008), gradiometer 4 E/$\sqrt{\text{Hz}}$ (McGuirk et al, 2008). Alternative concepts using ultra cold atoms are also under development, but these still have to reach the accuracy of the Raman-pulse atom interferometer.

Relative Gravimeter

When measuring relative gravity, the sensor is only able to observe directly or indirectly one of the two fundamental acceleration quantities time or length. To solve this under-determined problem, one of the two quantities is fixed. The gravity difference is then calculated from the observed difference in time or length (Torge, 1989). Relative gravimeters are based on the principle of Newton's Spring Scale where the change in length of a coil is related to the change in gravity

$$\mathrm{d}g/g = k(\mathrm{d}l/l)m\,, \tag{2.54}$$

with k being the coil constant and m the mass of the test mass attached to the coil. The simplest form of a vertically hanging spring is too imprecise to achieve satisfactory measurement accuracy. To resolve for gravity in nm s^{-2} range, gravimeters based on the lever spring balance were developed. The principle of such a relative gravimeter is depicted in Fig. 2.7.

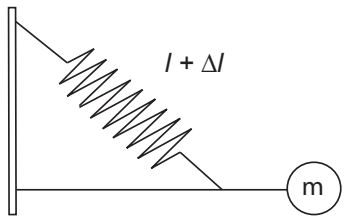

Figure 2.7: General lever spring balance principle

To further increase the resolution of the gravimeter by so called astatisation, Lucien LaCoste

developed in 1942 the so called zero-length coil; it behaves as though its unweighted length is zero. Nowadays the relative gravimeter are compact and easily transportable and reach 1 nm s^{-2} resolution.

Superconducting gravimeters (SG) take the idea of the coil-mass system a step further. They consist in general of a supra conducting coil generating a magnetic field, which holds a super conducting hollow sphere in abeyance (see Fig. 2.8). Forces acting as accelerations on this sample mass are compensated by a control loop such that the sphere does not change its position in space. The power needed to do so, can be directly related to the change in gravity (Torge, 1989).

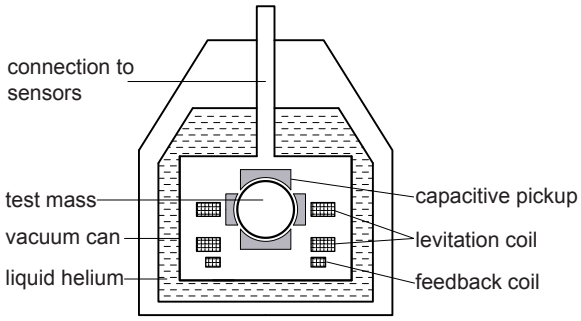

Figure 2.8: SG principle (modified fromTorge, 1989)

The applications of observing the time varying gravity field with SGs are:

- monitoring of the solid Earth tides with high accuracy to determine the exact elastic parametrization of the Earth,
- registration of gravity changes as part of height changes,
- registration of gravity changes in consequence of polar motion,
- detection of seismically induced self-oscillation of the Earth ,
- detection of the eigenmode of the Earth core,
- investigation of deformations of the crust due to atmospheric and oceanic loading, and/or

- investigation of meteorological phenomena.

SGs excel on the high resolution of the signal (< 0.1 nm/s^2) and the low instrument drift between 0 and 100 nm/s^2 per year depending on the instrument. This can be related to the low noise level, achieved through operating near absolute zero and the almost complete shielding of the instrument against changes in temperature, pressure and magnetic fields. The whole gravimeter resides in a tank filled with liquid Helium with a constant temperature of 4.2 K. The sensor itself is in a vacuum cylinder where the position of the sample mass, a Niob sphere of one inch in diameter, is controlled by a capacitive bridge where a feed-back coil is holding it in place. The coil current is proportional to the reset force and serves as signal (Torge, 1989). The sole manufacturer of superconducting gravimeter is GWR Instruments, founded by J. Goodkind, R. Warburton and R. Reineman.

In 1997 an international network of superconducting gravimeters (Fig. 2.9) was established within the Global Geodynamics Project (GGP) (Crossley and Hinderer, 2009) and further extended in 2003. During the IUGG assembly in 2007 it was decided to move to a permanent network hosted by IAG (International Association of Geodesy) and become part of GGOS (Global Geodetic Observing System). GGP has two main goals, first to record the Earth's gravity field with high accuracy at a number of stations worldwide using superconducting gravimeters, where each site is visited at least twice per year with an absolute gravimeter to co-determine secular changes and check calibration. The second objective is to maintain standards for the deployment of all GWR SGs, including site, instrument, data acquisition, and processing guidelines for SG instruments.

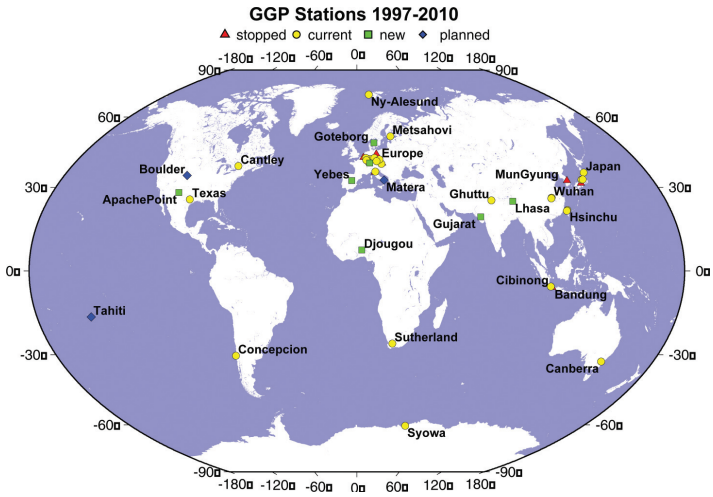

Figure 2.9: Network of the GPP, status of 2010, source: GGP project homepage `http://www.eas.slu.edu/GGP/ggphome.html`

2.2.3 Satellite based gravity determination

Prior to the satellite era, when the measurements were purely terrestrial and airborne, the Earth gravity field was known with a high accuracy only for a few regions of the world. In large parts of the globe were virtually no gravity data. The aim of satellite based gravity field exploration was to close these gaps.

Satellite laser ranging SLR

The Earths oblateness, i.e. the C20 coefficient, induces the largest perturbations on a satellites trajectory (Reigber, 1989) and is therefore a critical component in mission design. In the mid 1970s the international community initiated the launch of the first satellites for geodetic purposes. These spacecrafts orbit the Earth as completely passive, free falling objects covered by laser corner cubes. A global network of stations measure the instantaneous round trip time of ultrashort pulses of light to the satellites, hence the name of the technique: Satellite Laser Ranging (SLR), see Fig. 2.10. This provides instantaneous range measurements of millimeter level precision which can be accumulated to provide accurate orbits. From them the geocentric position of an Earth satellite can be determined and thus also the geocenter (Cheng et al, 1997). If the time series of the measurements are long enough this technique also allows to determine the long wavelenght temporal variations in the Earths gravity field;

especially for the low degree coefficients SLR is indispensable and it is the most precise technique currently available to determine C_{20} (see Fig. 2.11).

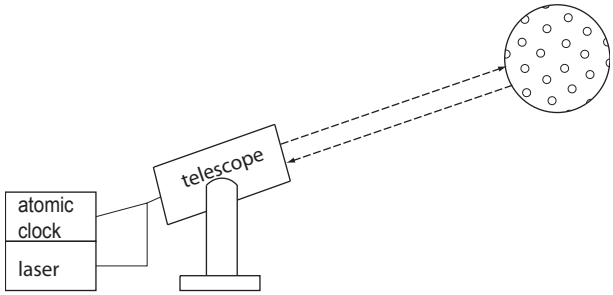

Figure 2.10: Scheme of SLR: transmit/receive telescope, puls laser, atomic clock, geodetic satellite equipped with corner cube reflectors.

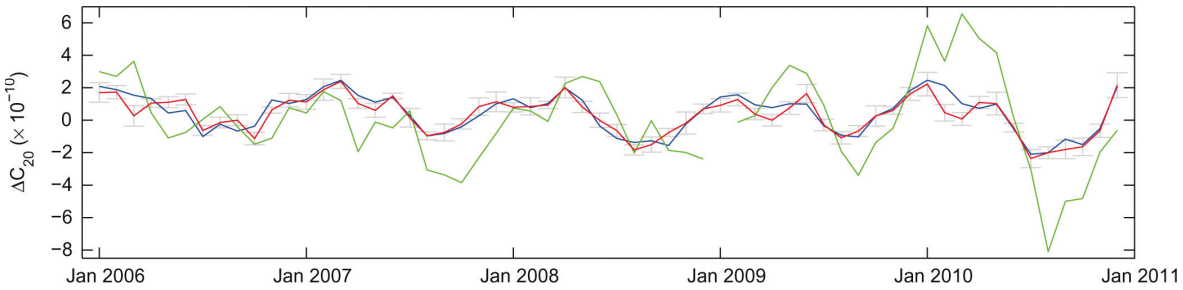

Figure 2.11: Temporal variation of the C_{20} coefficient, in red and blue a SLR-solution, in green GRACE (Maier et al, 2012).

Over the years a global network of ground stations was established and today the International Laser Ranging Service (ILRS, Pearlman et al (2002)) collects, merges, archives and distributes SLR and Lunar Laser Ranging (LLR) observation data and their related products . Figure 2.12 shows the location of the stations and the ground tracks for seven days of SLR data. Here one weaknesses of this system becomes evident: the uneven distribution of the ground stations over the globe, i.e. the dense network in Europe (more than 50 % of the measurements are taken there) versus the vast uncovered areas over the oceans and sparse station numbers in the southern hemisphere. Nevertheless SLR is indispensable for measuring the low gravity field coefficients as well as for the maintenance of an accurate International Terrestrial Reference Frame (ITRF).

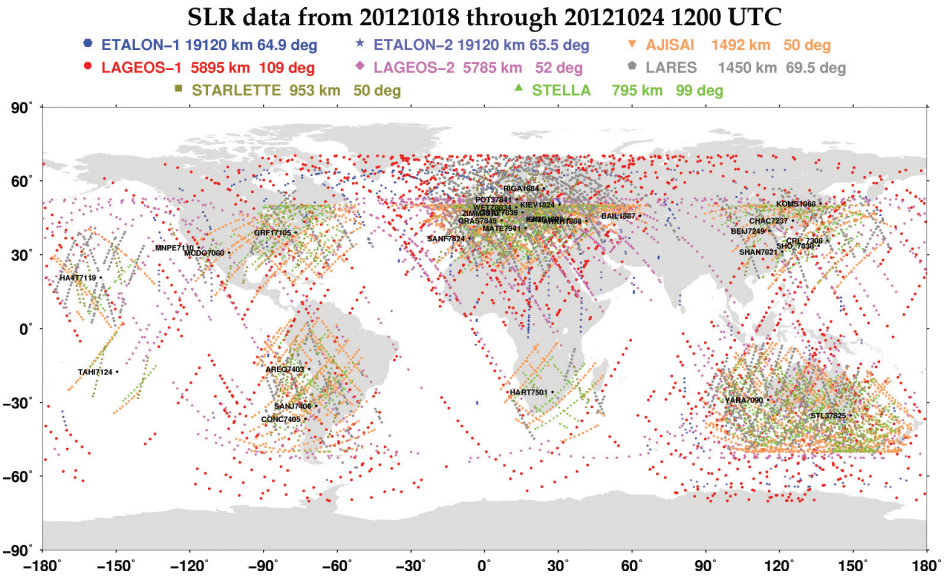

Figure 2.12: Network of SLR stations and ground tracks of seven days of geodetic SLR data, source: ILRS.

CHAMP: Satellite-To-Satellite-Tracking in high-low mode

The orbit of a Low Earth Orbit (LEO) satellite is continuously monitored by GNSS satellites and an on-board three-dimensional accelerometer measures the perturbing accelerations caused by the Earth gravity field. These observables correspond to the first derivative of the gravitational potential. This principle was realized within CHAMP (CHAllenging Minisatellite Payload, (Reigber et al, 2002b)).

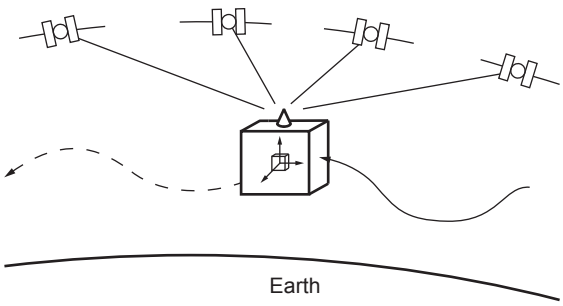

Figure 2.13: Scheme of CHAMP: one on-board 3-axis accelerometer, tracked by GNSS satellites

CHAMP was a satellite mission led by the GFZ (German Research Centre for Geosciences) for geoscientific and atmospheric research and applications, launched on 15 July 2000 and

ended 19 September 2010. It was equipped with magnetometer, accelerometer, star sensor, GPS receiver, laser retro reflector, and an ion drift meter, initially operated in a near polar orbit in 454 km above Earth surface. CHAMP was the first satellite to be able to simultaneously generate highly precise gravity and magnetic field measurements.

Exemplarily in Fig. 2.14 the EIGEN-CHAMP03S (Reigber et al, 2004) geoid is shown, it is a CHAMP-only gravity field model derived from CHAMP GPS satellite-to-satellite and accelerometer data out of the period October 2000 through June 2003. The accuracy of EIGEN-CHAMP03S is about 5 cm and 0.5 mgal in terms of geoid heights and gravity anomalies, respectively, at 400 km half-wavelength.

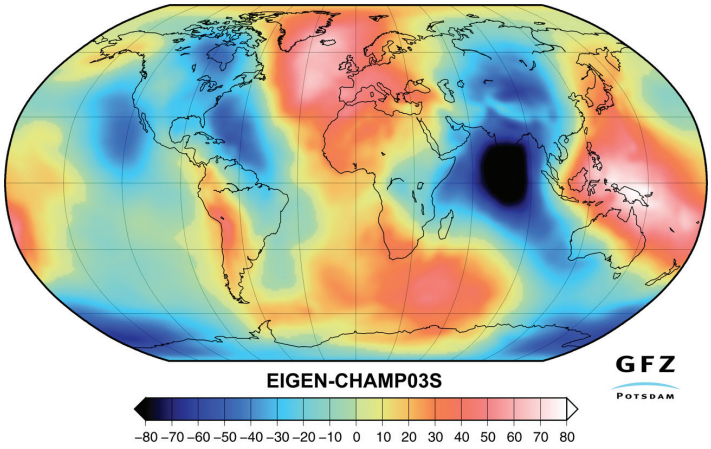

Figure 2.14: EIGEN-CHAMP03S Geoid in meter, Reigber et al (2004)

The selected EIGEN-CHAMP03S solution space of the Stokes' coefficients is complete to degree and order 120 with an increased resolution up to maximum degree 140 for sensitive and resonant orders. For more detailed information refer to Reigber et al (2002a, 2004).

GRACE: Satellite-To-Satellite-Tracking in low-low mode

The basic idea is that two LEO satellites equipped with three-dimensional accelerometers are placed in the same orbit but separated by several hundred kilometers. Both satellite orbits are monitored by GNSS and additionally the range rate between them is measured, corresponding to differences in acceleration.

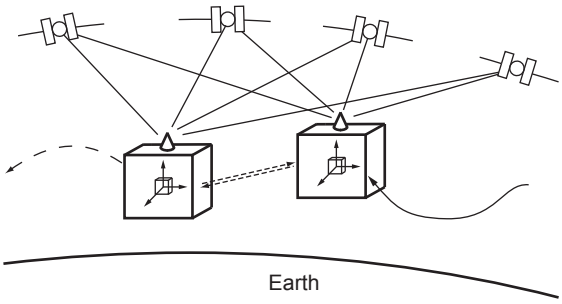

Figure 2.15: Scheme of GRACE: twin-satellites with one on-board 3-axis accelerometer and microwave ranging system, tracked by GNSS satellites

The GRACE (Gravity Recovery and Climate Experiment, (Tapley et al, 2004)) mission was launched in March 2002 under the NASA Earth System Science Pathfinder (ESSP) Program, to accurately map variations in the Earth's gravity field over its lifetime. The GRACE mission has two identical spacecrafts flying about 220 km apart in a polar orbit 500 kilometers above the Earth performing accurate measurements of the distance between the two satellites using a microwave ranging system. GPS is used for positioning. The ranging system is sensitive enough to detect separation changes as small as 10 μm over the distance of 220 km between the satellites (Wahr et al, 1998).

Gravity variations that GRACE is sensitive to include: changes due to surface and deep currents in the ocean, runoff and ground water storage on land masses, exchanges between ice sheets or glaciers and the oceans, or variations of mass within the Earth (see also Chap. 2.3). Figure 2.16 shows the mean monthly variability of continental water storage from GRACE data for the period 2002-2011 in terms of equivalent water height in mm.

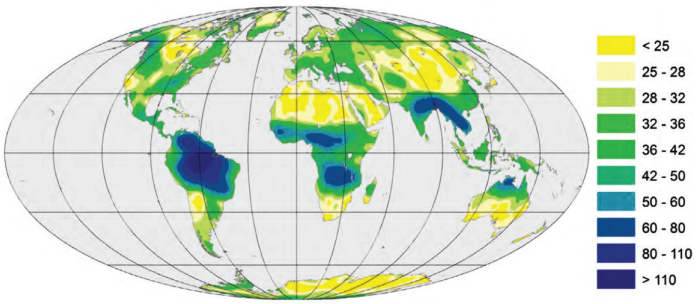

Figure 2.16: Mean monthly variability of continental water storage (2002-2011), Güntner et al (2012). , Reigber et al (2005)

GRACE provides for the first time global data that shows the variability of water storage on monthly, seasonal to inter-annual time scales (e.g. Schmidt (2006)). Areas of large variability include tropical and their marginal areas which are characterized by their seasonal change of rain and dry seasons. In the rainy season the water iis stored in the soil, as ground water but also in the flood areas along major rivers such as the Amazon or Ganges saved. Clearly visible are also areas at high latitudes, where snow accumulates in winter and melts in the spring and summer, resulting in large seasonal variations in water storage (Güntner et al, 2012).

GOCE: Satellite gravity gradiometry

Satellite gradiometry consists basically of the measurement of the acceleration differences in three spatial orthogonal directions between the six test masses situated on each end of the axes. This measurement quantity corresponds to the gradients of the gravity acceleration, i.e. the second derivative of the gravitational potential.

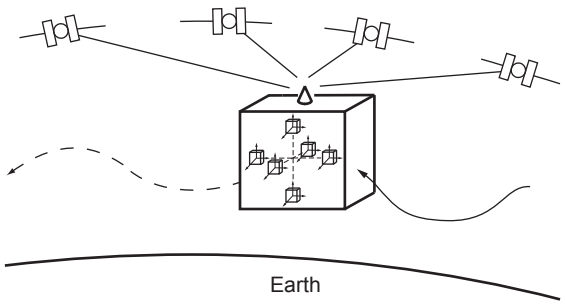

Figure 2.17: Scheme of GOCE: Six on-board 3-axis accelerometers, tracked by GNSS satellites

GOCE (Gravity field and steady-state Ocean Circulation Explorer, (Rummel et al, 2000)) was launched on 17 March 2009 and was the first mission of ESA's Living Planet Program. It is the first satellite equipped with a gradiometer and thus helps to better understand the static gravitational field of the Earth. The missions objectives are to obtain gravity gradients from which new global and regional models can be deduced at length scales down to 100 km with a geoid accuracy of 1-2 cm. This corresponds to gravity field anomaly accuracy of 1 mGal. Today GOCE effectively resolves the gravity field to degree 200, attenuated to 250

(Drinkwater et al, 2003).

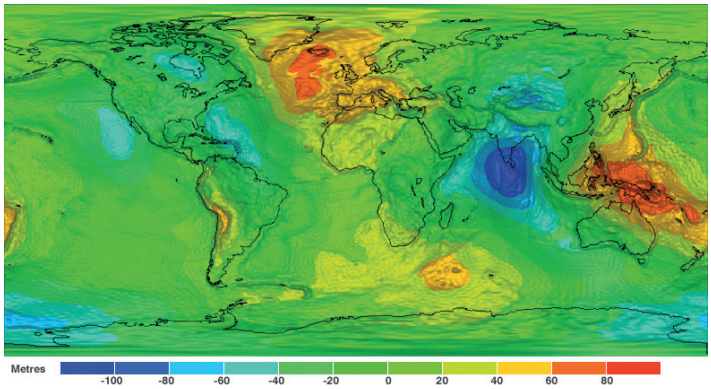

Figure 2.18: First GOCE-only gravity field in meter, Pail et al (2011)

Satellite gravity gradiometry (SGG) data alone are not sufficient to accurately determine the low-degree coefficients of the gravity field due to the noise characteristics of the gradiometer. The GPS satellite-to-satellite tracking (SST) data are used to determine the precise orbit, thus geo-locating the gravity tensor observables, and the long-wavelength part of the gravity field, same as for CHAMP and GRACE. It was decided to implement three different gravity field modeling approaches in the GOCE High level processing facility (Rummel et al, 2004): direct (DIR), time-wise (TIM) and space-wise (SPW). Approach DIR is based on the least-squares solution of the inverse problem, i.e. it starts with an a priori gravity field model and adds GOCE information to improve it. The partial derivatives for all parameters to be adjusted, i.e. the spherical harmonic coefficients, are computed and normal equations are generated by processing e.g. daily arcs. TIM considers the gravity gradient and orbit observations as time-series measured along the orbit and computes a GOCE-only model in a rigorous sense. In both cases large normal equation systems have to be built and solved, leading to a high demand on CPU power (Pail et al, 2007). In contrast, SPW works predominantly in the space domain, applying least squares collocation and exploiting spatial correlations of the gravity field (Tscherning, 2001). To diminish the dimension of the system it is implemented as a multi-step collocation procedure iterated till convergence. An overview of all the methods as well as further references are given in (Pail et al, 2011).

Future missions

The GRACE Follow-On mission, a cooperation between the German Research Centre for Geosciences (GFZ) and NASA, is focused on maintaining data continuity from GRACE and is planned for launch in 2017 (Flechtner et al, 2012). To minimize the project schedule as well as the technical and cost risk a high inheritance 'replica' of GRACE is conceptualized, taking into account the lessons learned from GRACE. Additionally to the microwave ranging system a laser interferometer will be installed for an improved ranging at the nm/sec level, which also serves as a technical demonstration of this technology for future missions with more satellites and different orbit constellations in the time frame beyond 2020 (Gruber et al, 2011).

As a possible successor of the GOCE mission several projects using atom interferometry (see Chap. 2.2.2) are under consideration. Such atom interferometers make it possible to measure the absolute acceleration value plus the complete gravity gradient tensor at very high sensitivity, i.e. 10^{-17} Gal or well below 1 mE in space. Implementing such a device would allow lower orbits and therefore a higher spatial resolution, also a broader frequency range is observable at a higher temporal resolution leading to a higher accuracy of the measurement (Yu et al, 2006; Tino et al, 2007).

2.3 Temporal variation of the Earth's gravity field

This chapter gives a short overview over various effects which introduce changes in the Earth gravity field, except the influence of the atmosphere. This will be treaded thoroughly in Chapter 3. Temporal changes in Earth gravity can generally be divided into two classes; first, changes in Earth rotation and Earth tides, and second, into variations caused by mass changes in the system Earth. In 1687, Sir Isaac Newton explained for the first time ocean tides as a result of the gravitational attraction of the sun and moon on the oceans (Newton, 1687), 1863 Lord Kelvin introduced the tidal deformation of the elastic Earth (Thomson, 1863). The parameters describing the elasticity of the Earth as a ratio of observed and theoretical tidal amplitudes, were introduced by Love (Love, 1909). 50 years later, in the International Geophysical Year 1957, it was demonstrated that the amplitude ratio shows local variations,

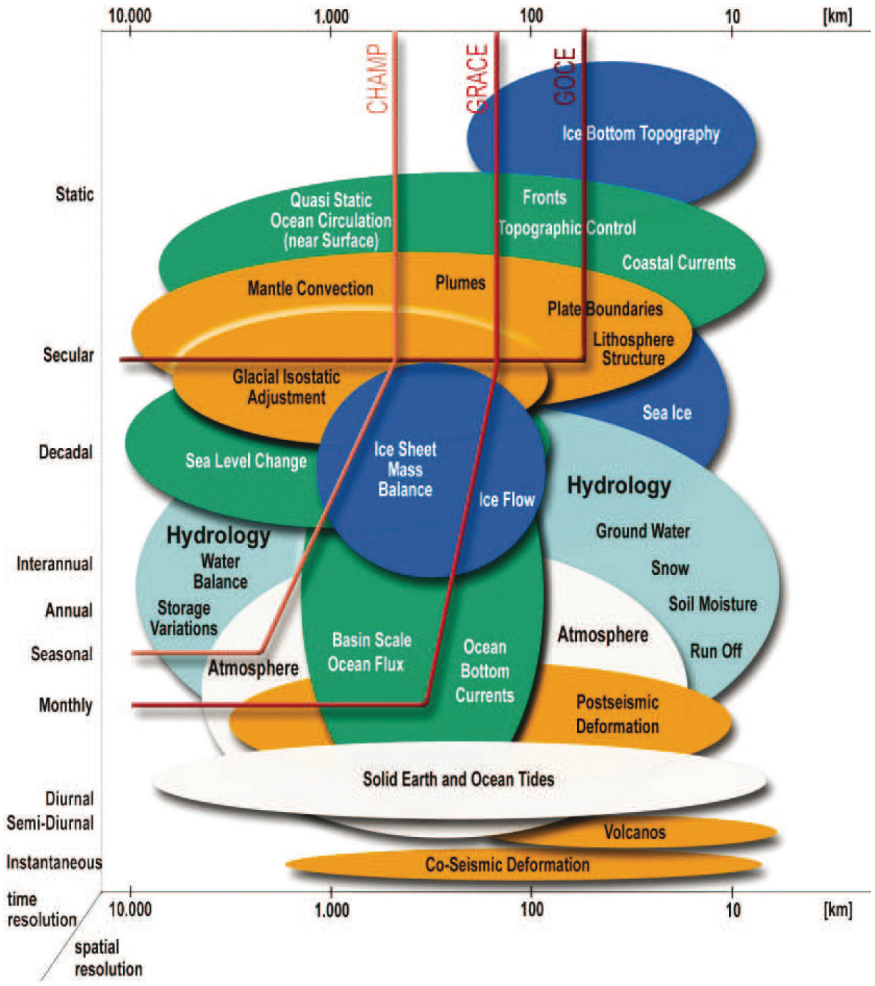

Figure 2.19: Effects of mass signals on spatial and temporal determination of the geoid, from Sneeuw et al (2005).

pointing to the inhomogeneous structure of the Earth crust (Tomaschek and Schaffernicht, 1957). But only starting from the 1960's, after static gravimeter reached the needed accuracy, non-tidal gravity changes could be observed.

Figure 2.19 shows different geophysical effects depending on temporal and spatial variability of mass signals, many of them overlapping. All these phenomena can benefit greatly from global and precise gravity observations. But to be able to separate overlapping background signals, highly accurate background data is required as well as reliable modeling of aliasing signals. While spatial-temporal localized effects such as volcano eruptions can be measured best by ground based systems, satellite measurements can give a better insight into larger and global scales.

2.3.1 The gravity constant and Earth rotation

Although the Newtonian gravitational constant $G = 6.6742 \cdot 10^{-11}$ m^3 kg^{-1} s^{-2} is one of the longest known physical quantities, it is also the one we know only little about. Most other constants of nature are determined to parts per billion, G however proves to be extremely difficult to be measured. Therefore a large variety of values and change rates can be found in the literature. Further on, in recent years a possible time dependency of G is under discussion. The Earth rotation vector $\vec{\omega}$ is not only subjected to secular changes, but also to periodic and irregular ones leading to a variation in the centrifugal acceleration and thus to a change in the centrifugal force (Eq. 2.13), changing gravity too. Using a spherical approximation the radial component of the centrifugal acceleration can be given as (Torge, 1989):

$$z_r = -\omega^2 R cos^2 \varphi \tag{2.55}$$

By differentiating this equation the dependency of gravity on changes in latitude $\delta\varphi$, i.e. polar motion, and in angular velocity $\delta\omega$, i.e. length of day, becomes evident.

$$\delta z_r = -\omega^2 R sin2\varphi \delta\varphi - 2\omega R cos^2 \varphi \delta\omega \tag{2.56}$$

2.3.2 Gravitational tides of the solid Earth

Looking at a solid Earth and its movements around the Sun (following holds also for the Moon and other celestial bodies), the attraction $\vec{a}_s = GM_s/r_s^2$ exerted by the sun and the centrifugal acceleration $a_z = \omega^2 r_o$ resulting from the rotation around the common center of gravity, are in equilibrium in the Earth's center of mass (with r_s= distance to Sun, M_s= mass of the sun, r_o= geocentric distance to the common center of gravity, see Fig. 2.20). Further, the centrifugal acceleration $\vec{a}_z$ forms a homogeneous field, meaning that in all locations on the Earth is has the same magnitude and direction. The attraction $\vec{a}_s$ exerted by the sun on the other hand is bigger on the side facing the Sun and smaller on the other side. Adding those two vectors results in the vector of the tidal forces $\vec{a}_t$.

The tidal potential V_t can be introduced by:

$$\vec{a}_t = \vec{a}_s + \vec{a}_z = grad\ V_t \tag{2.57}$$

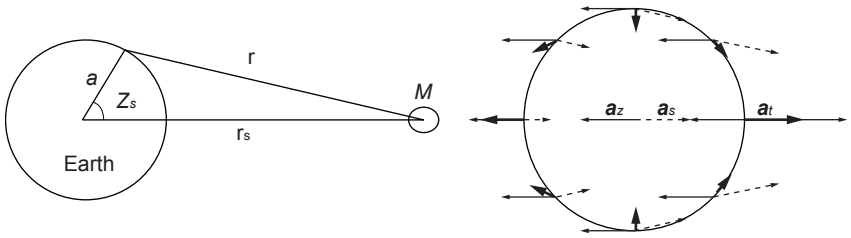

Figure 2.20: On the left the geometry for the problem for computing the tidal force on a point on Earth, caused by an external body M. On the right the corresponding field of forces.

V_t can be expanded into spherical harmonics (see Chap. 2.1.3), ignoring degrees $n < 2$ due to the system equilibrium (Torge, 1989). For $n = 2$ we get:

$$V_t = \frac{3}{4} GM_t \frac{r^2}{r_t^3} (\cos 2\, Z_s + \frac{1}{3}), \tag{2.58}$$

with r = geocentric distance of the attracted point and Z_s= geocentric zenith angle of sun.

$$\frac{\delta V_t}{\delta r} = \frac{2}{r} V_t = \frac{3}{2} GM_t \frac{r}{r_s^3} (\cos 2\, Z_s + \frac{1}{3}) \tag{2.59}$$

gives the radial component of the tidal acceleration, which is responsible for a decrease of the Earth gravity. The maximum variations occur in zenith and nadir direction of the attracting body and the corresponding perpendicular directions. For the moon they amount to 1.65 μms^{-2}, for the sun to 0.76 μms^{-2}. In general the solar tides amount to 45% of the moon tides. Usually the tidal acceleration is not described using the zenith angle Z_s, it is more convenient to use an Earth-fixed coordinate system with φ and λ as geocentric latitude and longitude and introducing the tide-generating body by its equatorial coordinates (h_t = hour angle, δ_t = declination). That leads from Eq.2.59 to:

$$\frac{\delta V_t}{\delta r} = \frac{3}{2} GM_t \frac{r}{r_t^3} [3(\sin^2\varphi - \frac{1}{3})(\sin^2\delta_t - \frac{1}{3}) + \sin 2\varphi \sin 2\delta_t \cos h_t + \cos^2\varphi \cos^2\delta_t \cos 2h_t]\,. \tag{2.60}$$

Equation 2.60 contains various time-dependent functions which are not well suited for tidal analysis. But fortunately the tides can be expressed as a harmonic expansions, so that the tidal acceleration then follows a sum of time dependent cosine functions of constant frequency and amplitude. Some of the most important tides can be found in Tab. 2.1. The IERS

Conventions, 2003 (McCarthy and Petit, 2004) contain 62 tidal waves.

Table 2.1: Principal tidal waves

Symbol	Name	Period T	Amplitude at φ =45°, h_t=0
long-periodic waves			
M0	const. lunar tide	∞ h	102.9 nm s^{-2}
S0	const. solar tide	∞ h	47.7 nm s^{-2}
diurnal waves			
O1	main diurnal lunar tide	25.82 h	310.6 nm s^{-2}
P1	main diurnal solar tide	24.07 h	144.6 nm s^{-2}
semi-diurnal waves			
M2	main semi diurnal lunar tide	12.42 h	375.6 nm s^{-2}
S2	main diurnal solar tide	12.00 h	174.8 nm s^{-2}

2.3.3 Earth tides

In response to the lunisolar gravitational attraction, the solid Earth undergoes an elastic deformation, i.e. tidal variations of its mass distribution resulting in variations of gravity and of the height of equipotential and solid surfaces. This direct response is called gravimetric Earth tide or Earth body tide (Fuchs and Soffel, 1984). For a spherically symmetric, non-rotating, elastic earth model the response to the tidal forcing field is described by Loves theory (Love, 1909).

The tidal potential V_t causes in point P a radial shift of Δr_{el} of the equipotential surface (see Fig. 2.21). If the Earth were completely plastic it would now try to reach the same shape as this equipotential surface.

But because of its rigidity it does not reach the same shape and conforms only partially to the equipotential. This deformation causes an additional deformation potential V_d and therefore also a further change of the equipotential surface. V_d and Δr_{el} are proportional to V_t (Torge, 1989). The tidal potential of the elastic Earth V_{el} follows as:

$$V_{el} = V_t + V_d + g\Delta r_{el} = V_t(1 + k - h) \tag{2.61}$$

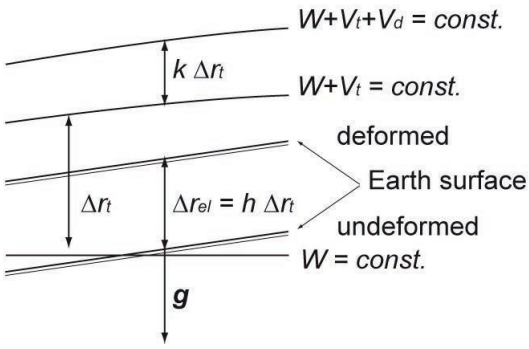

Figure 2.21: Vertical shift of the solid Earth and its level surface caused by tidal potential.

with k being the first Love number (Love, 1909) and h the second, both depending on the degree of the spherical harmonic expansion. The Love numbers h and k are dimensionless parameters that describe the rigidity of a planetary body and the susceptibility of its shape to change in response to a tidal potential, introduced by Augustus Edward Hough Love in 1911. Later, in 1912, T. Shida (Shida, 1912) added a third Love number, l, which was needed to obtain a complete overall description of the solid Earth's response to the tides. The moon can introduce a maximum change in the orthometric height (distance along a plumb line from a point at the physical surface to the geoid) of about 35 cm, the sun of ca. 17 cm.
Additionally to the varying tidal deformation a permanent deformation exists, the so called permanent tide, which is caused by the simple presence of moon and sun. Honkasalo (1964) found that the tide-free gravity, which demands the removal of the permanent tide, does not represent the time-average of the acceleration of the free fall, hence he restored the permanent tide. In this way, only the truly cyclic tidal elements were removed. This approach is called a 'mean tide' system. But it violates the theory that called for removal of all external masses when computing the equipotential surface of the Earth (Heikkinen, 1979). This lead to the first IAG resolution, were it was recommend to not apply the Honkasalo correction, meaning, the permanent tide should be removed. However, the discussion is still ongoing, the actual IERS Conventions 2010 (Petit and Luzum, 2012) state the following:

> Resolution 16 of the 18th General Assembly of the IAG (1984), recognizing the need for the uniform treatment of tidal corrections to various geodetic quantities such as gravity and station positions," recommended that the indirect effect due to the permanent yielding of the Earth be not removed," i.e. recommends

No. 36 IERS Technical Note 1 General definitions and numerical standards the use of "zero-tide" values for quantities associated with the geopotential and "mean-tide" values for quantities associated with station displacements. This recommendation, however, has not been implemented in the algorithms used for tide modeling by the geodesy community in the analysis of space geodetic data in general. As a consequence, the station coordinates that go with such analyses are "conventional tide free" values.

2.3.4 Ocean loading tides

Oceanic tides cause additionally to their direct attraction due to the water masses a change in gravity due to loading effects evoked by the mass shift and the induced vertical surface displacement (Torge, 1989; Scherneck, 1991). For example, a high tide causes a depression with a related increase in gravity which decreases with increasing distance from the shore. In South-West England, vertical ground displacements due to tidal loading can range over 10 cm (Penna et al, 2008) and displacement gradients can be larger than 3 cm per 100 km, leading to changes in gravity up several tenths of micro-gals (10^{-8} ms^{-2}) in the vicinity of the Irish Sea (Baker, 1980). The ocean tide loading on an elastic Earth can be determined with analysis of VLBI and GPS time series (Schuh and Moehlmann, 1989; Vey et al, 2002) or modeled using the help of ocean tide models (Egbert and Erofeeva, 2002). For the latter a common approach uses the Green's function formulation (Farrell, 1972), considering the ocean load as a thin layer and expanding it into spherical harmonics (due to the strong spatial variation up to very high degrees n=10000). In this case the perturbations of the gravitational potential are described by the degree dependent load Love numbers h' and k' first determined by Farrell (1972). The loading effect can then be calculated analogous to the Earth tides (Eq. 2.61).

2.3.5 Mass changes in the System Earth

Besides all the tidal effects there are several other sources for gravity changes within the Earth, especially due to mass displacements near the surface. Sources can be seismic earthquakes or volcanic or tectonic movements leading to changes in gravity up to 10^4 nm s^{-2}.

But also man made mass displacements, for example mining, constructions and also depletion of water, oil or gas, can introduce considerable gravity variations (100 nm s^{-2}). Changes in the ground water level can have similar impacts (Torge, 1989). All these variations occur on different temporal and spatial scales. While earthquakes lead to a sudden and permanent change in gravity, ground water variations introduce a periodic- or quasi-periodic variation from days to years, the post glacial rebound, also called or glacial isostatic adjustment (ascent of land masses due to the elastic response of the Earth crust after the melting of the ice sheets), on the other hand shows a secular trend covering centuries (Stacey and Davis, 1977; Peltier, 2008).

Events that have an impact on more than 10^4 km are considered global, in this category fall changes in the eccentricity of the Earth core, mass transport processes in the mantle, plate movement but also sea level rise. The post glacial rebound is considered a regional effect, together with tectonic processes such as mountain building. The effects in both categories progress secularly or in a long term time span of thousands to million years. Local changes in the range of several kilometers are related mostly to earthquakes, volcanoes and other mass displacements on the surface like landslides but also changes in the ground water and other hydrological variations including non-tidal effects in the ocean (e.g. El Niño). Such effects cover time-spans from seconds to several years.

Chapter 3

Atmospheric effects on the gravity field of the Earth

3.1 Physical and meteorological fundamentals

The following chapters give a brief introduction to the structure and basic physical relationships of the atmosphere. It is designed to provide solely the fundamental information and equations and cannot be considered as complete.

3.1.1 Structure of the atmosphere

The atmosphere is a gaseous hull enclosing the Earth consisting of various gases, mainly nitrogen (78%) and oxygen (20%). The atmosphere is in hydrostatic equilibrium and subjected to the Earth gravity. No clear upper boundary is defined, the atmosphere passes continuously over to interplanetary space. In case of gravimetric correction the lower 60-80 km are of interest, i.e. the troposphere, stratosphere and mesosphere, where most of the masses are concentrated. Figure 3.1(a) and 3.1(b) show the progression of the density and virtual temperature (temperature which a sample of dry air must have in order to have the same density as a sample of moist air at the same pressure, see Eq. 3.2) at Vienna for the first 65 km using ECMWF (see. Chap. 3.2.1) data of 01.January, 2008 00 UTC.

The lower two layers, i.e. the troposphere and stratosphere, are separated by the tropopause

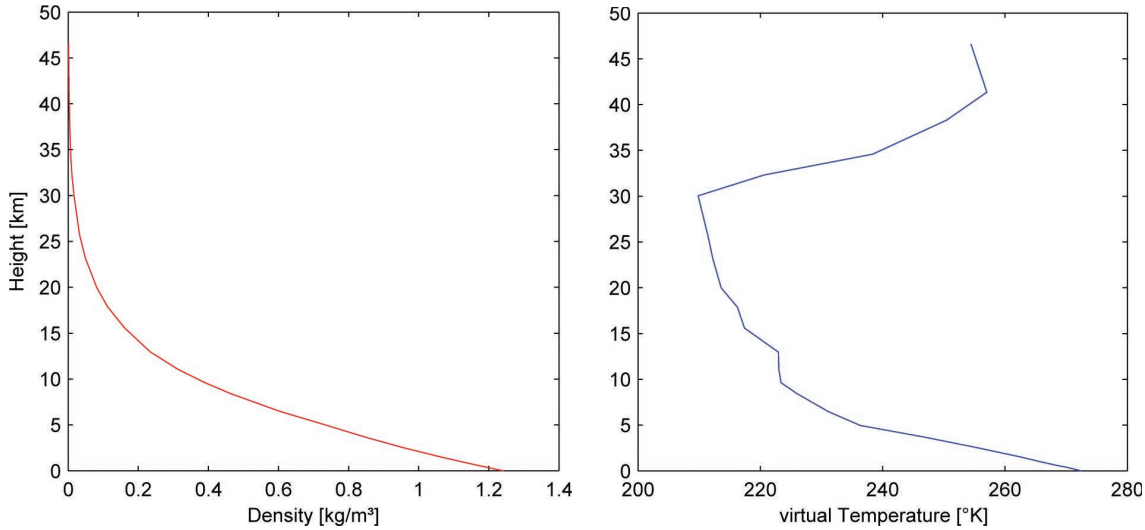

Figure 3.1: **a)** Progression of the density with height and **b)** of the virtual temperature at Vienna (48N, 16E)

which mean height and temperature changes in dependence on geographical latitude and time of the year. At mid latitudes it lies approximately in 10 km height, but it can vary between 6 km an 13 km depending on the temperature. In the tropics it is around 17-18 km, beyond the polar circle in ca. 6-8 km. The source of the change in height of the layer is due to the heating of the air during summer and the resulting ascent of the masses to larger heights, and because of the oblateness of the Earth caused by the centrifugal force, which is also acting on the atmosphere (Ahrens, 2005).

3.1.2 Pressure, temperature, density and height

The gas mixture air has at each point of the atmosphere a certain pressure, temperature and density. If the ratio of the gases in the mixture is known together with two of these variables, the remaining one can be determined with help of the general gas equation of state (Eq. 3.1), showing the relationship between the temperature T, the pressure p and the density of a gas ρ. The following formulae can be found in e.g. Jacobson (1999).

$$p = \rho R_L T_v \tag{3.1}$$

with R_L = 287.05 Jkg^{-1} K^{-1} being the specific gas constant for dry air. An important role in the composition of the air has the water vapor. Its a quantity, that describes the ratio between the total mass of the moist air and the water vapor, called the specific humidity q, defined in Eq. 3.7. The moist air is composed of dry air and water vapor and is subject to greater variations. For moist air with the specific humidity q the virtual temperature T_v can be computed from the temperature T as follows

$$T_v = T(1 + 0.608\, q)\,. \tag{3.2}$$

Every moist air parcel has a temperature at which the density of the humid air is equal to the density of the dry air. This temperature is referred to as virtual temperature. It also follows that moist air behaves like dry air with the virtual temperature and meaning the standard formulas established to dry air can be applied without having to consider the humidity.
As pressure we understand the force which is imposed by the air masses on a surface. Since the air pressure can be attributed directly to the weight of the air column, it decreases with increasing height. Thus we find the air pressure p at height z and $p - \mathrm{d}p$ at the height $z + \mathrm{d}z$. The Eq. 3.1 becomes the hydrostatic equation,

$$\mathrm{d}p = -\rho g \mathrm{d}z\,, \tag{3.3}$$

with g as a height-dependent acceleration of gravity. The density ρ is both height and temperature-dependent. The elimination of the density in Eq. 3.1 with Eq. 3.3 leads to

$$\frac{\mathrm{d}p}{p} = -\frac{g_n}{R_L T_v}\mathrm{d}z\,, \tag{3.4}$$

its integration yields

$$p = p_0\, e^{\left(-\frac{H g_n}{R_L T_v}\right)}\,. \tag{3.5}$$

Here g_n = 9.80665 ms^{-2} is the mean gravity value on the geoid, H the height above sea level and p_0 = 1013.25 hPa the air pressure at sea level. The relationship in Eq. 3.5 is also known as barometric formula and shows the exponential decrease in air pressure with height.
The difference between the virtual temperature T_v and the actual temperature T is generally in the order of 1°K. In the extreme case of 7°K a gravitational effect of 1 nm s^{-2} can be

caused, see Kroner (1997).

Inserting Eq. 3.2 in Eq. 3.1 we obtain for the density of the moist air

$$\rho = \frac{p}{R_L T_v (1 + 0.608q)} . \tag{3.6}$$

According to the definition of specific humidity q the following relationship between the density of water vapor and the density for humid air is established

$$q = \frac{\rho_{water\ vapor}}{\rho_{humid\ air}} = \frac{0.622e}{p - 0.378e} , \tag{3.7}$$

with the vapor pressure e, composed of the relative humidity r and the saturation vapor pressure E

$$e = \frac{r}{100E} . \tag{3.8}$$

E was defined by (Balton, 1980) at a given temperature T in °C as

$$E = 6.112e^{\frac{17.67T}{T+243.5}} . \tag{3.9}$$

The geopotential V in a certain point of the atmosphere is defined as the work that needs to be done to move a unit mass against the gravity from the sea surface to a certain point. The height H of the potential surface above sea level can be determined with the mean gravity g_n (Liljequist and Cehak, 2012)

$$H = \frac{V}{(1 - k\cos 2\phi) g_n} \tag{3.10}$$

with $k = 0.002637$ and ϕ as latitude. The term in brackets takes into account the contribution of the Earth oblateness to the gravitational acceleration. ,

3.1.3 The atmospheric pressure and its variation

The mass changes within the atmosphere, i.e. the gaseous part of the system Earth, contribute to the total mass exchange inside the entire system. However, there is no possibility for geodesy to separate the individual components through gravity field observations. Various authors have tried to estimate the total mass of the atmosphere evaluating

different global pressure fields, using the fact that pressure reflects directly the mass of the atmosphere (Ekholm, 1902; Trenberth and Guillemot, 1994; Trenberth and Smith, 2005).

The estimates of the authors vary significantly, starting from $5.16 \cdot 10^{18}$ kg to $5.32 \cdot 10^{18}$ kg. One reason for this are the different approaches used for atmospheric sciences and for geodesy. A second reason are the different models used, and the changes within the models themselves (Gruber et al, 2009). Most of the recent studies however, show a slight increase in the atmospheric mass over the last decades that can be associated with an increase of water vapor. Figure 3.2 shows a time series of the global mean surface pressure from the ECMWF operational analysis and re-analysis data over 30 years, where the most prominent signal is the yearly variation.

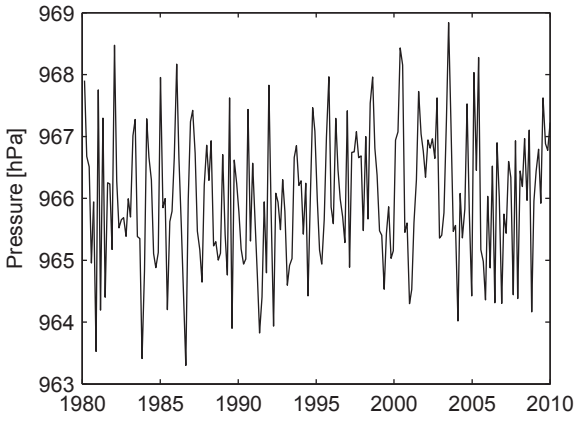

Figure 3.2: Global mean surface pressure in hPa from ECMWF analysis (1980-2009) pressure level data reduced to surface topography

The degree 0 coefficient of the atmospheric potential field is directly linked to the total mass of the atmosphere. Figure 3.3 shows the time series of the mass change obtained from the C_{00} atmospheric gravity coefficient of the years 1980 until 2009. The yearly signal is clearly visible, also a linear trend can be calculated for the whole time period (red line), which suggests an increase of the atmospheric mass of $3.26 \cdot 10^{13}$ kg/year. But this conclusion has to be treated with caution, because as the chosen time period changes, the trend can change considerably too (cyan, green and blue lines).

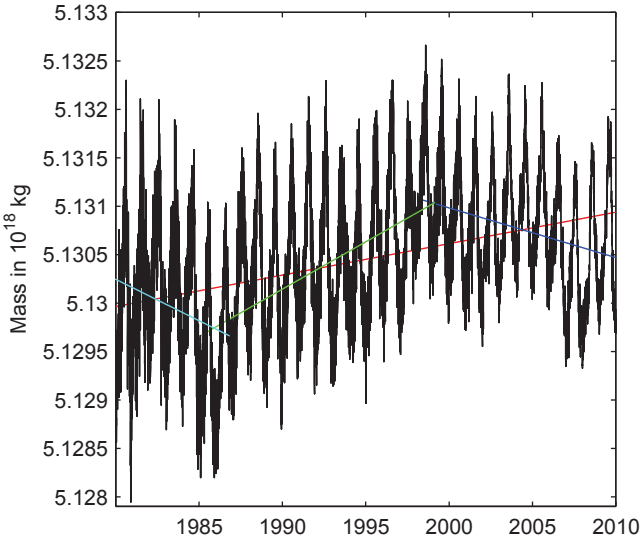

Figure 3.3: Global mass change of the atmosphere obtained from C_{00} based on ECMWF operational analysis (1980-2009) pressure level data reduced to surface topography

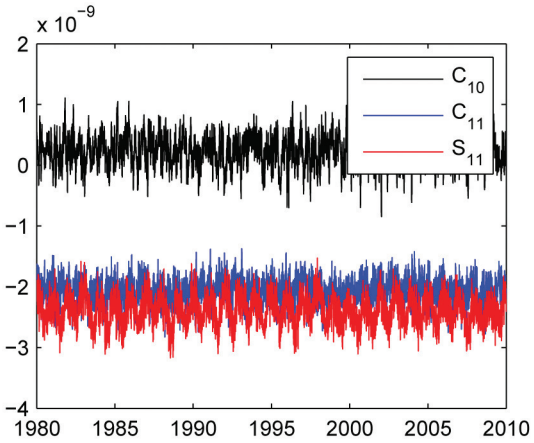

Figure 3.4: Degree 1 coefficients using the thin layer approach, based on ECMWF operational analysis (1980-2009) pressure level data reduced to surface topography, in black C_{10}, in blue C_{11} and in red S_{11}

Figure 3.4 shows a time series of the degree 1 coefficients C_{10}, C_{11} and S_{11} which are closely tied to the center of mass (see Eq. (2.30)). In contrast to the mass, in this time series no significant trend becomes evident, although other studies (Gruber et al, 2009) show changes of the geocenter up to 2.6 mm per year in x-, 0.8 in y- and 6.7 in z-direction.

Although the change in the global mean of the atmospheric mass is small (the range for the 30 years in Fig. 3.2 is 5.5 hPa), the changes within smaller time and space scales can be of

several tens of hPa. Such changes in the atmosphere are responsible for one of the largest signals in the time variable gravity field (Warburton and Goodkind, 1977). Typically, the surface pressure variations are larger in mid and high latitudes, whereas in tropical regions they are rather small. Figure 3.5 shows the RMS pressure variability using ECMWF surface pressure data for 2008.

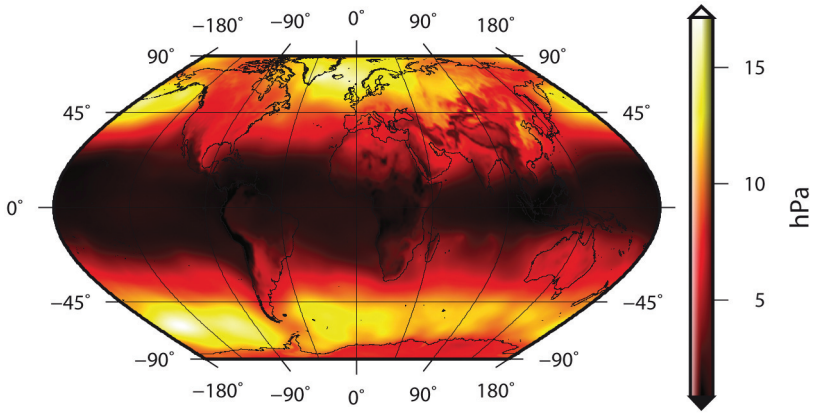

Figure 3.5: RMS of ECMWF surface pressure over the year 2008

Generally atmospheric phenomena can be categorized based on their time variability. One class consists of long term variations, such as seasonal, annual and inter-annual variations. The global atmospheric pressure cycle (Fig. 3.2), the seasonal variation between northern and southern hemisphere or mass transport between land and ocean such as the monsoon fall into this category. The El Niño southern oscillation (ENSO) classifies for inter-annual variations (McPhaden, 2002), just as the North-Atlantic Oscillation (NAO) (Hurrell and van Loon, 1997) .

The second class contains short term variations, containing signals like the diurnal and semi-diurnal solar tides (see Fig. 3.6(a),3.6(b)). But the most prominent variations are introduced by (anti-) cyclones, which can reach 50-60 hPa in central Europe (Rabbel and Zschau, 1985) within a few days, in Scandinavia even 80 hPa. But also extreme events such as hurricanes fall into this class. At the center of a hurricane the pressure can drop by 100 hPa within hours.

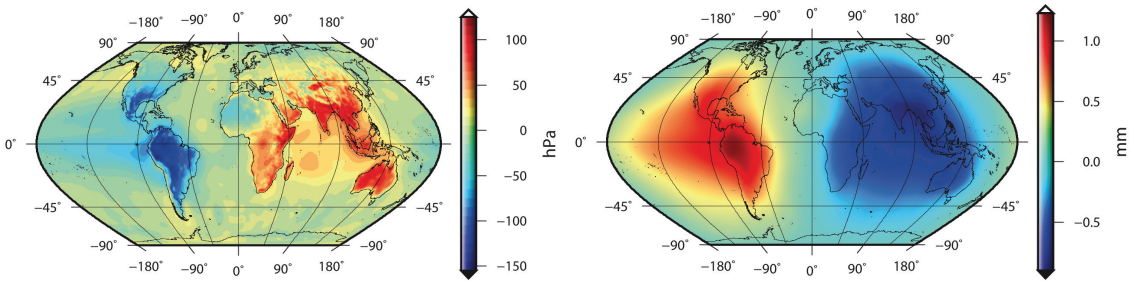

(a) (b)

Figure 3.6: **a)** S1 tide at 00 UTC in hPa. **b)** Corresponding effect on geoid in millimeter

3.2 Meteorological analysis-models

This chapter gives an introduction in the field of atmospheric modeling and weather prediction. Different approaches and types of models will be discussed, using models from the European Centre for Medium-Range Weather Forecast (ECMWF) and the National Centers for Environmental Prediction (NCEP).

3.2.1 Numerical weather models

The main quantity for meteorologist is the pressure, because compared to other properties, pressure is the least variable one. For temperature or humidity, a small change in the location can introduce a considerable error (Jacobson, 1999). Generally, there a two methods to obtain the pressure values at a certain location, one is from in-situ measurements using barometers, anemometers, radiosondes etc. An other one is to obtain such data from numerical weather models (NWM). The most widely used NWM models are those from ECMWF `http://www.ecmwf.int/` and NCEP `http://www.ncep.noaa.gov/`.

In the beginning of the 20th Century the Norwegian physicist and meteorologist Vilhelm Bjerknes was the first to propose to describe the dynamic processes in the atmosphere with exact thermodynamic and hydrodynamic equations. The realization of this idea had to wait until the mid 50's until the first computers were developed and a network consisting of several weather stations was established. Soon it became clear, that the modeling of atmospheric events was far more complex and more difficult than initially anticipated. The first numerical models were quite simple and based solely on elementary equations. The first global

model was established in 1966 and consisted of a 300-km grid and six levels for the vertical discretization.

Modern numerical forecast models are based on a formulation of the dynamic equations, which are referred to as primitive equations (Grammeltvedt, 1969). These models are designed to predict the future state of the atmosphere by modeling the dynamic and physical processes. To integrate the dynamic equations, accurate initial conditions are required. These are obtained from various observations, such as ground weather stations, radiosondes, ships, aircrafts and weather satellites. Here one of the limiting factors for NWM manifests; namely meteorological observations, especially near the ground and in the lower layers, where the atmosphere is most variable, are not evenly distributed over the globe. Big gabs can be found over the oceans, the polar regions and in developing countries.

The process of integrating the observations into the model analysis is called assimilation. Within this process the observations are checked for errors and then interpolated to the internally used grid format and combined with a first guess from previous forecasts. The resulting grid then represents a best approximation of the true state of the atmosphere at a given time. The variables in the models are represented by either grid or spectral forms. Currently, most of the global operational models utilize spectral models for better computational efficiency. Various grid models are then derived from them on global, regional or limited-area scales.

The vertical discretization is generally realized through individual layers, implemented as model or pressure level data. The ECMWF model level data presently consist of 91 model levels. The concept of model levels addresses the problem of discontinuities in the atmosphere, for example mountains, by creating atmospheric levels that follow the contours of the Earth's surface in the lower and mid-troposphere, the so-called orography (see Chap. 3.2.2). In high altitude the effect of the orography diminishes until the layers in the upper atmosphere become parallel to layers of constant pressure. From the model level data the so-called pressure levels are retrieved, where the vertical discretization is implemented within ECMWF through 25 levels instead of 91, following continuous surfaces of equal pressure from 1000 hPa to 1 hPa, which can also lie underneath the topography. At each level, among other parameters, the temperature, the specific humidity, and the geopotential

height are available.

Generally, besides forecast products, two kinds of analysis products are available: operational analyses and reanalysis. The assimilation method of operational analysis is constantly evolving as time goes on. Variations of the initialization methods, physics, grid resolution, data availability, and handling techniques will disrupt the consistency and the continuity of the analysis. To provide a consistent dataset, many organizations established their own project to produce the re-analyzed fields for various time spans such as the ECMWF 40-year re-analysis (ERA40) and NCEP reanalysis. In these products, the assimilation schemes do not change over time, but the observations will change due to the data availability over time (e.g. no satellite data in the past).

3.2.2 Topographical effects on the surface pressure

The terrain in numerical weather models usually does not follow the 'real' topography but the so called model orography which is derived from digital elevation models using various methods, such as mean orography (average of the terrain data inside a model grid box), envelope orography (cover all but the very sharpest peaks) or silhouette orography (averages only the tallest features in each grid box). Additionally, due to the fact that most NWM use spherical harmonics in their internal computation, and therefore also for the representation of the topography, the Gibbs phenomenon caused by the truncation of the spherical harmonics, may lead to ripples in areas of rapid elevation changes. The usage of different land-sea masks can cause further discrepancies near the coasts. Also the accuracy of the conversion from the 3D global analysis data to surface pressure is greatly affected by the complexity of the land topography. Figure 3.7 shows the difference between ETOPO5 topography and ECMWF orography on a 1° x 1° grid.

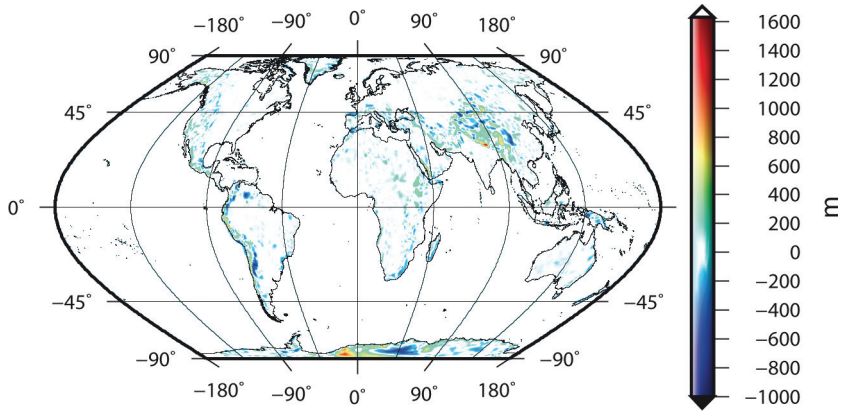

Figure 3.7: Difference between ETOPO5 topography and ECMWF orography on a 1° x 1° grid.

Since the topography alters the flow of the atmosphere, the real topography is adjusted or smoothed to best fit the physical model and its resolution. Sometimes, biases exist between the real and the artificial model surface pressure, i.e., the surface pressure from the NWM model is different from the surface pressure on the real physical Earth. Figure 3.8 shows the surface pressure at the Conrad Observatory for January 2008 retrieved from ECMWF on the orography in green, ECMWF reduced to Etopo5 in red, from the German weather service DWD (Deutscher Wetter Dienst) in blue and from in-situ measurements in black.

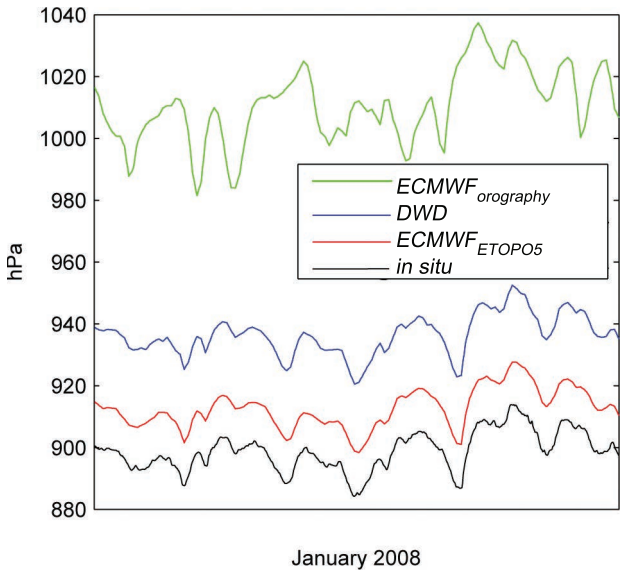

Figure 3.8: Surface pressure at the Conrad Observatory for January 2008: in green ECMWF on the orography, in red ECMWF reduced to Etopo5, in blue DWD and in black in-situ measurements.

Although some NWM analysis products directly include the surface pressure, most of the time these values are not suitable to be used directly, as can be concluded from Fig. 3.8. That is one reason we choose for our study to use ETOPO5 as topography and to reference all the quantities given by ECMWF to that surface. The exact procedure is given in Chap. 4.2.

3.2.3 The mean state of the atmosphere

For several geodetic application a clear unambiguous definition and accurate calculation of a mean state of the atmosphere, i.e. a global reference pressure field, is essential. Examples are the determination of the Earths surface deformation due to atmospheric pressure loading (Rabbel and Zschau, 1985; van Dam and Wahr, 1987; Boy and Chao, 2005), precise calculation of the Earths time-variable gravity field due to atmospheric mass redistribution (Boy et al, 2009), de-aliasing of gravity mission satellite data (Flechtner, 2007), accurate determination of the geocenter variations due to redistribution of the total Earths mass (Dong et al, 1998; Chen et al, 1999), and determination of the total atmospheric mass (Trenberth and Smith, 2005; Gruber et al, 2009), as well as its seasonal variations (Hoinka, 2012).
In most geodetic applications so far, the reference pressure values have been usually determined by averaging global surface pressure data over a certain period, e.g. 2 years of ECMWF data (Flechtner, 2007), or 22 years of NCEP data (Petrov and Boy, 2004). As different data periods and data providers are used, the determination of the reference pressure values is ambiguous and the results may not be consistent with each other. To develop a consistent reference pressure Plag et al (2007) proposed to transform the pressure values obtained from the NWM from the orography onto an topography model. Following the recommendations discussed in Böhm et al (2008) a new method for the calculation of reference pressure values has been designed in the frame of the project GGOS Atmosphere. For that purpose it was decided to use ECMWF 40 years re-analysis (ERA-40) atmospheric monthly mean pressure level data as the basis for determining the global reference pressure on a 0.5° x 0.5° global grid using ETOPO5 as topography. It is plotted in Fig. 3.9 and the exact processing strategy adopted can be found in 4.2.

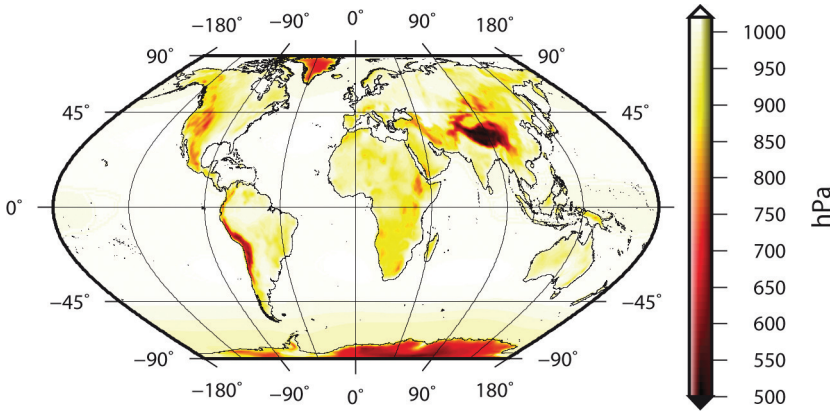

Figure 3.9: Global Reference Pressure

3.2.4 Error estimation

In order to investigate the time-variable gravity field, atmospheric effects have to be removed beforehand. Especially for satellite missions such as GRACE (Chap.2.2.3) but also for ground measurements, the basis for that procedure are NWM, which are considered up till now, together with all used background models, as error free. Velicogna et al (2001) compared surface pressure from ECMWF and NCEP with in-situ measurements and showed that the accuracy of the models is around 1-1.5 hPa and concluded that these models are suitable to remove the atmospheric contribution from the GRACE estimates. In order to recover the continental hydrological signal with an accuracy of 1 hPa or better.

However, one reason that the GRACE gravity field models have not reached their ultimate accuracy is seen in the de-aliasing process (see Chap. 3.3.1 and 4) and the uncertainties of the atmospheric models applied during that procedure. These findings were confirmed in more recent studies by Zenner et al (2010), which showed that the choice of the error map of the surface pressure can change the monthly gravity fields on a regional scale up to 1.6 mm in terms of geoid height. Hence the error maps have to be determined carefully.

ECMWF provides 6-hourly surface pressure errors representing conservative estimates derived during the modeling, taking into account meteorological phenomena but not unknown events like sudden evolutions of unpredicted low pressure fields. Generally the ECMWF error maps are considered to be too optimistic, being a pure outcome from weighted combination of measurements and model predictions. Another method to derive error maps, is by

determining the difference between ECMWF and NCEP surface pressure fields, as shown in Fig. 3.10. Problem here are the different temporal and spatial resolutions of the models, as well as the different background models and topographies used in the model determination. Further on, some of the errors in the models are partially correlated (Wahr et al, 1998; Velicogna et al, 2001) Although on the present GRACE error level, these effects are too small when looking on a global sclale as they lie below the actual GRACE error level. Nevertheless regionally the effects are within the GRACE sensitivity and can effect GRACE results on a significant level, thus making the determination of more accurate and realistic error values as well as uncertainties one of the main issues to be solved for the next generation gravity field missions (Zenner et al, 2012).

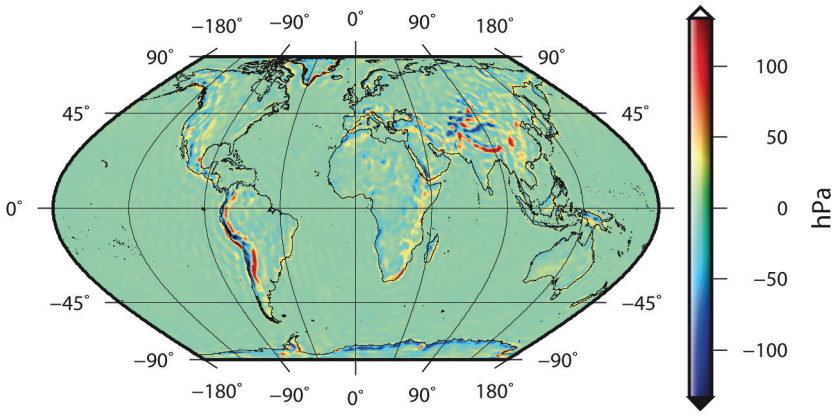

Figure 3.10: Difference between ECMWF and NCEP surface pressure on a 1° x 1° grid. NCEP is interpolated linearly from a 2.5° to a 1° grid.

3.3 Impact of the pressure variation on the gravity field

Gravimetric measurements are influenced by variations in the density within the atmosphere and thus the gravitational attraction of the air masses. The direct effect, i.e. the attraction of the air masses, gives the main contribution to the changes in gravity. Additionally the Earths crust as well as the ocean bottom (although on a much smaller scale) get elastically deformed when subject to the loading of air masses. This again causes a shift in the mass distribution within the crust and of the crust itself. This is a large-scale effect, also called indirect effect, and usually acts reverse to the attraction of the atmosphere. All these effects influence space borne as well ground based gravity measurements and have to be considered thoroughly.

3.3.1 Atmospheric aliasing

Exploring the Earth gravity field requires the removal of short term mass variations in the system Earth, including all solid, liquid and atmospheric particles. Due to the fluctuation of those masses at various temporal and spatial scales (like high and low atmospheric pressure systems) as well as due to a strong dependency on the sampling rate of the ground track of the satellite, a long observation time does not guarantee that the introduced variations in the gravity field are canceled out by the mean operator. This effect is called aliasing and is caused by the fact that the sampling frequency is lower than the highest frequency of the signal. Figure 3.11 shows the effect of some of these mass variations in terms of degree standard deviations with respect to the theoretical performance of the three gravity satellite missions CHAMP, GRACE and GOCE (see Chap. 2.2.2). Thus de-aliasing means incorporating such instantaneous variations in the atmospheric masses with respect to a static mean state of the atmosphere and correcting for them, either during the preprocessing of observations or during the estimation procedure of the gravity field solution.

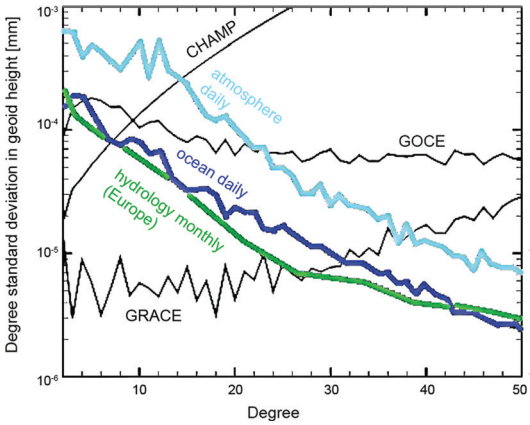

Figure 3.11: Gravity variation signals from different sources in terms of degree standard deviation, in cyan daily atmosphere, blue daily ocean, green monthly hydrology, compared to mission sensitivities of CHAMP, GRACE and GOCE, modified from Flechtner (2007).

Among those signals, the atmosphere has the largest contribution, therefore good atmospheric de-aliasing models are crucial. The mostly used way to reduce aliasing is by help of NWM (Flechtner, 2007). Thompson et al (2004) examined the impact of the short-period, temporal mass variation on the GRACE monthly estimate. It is found that the degree error relative to the measurement error increases by a factor of 20, due to the atmosphere aliasing,

and that the de-aliasing gives the greatest reduction in aliasing errors for the coefficients in mid-degrees and higher. It is important that the background models used in the GRACE processing contain a reasonably accurate representation of the high frequency content in the atmosphere, as otherwise the result will be deteriorated significantly, especially for the lower degrees (see Fig. 3.11.

Similar conclusions can be drawn for atmospheric corrections for SG, where this matter is even more crucial, as far smaller signals are to be detected, i.e. eigenmode of the Earth core or its self-oscillation.

3.3.2 Atmospheric tides

As mentioned in Chap. 3.1.3, the amplitude of the barometric tides can reach several hPa (see Fig. 3.6 for S1). These global-scale oscillations of the atmosphere are generated mainly by the periodic heating of the atmosphere by the Sun. Zonally symmetric forcing of the atmosphere produces the migrating tides with periods harmonic of a 24 hour day and phase velocities that match the apparent motion of the sub-solar point. Migrating tides are the sun-synchronous tides, propagating westwards with the apparent motion of the sun. The non-migrating tidal components, which are much smaller than the migrating component, show the same periods as the migrating tides but do not follow the apparent motion of the sun. The reason behind it can lye in the topography, the land-sea contrast and other surface interactions as well as latent heat release due to deep convection in the tropics (Lindzen, 1979). The most dominant barometric tides are diurnal (S1) and semi-diurnal (S2) tides, with a larger amplitude for the semi-diurnal tide. The tri-diurnal tide (S3) is one order of magnitude smaller. Figure 3.12 shows the effect of the S2 and S3 (tri-diurnal) tides on the geoid.

In this research three-hourly pressure level data from the so-called Delayed Cut-off Data Analysis (DCDA) from ECMWF over the time period from 2005 to 2011 with a spatial resolution of 1° was used. The cut-off time is the latest possible arrival time for meteorological observations to be incorporated in an analysis cycle. Six-hourly and twelve-hourly analysis cycles are combined with short-term forecasts, so that the cut-off time can be delayed. A further characteristics is a higher temporal resolution of 3 hours that makes use of the short-term forecasts. Using this data it is possible to consider both migrating and non migrating

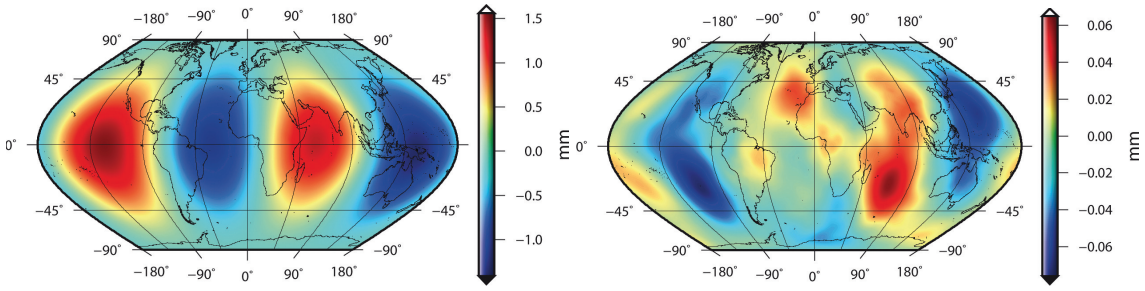

Figure 3.12: **a)** S2 and **b)** S3 tide at 00 UTC expressed in geoid height in millimeter.

tidal components. Furthermore, the three hourly sampling of the data permits a proper determination of the S1, S2, and S3 atmospheric tides. A global gridded model of the pressure tides was developed using the annual mean model described in Ponte and Ray (2002).

3.3.3 Atmospheric loading and the indirect effect

The indirect effect of the atmosphere on the gravity field, i.e. the elastic deformation of the solid Earth due to atmospheric loading, is counteracting the direct effect due to the deformation towards the geocenter. In general, for small deformations the additional change in the potential ΔV depends linearly on the potential, following Farrell (1972):

$$\Delta V_n^{ind} = k_n \Delta V \,, \tag{3.11}$$

$$\Delta V_n^{tot} = \Delta V + k_n \Delta V = (1 + k_n)\Delta V \,, \tag{3.12}$$

k_n denote the degree dependent load Love numbers and represent the deformation behavior based on the rheology of the Earth.

Loading introduces generally effects on a large spatial scale since the Earth's elastic surface deformation due to mass redistribution is mainly sensitive to large scale pressure variations with wavelengths greater than 2000 km, corresponding to $n < 10$ (Boy et al, 2001). Figure 3.13 shows the indirect effect for 01.01.2008 at 00 UTC. A more detailed insight in the processing is given in 4.3.3.

SGs of course see the indirect effect too, which only amounts up to 5% of the total atmospheric signal. With growing distance from the station, the influence of the indirect effect increases (see Fig. 3.14, (Neumeyer et al, 2004)), whereas the direct effect decreases. How

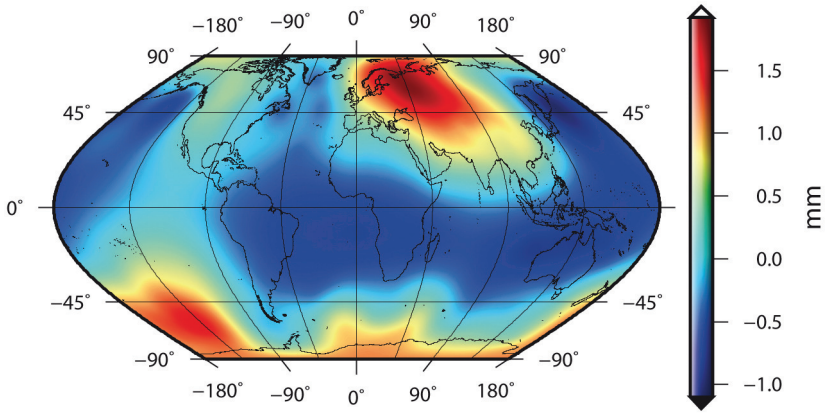

Figure 3.13: Difference of the geoid height variation in millimeter for the thin layer approach between the variant with and without loading for January 1, 2008, 00 UTC

this effect is dealt with in practice is explained in Chap. 5.1.6.

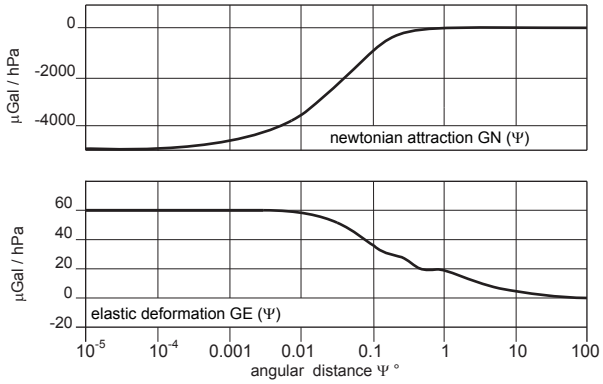

Figure 3.14: Newtonian and elastic contributions of the atmosphere to gravity changes (modified from Neumeyer et al, 2004)

3.4 The atmosphere and the ocean

Generally, the ocean responds to atmospheric forcing like wind, pressure, evaporation, precipitation, and radiation from the Sun. The responses are classically divided into barotropic and baroclinic components (Higdon, 2008). Barotropic is the depth-independent part of the flow. In classic wind-driven ocean circulation theory, it is the flow that results from, or is in balance with, a sea surface slope. Baroclinic is the depth-dependent part of the flow and results from the density distribution within the ocean and tries to cancel the sea surface flow. Commonly the barotropic motions are fast (hours to days) such as tides, although they in-

clude a small baroclinic contribution. The El Niño (Hurrell and van Loon, 1997) for example is a mainly baroclinic phenomenon with its slow motions.
Compared to the atmosphere, the time-variable mass signal of the ocean is rather small, the RMS surface mass variability is typically only 2-3 cm (Wahr et al, 1998). Still, ocean signals are evident in GRACE data and have to be considered and corrected. There are various ways to model the oceanic response due to atmospheric forcing. Here only a short overview shall be given:

- Non-inverted barometer (NIB): Atmospheric pressure variations are fully transmitted to the sea floor and the oceanic response is the same as for the solid Earth.

- Inverted barometer (IB): Pressure variations in the atmosphere Δp are compensated by static variations of the sea depth and the pressure on the sea floor, ie. the ocean bottom pressure, does not change (Dickman, 1988). In the simplest case IB assumes approximately 1 cm change in water depth due to 1 hPa change in the atmospheric pressure:

$$\delta h_w = -\frac{\Delta p}{\rho_w g_0} \tag{3.13}$$

  where ρ_w is the sea water density, g_0 the Earth mean gravity acceleration, and respectively δh_w the change in sea depth.

  However the ocean does not respond perfectly like the IB assumption, especially in the tropics and in the southern ocean (Ponte and Gaspa, 1999), but also shallow seas or the changing ice coverage in the Arctic pose problems. Those deficiencies are linked to the inability of the model to consider various interactions occurring between the atmosphere, solid Earth and the oceans (Wunsch and Stammer, 1997).

- Ocean models: They can be divided in the same classes as the oceanic responses, i.e. barotropic and baroclinic. Barotropic ocean models assume one density for the whole water column and are forced only by wind and pressure. Although this approach simplifies the ocean to a rather plain model, it has advantages in easier parameterizations and lesser needs in computational power. The PPHA model developed by Pacanowski, Ponte, Hirose and Ali (Hirose et al, 2001) is such a model.

  Baroclinic models on the other hand include vertical changes and also effects intro-

duced by radiation, evaporation, and precipitation. The OMCT (Ocean Models for Circulation and Tides), developed for studying non-linear interactions among tides and the general circulation and used for the de-aliasing of GRACE, is an example for such a model (Thomas, 2002; Dobslaw and Thomas, 2007).

Within this work, due to the lack of a suitable ocean model, the ocean was not considered in any way.

Chapter 4

Mathematical description of the de-aliasing model for GRACE and its validation

In order to eliminate the aliasing signals of the atmosphere the determination of accurate Atmospheric Gravity field Coefficients (AGC) is indispensable. For the determination of AGC it has become state of the art to use high resolution NWM, which take into account the three-dimensional distribution of the atmospheric mass. By subtracting the gravity spherical harmonics of the instantaneous atmosphere from the ones of the mean atmospheric field, the residual gravity spherical harmonic series are obtained. These describe the deviation of the actual gravity field from the mean gravity field due to atmospheric mass variations. Some parts of the following chapter were already published in the paper Karbon et al (2011).
First a glimpse into the GRACE data analysis will be given, to provide an insight into the various processing steps and the role of the de-aliasing in it. In the following sections the applied data processing for the AGC determination as well as a detailed description of the mathematical modeling is presented. The second part supplies comparisons and validations of various models and methods.

4.1 A glimpse into GRACE data analyses

The following explanations shall give a short insight into the GRACE data analysis to emphasize the role of the de-aliasing within the processing as well as when, where and how these corrections are applied, following Gruber and Flechtner (2007). More detailed information can be found in Schmidt (2006) and the GRACE product descriptions down loadable for example at `http://isdc.gfz-potsdam.de/`.

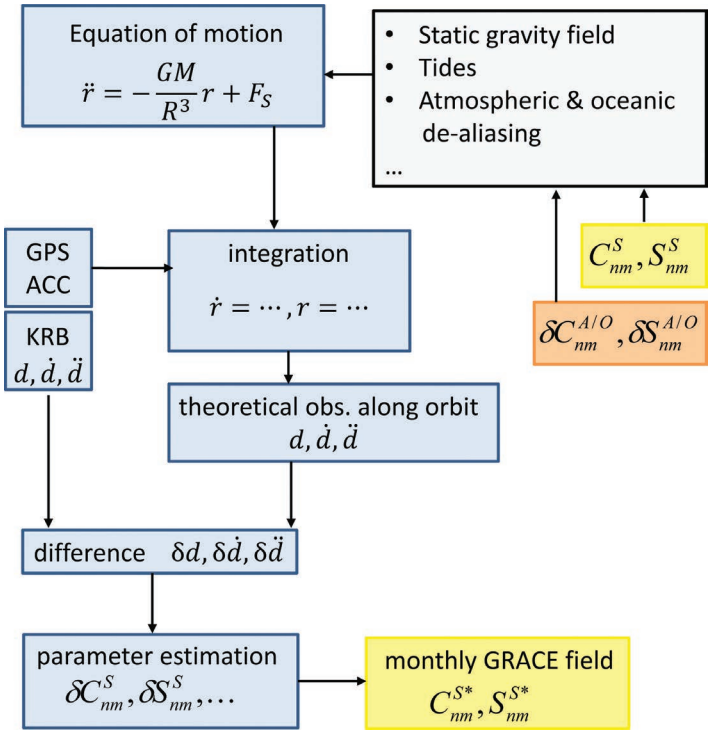

Figure 4.1: Simplified scheme of the GRACE data analysis, modified from Gruber and Flechtner (2007).

Starting point of the processing is the equation of motion which describes the orbit position r of the satellite, where F_s comprises the disturbances acting on the satellite. This includes, among others the static gravity field, summarized in C^S_{nm}, S^S_{nm}, tidal effects, and the non-tidal variation of the atmosphere and ocean with respect to a mean field ($C^{A/O}_{nm}, S^{A/O}_{nm}$), i.e. the de-aliasing products. Non conservative forces like friction introduced through the rest atmosphere at orbital heigt or solar pressure are observed with the accelerometer (ACC) and introduced directly as corrections. The orbit of the satellites can then be determined through numerical integration of the equation of motion from integration of the GPS measurements.

From these theoretical positions of both satellites the distance between both is determined. Since all the disturbing forces are not known to their full extent, these calculated distances differ from those measured by the K-Band Ranging System (KBR) by δd.
These differences are calculated for each step and introduced into the least squares adjustment, the main part of the processing procedure. Here these residuals are referred through a stochastic process to various unknown parameters, such as the static gravity field or calibration parameters of the accelerometer. In general, as more observations are included, more parameters (e.g. a gravity model with larger maximum degree) can be estimated. In case of GRACE one month was defined as standard (Watkins and Yuan, 2007; Bettadpur, 2007; Flechtner et al, 2010) but also 10-day (Bruinsma et al, 2010) as well as weekly- (Flechtner et al, 2010) and daily-solutions are available, although following different processing strategies. The atmospheric and oceanic de-aliasing products are in general considered as error-free, since due to the immense amount of parameters an estimate is hard to accomplish.
Adding the resulting residual gravity model coefficients δC^S_{nm} and δS^S_{nm} to the a-priori static gravity field a monthly GRACE gravity field is obtained.

4.2 Data processing

The appleied processing of the NWM-data shall be introduced on the basis of the determiiation of the atmospheric mean field. As mentioned in Chap. 3.2.3 the determination of the mean state of the atmosphere is a crucial step in the determination of time varying gravity. The global reference pressure (GRP) is based on ECMWF 40 years re-analysis (ERA-40), covering the years 1957 to 2001. This atmospheric monthly mean data set has a horizontal resolution of 1° x 1° on a latitude-longitude geocentric grid and a vertical discretization of 23 pressure levels containing values for the three important parameters, i.e. geopotential Z, specific humidity q, and temperature T (gives the virtual temperature T_v together with q see. Eq. 3.2). To determine the GRP, the following steps are performed:

- The data points given in this 3-dimensional grid are transformed to a set of geocentric coordinates (r_{84}, θ, λ) with respect to the WGS84 ellipsoid by setting the given latitude equal to the geocentric co-latitude θ (see left sketch in Fig.4.2).

- To convert the geopotential height Z (geopotential given by ECMWF divided by the gravity constant of 9.80665 m/s^2 defined by the World Meteorological Organization, with a spherical Earth with radius = 6367.47 km), into an orthometric height H_o and to determine the geocentric radius $r_{el}(\theta,\lambda)$ for a point on a certain level and its corresponding gravity acceleration, a gravity model with its geoid undulation N needs to be introduced. We used the fully normalized coefficients of the tide-free EGM96 up to degree and order 2 for the gravity acceleration and the full set up to degree and order 360 for the geoid undulation as needed for the topography determination (see right sketch in Fig.4.2 and Eq. 4.1). r_{el} of each point P within the levels of the atmospheric column as given by the NWM can be derived from

$$r_{el}(\theta,\lambda) = r_{84}(\theta,\lambda) + H_{el}(\theta,\lambda) = r_{84}(\theta,\lambda) + H_o(\theta,\lambda) + N \tag{4.1}$$

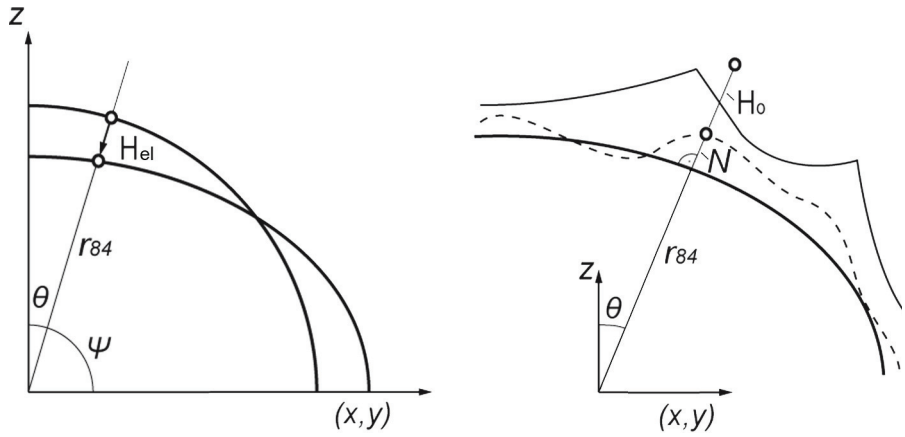

Figure 4.2: On the left the conversion from the sphere to the ellipsoid, on the right the determination of the ellipsoidal height, with the bold solid line depicting the ellipsoid, the dashed one the geoid and the narrow line the topography.

- In order to get realistic values for virtual temperature and pressure at the Earths surface, one has to interpolate the values of T_v and P from the pressure levels onto a digital elevation model. In our case ETOPO5 is used which provides sea level heights on an equidistant grid of ellipsoidal coordinates (with respect to WGS84) with a resolution of $5'$. Preceding the main interpolation onto the Earths surface, two intermediate steps of interpolation have to be carried out:

1. The orthometric heights of the meteorological data are arranged on 1° integer grid nodes of geocentric coordinates. ETOPO5 orthometric heights are available on a similar 1°-integer grid, but referring to ellipsoidal coordinates. Thus, it is necessary to transform the ellipsoidal (ϕ_{el},λ_{el})-grid to its corresponding geocentric (θ_{gc},λ_{gc})-grid and linearly interpolate the orthometric heights for the desired geocentric coordinates (θ_{gc},λ_{gc}) of the meteorological data.

2. This revised ETOPO5 is re-sampled at 10′ x 10′, the resolution deemed sufficient for further purposes. To retrieve P and T_v for each of these surface points, the 1° x 1° meteorological grid is then refined towards 10′ x 10′ by bilinear interpolation on all pressure levels for the parameters T_v and H. P stays the same for each pressure level.

- For each surface point in the 10′ x 10′ reference pressure data, the two enclosing pressure levels have to be identified (see right sketch in Fig.4.3). Then the virtual temperature is interpolated linearly and the pressure P is obtained by applying the exponential function Eq.4.2:

$$P_s = P_i \, e^{\,(-c\,\Delta H)}, \qquad \text{where} \qquad \Delta H = H_s - H_i\,, \tag{4.2}$$

and the coefficient c

$$c = \frac{\ln(P_i) - \ln(P_{i+1})}{H_{i+1} - H_i}\,. \tag{4.3}$$

The subscript s stands for 'surface', the subscript i denotes the index for the level above 'surface' s and the subscript $i+1$ denotes the index for the level below s.

The interpolation scheme given above was applied for each of the 12 months in the ERA-40 data, covering the time span 1957 to 2001, producing 12 sets of surface pressure P_s and surface virtual temperature T_{vs}. These 12 sets were subsequently averaged to get a single data set of P_s and T_{vs} at 10′ -nodes with corresponding orthometric height H_s. From that fields of block mean values with various spatial resolution were determined (0.5°, 1°, 1°, 2°, 2.5°), see Fig. 4.3, left sketch. The fields can be downloaded at `http://ggosatm.hg.tuwien.ac.at/LOADING/REFPRES/`, 3.9 shows the 1°, 1° grid.

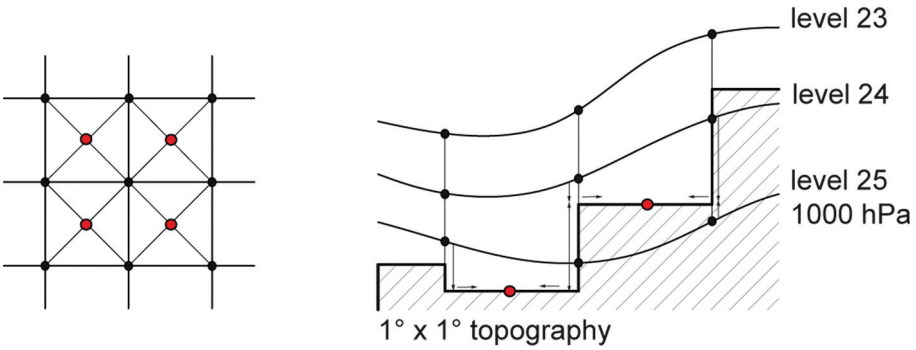

Figure 4.3: On the left the calculation of block mean values at each level, on the right the inter- and extrapolation scheme to the topography and calculation of the corresponding block mean values.

An almost identical procedure as for GRP was applied to the operational analysis data from ECMWF used for this study. These datasets are downloaded as daily rectangular, three-dimensional 1° x 1° grids in the grib-format, containing the geopotential Z, the specific humidity Q, and the temperature T at discrete points on 29 pressure levels and at 4 epochs (00, 06, 12, 18 UTC). Further meta-data like time and date, spatial resolution and number of nodes are included.

Unfortunately GRP is not suitable for the VI approach (see Chap. 4.3.2) as a degree dependent 3D field is needed. For this application we use a mean field calculated from 2 years of analysis data (2008 and 2009, processed as noted above) which shows some differences with respect to GRP, as it can be seen in Fig. 4.4. The impact of this different definition on the de-aliasing product will be discussed in Chap. 4.4.2.

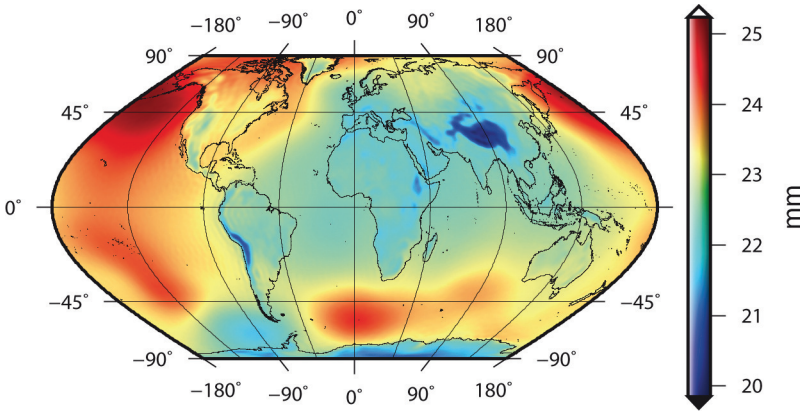

Figure 4.4: Difference of GRP and the mean field used for VI expressed in geoid height, in mm.

4.3 From atmosphere to gravity

The atmosphere is nearly in hydrostatic equilibrium, which means that the change in atmospheric pressure on the surface is proportional to the change of mass in the corresponding atmospheric column, including variations in water vapor mass as well as in the dry air mass. ρ describes the density along the column which can be expressed in terms of surface load σ (Boy et al, 2001; Flechtner, 2007) and which is linked directly to the surface pressure variation Δp.

$$\Delta p = g_0 \int_0^\infty \Delta\rho \mathrm{dr} = \mathrm{g_0}\Delta\sigma\,, \tag{4.4}$$

$$\Delta\sigma = \frac{\Delta p}{g_0}\,, \tag{4.5}$$

where g_0 is the mean gravity acceleration at the Earth surface.

The atmosphere affects the Earth gravity field in two different ways: a direct attraction of the atmospheric masses acting on the orbiting satellite and a much smaller indirect effect introduced by the deformation of the Earth's surface due to elastic loading. The following sections deal exclusively with the direct effect, the indirect effect will be addressed in Sec. 4.3.3.

Due to mass redistribution in the atmosphere the potential V changes with time. This

time-dependency of atmospheric density $\Delta\rho$ can be represented in terms of time-dependent ΔC_{nm} and ΔS_{nm} gravitational coefficients, taking into account Eqs. (4.4) and (4.5), as follows

$$\begin{Bmatrix} \Delta C_{nm} \\ \Delta S_{nm} \end{Bmatrix} = \frac{1}{(2n+1)Ma^n} \iint\limits_{Earth} \Big[\int\limits_{r_s}^{\infty} \Delta\rho r^{n+2} \mathrm{dr} \Big] \overline{\mathrm{P}}_{\mathrm{nm}}(\cos\theta) \begin{Bmatrix} \cos m\lambda \\ \sin m\lambda \end{Bmatrix} \sin\theta \mathrm{d}\theta \mathrm{d}\lambda \,, \qquad (4.6)$$

where r_s is the surface radius and M the mass of the Earth, a the radius of the spherical Earth, P_{nm} are the normalized Legendre polynomials, n and m stand for the degree and order of the spherical harmonic expansion.

4.3.1 Thin layer approximation

In the simplest approach for calculating AGC the vertical extent of the atmosphere is neglected and all the atmospheric masses are concentrated in a thin layer (TL) at the Earth surface. This can be done under the assumption that most of the mass changes occur in the lower 10 km of the atmosphere and act as variable loading effects on the solid Earth's surface (Boy and Chao, 2005).

Surface loads are defined as mass per surface element; therefore the density change in the atmosphere can be expressed in terms of surface load,

$$\begin{Bmatrix} \Delta C_{nm} \\ \Delta S_{nm} \end{Bmatrix} = \frac{a^2}{(2n+1)M} \iint\limits_{Earth} \Delta\sigma \overline{P}_{nm}(\cos\theta) \begin{Bmatrix} \cos m\lambda \\ \sin m\lambda \end{Bmatrix} \mathrm{dS} \,, \qquad (4.7)$$

considering that the mass element $\mathrm{dM} = \rho \mathrm{r}^2 \mathrm{dr} \sin\theta \mathrm{d}\theta \mathrm{d}\lambda = \mathrm{r}^2 \sigma \sin\theta \mathrm{d}\theta \mathrm{d}\lambda = \mathrm{r}^2 \sigma \mathrm{dS}$.

Following the definition of the surface load $\Delta\sigma$ in Eq. (4.5), the surface pressure p_s can be introduced, whereas a mean pressure field $\overline{p}_s$, representing a static mean state of the atmosphere, has to be subtracted to obtain the mass variation:

$$\begin{Bmatrix} \Delta C_{nm} \\ \Delta S_{nm} \end{Bmatrix} = \frac{a^2}{(2n+1)Mg_0} \iint\limits_{Earth} (p_s - \overline{p}_s) P_{nm}(\cos\theta) \begin{Bmatrix} \cos m\lambda \\ \sin m\lambda \end{Bmatrix} \mathrm{dS} \,. \qquad (4.8)$$

Due to our processing strategy we have access to the actual surface radius r_s and the gravity acceleration g at the surface which are used instead of the constant values a and g_0.

As an example the first epoch (00 UTC) of 1 January 2008 is selected. Figure 4.5(a) on the

left depicts the pressure variation at the surface and on the right (Fig. 4.5(b)) the corresponding change in geoid height following the thin layer approach is shown.

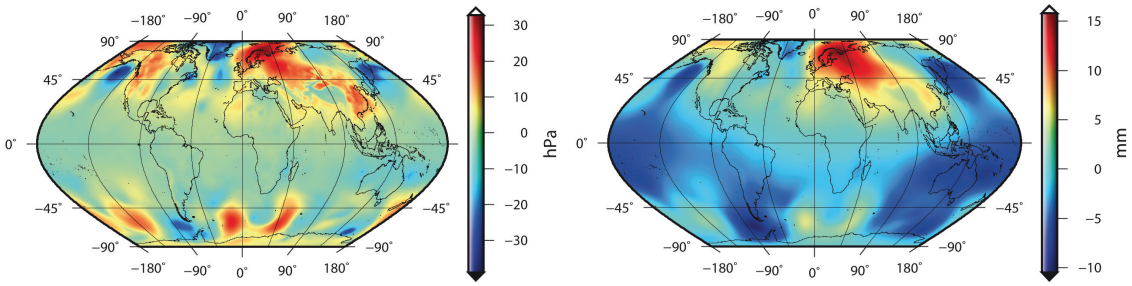

(a) (b)

Figure 4.5: **a)** Pressure variation (actual-mean) in hPa at 1 January 2008, 00 UTC **b)** Resulting geoid height variation following the thin layer approach in millimeter

4.3.2 3D Atmosphere

As mentioned in the introduction of this section, also the change of the center of mass of the atmospheric column has an impact on the orbiting satellite, not only the mass change itself. This variation of the center of mass is not addressed in the thin layer approximation but has to be taken into account for modern satellite gravity missions such as GRACE (Flechtner, 2007; Swenson and Wahr, 2002; Velicogna et al, 2001). This deficiency can be overcome by considering the whole vertical structure of the atmosphere by performing a vertical integration (VI) of the atmospheric masses. To do so, Numerical Weather Models which describe the vertical structure by introducing various numbers of pressure or model levels are needed. In order to formulate the vertical integration we start from the basic Eqs. (2.25) and (2.29), introducing the volume element used in Eq. (4.7); for details see (Flechtner, 2007; Zenner et al, 2010, 2011).

$$\left\{\begin{matrix} C_{nm} \\ S_{nm} \end{matrix}\right\} = -\frac{1}{(2n+1)Ma^n} \iint\limits_{Earth} \left[\int\limits_{r}^{\infty} r^{n+2}\rho \mathrm{d}r\right] \overline{\mathrm{P}}_{\mathrm{nm}}(\cos\theta) \left\{\begin{matrix} \cos m\lambda \\ \sin m\lambda \end{matrix}\right\} \sin\theta \mathrm{d}\theta \mathrm{d}\lambda \,, \qquad (4.9)$$

Adopting the hydrostatic equation 3.3, where g_r is the gravity acceleration at each level, we

get:

$$\begin{Bmatrix} C_{nm} \\ S_{nm} \end{Bmatrix} = -\frac{1}{(2n+1)Ma^n} \iint\limits_{Earth} \Big[\int\limits_{p_s}^{0} \frac{r^{n+2}}{g_r} \mathrm{dp} \Big] \overline{\mathrm{P}}_{\mathrm{nm}}(\cos\theta) \begin{Bmatrix} \cos m\lambda \\ \sin m\lambda \end{Bmatrix} \sin\theta \mathrm{d}\theta \mathrm{d}\lambda \,. \tag{4.10}$$

Again, to analyze gravity field variations caused by atmospheric effects, a quantity $\overline{p}_{VI}$ representing the mean state of the atmosphere, has to be subtracted from the inner integral, leading to:

$$\begin{Bmatrix} \Delta C_{nm} \\ \Delta S_{nm} \end{Bmatrix} = -\frac{1}{(2n+1)Ma^{n+2}g_0} \iint\limits_{Earth} \Big(\Big[\int\limits_{p_s}^{0} r^{n+4} \mathrm{dp} \Big] - \overline{\mathrm{p}}_{\mathrm{VI}} \Big) \overline{\mathrm{P}}_{\mathrm{nm}}(\cos\theta) \begin{Bmatrix} \cos m\lambda \\ \sin m\lambda \end{Bmatrix} \sin\theta \mathrm{d}\theta \mathrm{d}\lambda \,. \tag{4.11}$$

Again the constant values a and g_0 are exchanged with the actual surface radius r_s and the gravity acceleration g at the surface.

4.3.3 Indirect effect

The indirect effect of the atmosphere on the gravity field, can be included quite easily following the approach introduced in Chap. 3.3.3 tracing back to (Farrell, 1972), using the load Love numbers representing the deformational behavior based on the rheology of the Earth,

$$\Delta V_n^{tot} = \Delta V + k_n \Delta V = (1+k_n)\Delta V \,, \tag{4.12}$$

leading to

$$\begin{Bmatrix} \Delta C_{nm} \\ \Delta S_{nm} \end{Bmatrix} = -\frac{1+k_n}{(2n+1)Ma^{n+2}g_0} \iint\limits_{Earth} \Big(\Big[\int\limits_{p_s}^{0} r^{n+4} \mathrm{dp} \Big] - \overline{\mathrm{p}}_{\mathrm{VI}} \Big) \overline{\mathrm{P}}_{\mathrm{nm}}(\cos\theta) \begin{Bmatrix} \cos m\lambda \\ \sin m\lambda \end{Bmatrix} \sin\theta \mathrm{d}\theta \mathrm{d}\lambda \,. \tag{4.13}$$

4.4 Validation and interpretation

Unfortunately the impact of the aliasing effects and other mis-modeling of the atmosphere cannot be estimated straight forward as the true state of the atmosphere and therefore it's impact on gravity measurements is unknown. Thus we have to rely on comparisons, either

using different parameterizations or background models or other de-aliasing products. In the following we will use degree standard deviations in terms of geoid height to compare the performance of various realizations to the GRACE RL04 performance and the one predicted from pre-launch simulations (Kim, 2000). Release 05, available since mid 2012 is considered to be a factor 2-3 better than RL04 in terms of noise reduction (i.e. less pronounced typical GRACE striping artefacts) and spatial resolution, although the changes in the de-aliasing product concern mostly the ocean component and contribute to the improvements about 10% (personal communication Frank Flechtner, 12.03.2013). Further global plots in terms of geoid height will be used to display differences between the AGC realizations for specific epochs. At most times I used January 1, 2008, 00 UTC.

4.4.1 Impact of constant gravity and mean radius a

As is can be seen in the Eq. 4.8 and Eq. 4.11 a constant gravity $g_0 = 9.80665$ m s^{-2} and a mean Earth radius $a = 6371$ km are entered in the expression before the integral. The more accurate way is to replace those constants with the actual surface radius r_s of the Earth surface and a latitude dependent gravity acceleration g which are obtained in the pre-processing. The differences corresponding differences are shown in Fig. 4.6(a) and 4.6(b). Due to the prominent north-south gradient introduced by the Earth flattening (in case of Fig. 4.6(a) the values range between -14.2 km and +10.58 km) the detection of the smaller topographical signals is difficult. Hence this gradient was removed. Same holds for Fig. 4.6(b) in case of the gravity acceleration.

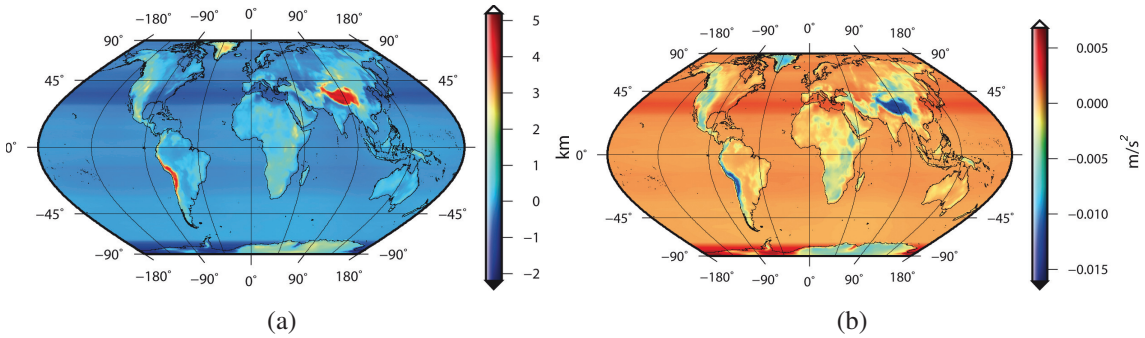

Figure 4.6: **a)**Difference between the geocentric radius to the Earth surface and the radius a = 6371 km of the mean sphere. Latitude dependent gradient removed. **b)** Difference between the gravity acceleration at Earth surface according to EGM96 and the mean gravity acceleration g_0 = 9.80665 m s^{-2}. Latitude dependent gradient removed.

The impact in the resulting de-aliasing product between the variant with constant radius and gravity acceleration and the one with longitude and latitude dependent values for the epoch January 1, 2008, 00 UTC is shown in Fig. 4.7(a). Here signals originating from the atmosphere itself and not from the definition of the radii and gravity acceleration are visible, suggesting that this effect, although the radii differ up to 14 km, is to small to propagate into the final result. As a result, the spread of the difference is only within -95 to 6 μm, thus below the GRACE sensitivity.

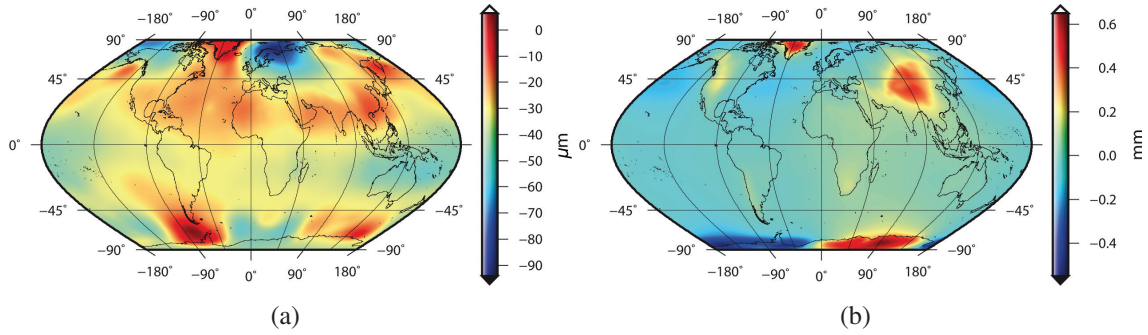

(a) (b)

Figure 4.7: **a)** Differences of the geoid height variation between the thin layer approach with latitude and longitude dependent radii and gravity acceleration and with constant radius a and g_0 for the epochs January 1, 2008, 00 UTC. **b)** Differences of the total atmosphere in terms of geoid height between the thin layer approach with latitude and longitude dependent radii and gravity acceleration and with constant radius a and gravity acceleration g_0 for the epoch January 1, 2008, 00 UTC. Latitude dependent gradient extracted.

To make sure no side effects are introduced by the definition of GRP (see Chap. 3.2.3) I look at the total atmosphere and not at the variation (actual-mean); further the prominent north south gradient introduced by the oblateness of the Earth is removed, otherwise none of the features would be visible. The result is shown in Fig. 4.7(b), where the variation of the remaining signal ranges between -0.55 mm to +0.65 mm (before the removal of the gradient: -0.23 mm - +9.12 mm). The similarities to the Fig. 4.6(a) and 4.6(b) are evident, although the effects introduced by changing the constants into varying parameters are obviously too small to show up in the final result 4.7(a) as the effect is mostly canceled by calculating the difference between mean and actual state of the atmosphere.

Looking at the degree standard deviation of the solution using constants with respect to the one using above variable parameters (Fig. 4.8), the resulting difference is even below the theoretical error level predicted for GRACE (dashed line). The black line marks the RL04 error level. We can conclude that the effects of the approximation of the Earth as a sphere

are too small to play a role in today's GRACE processing. Still this factor may be kept in mind for the future. For the VI approach a similar behavior was confirmed.

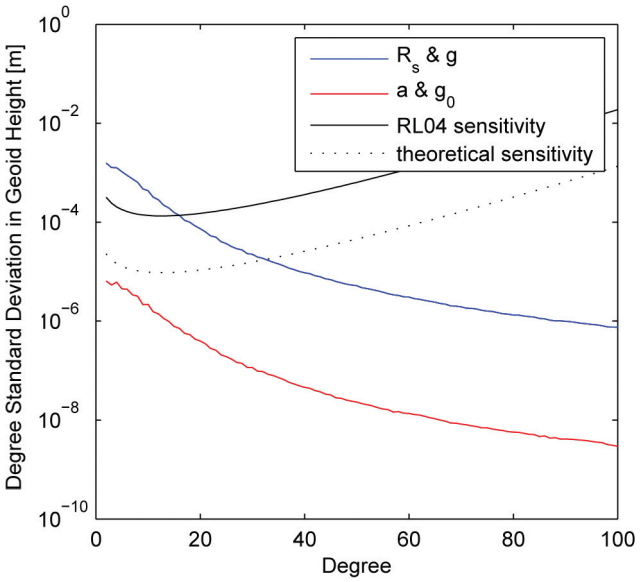

Figure 4.8: Degree standard deviation in terms of geoid height for the year 2008 in meter derived from the thin layer approach, in blue with latitude and longitude dependent radii and gravity acceleration and in red the difference to the solution with constant radius a and constant gravity acceleration g_0. The black line marks the RL04 error level of GRACE, the dashed one the theoretical error as obtained by pre-launch simulations.

4.4.2 Thin layer versus vertical integration and the effects of the mean field

To evaluate the significance of the vertical structure of the atmospheric column, the spherical harmonic series resulting from the TL approach and the ones of the VI are compared. In Fig. 4.9 the degree standard deviation of the coefficients of January 2008 up to degree 100 are plotted, in blue the vertical integration approach, in red the corresponding difference to the thin layer approach. The results indicate that at the RL04 error level (black solid line) the differences between the two approaches are negligible. But if GRACE reaches the targeted error level (dashed line), then the VI approach should be chosen.

When looking at specific epochs, here January 1, 2008 at 00 UTC (Fig.4.10(a)), the differences become more accentuated than when looking at monthly solutions. Further,

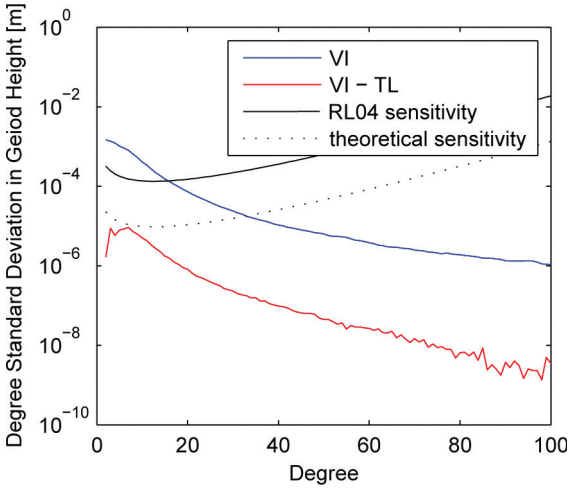

Figure 4.9: Degree standard deviation in terms of geoid height for the year 2008 in meter, in blue for the VI approach, in red the corresponding difference between VI and TL. The black line marks the RL04 error level of GRACE, the dashed one the theoretical error as obtained by pre-launch simulations.

when comparing this plot to the one of the difference between GRP and the mean field used for the VI approach (Fig. 4.4) the similarities in the large scale features catch the eye, suggesting an origin in the mean field definition. This can be confirmed when looking at Fig. 4.10(b), where the mean fields are not subtracted. Here besides the topographical signals and the expected bias, no large scale features like the ones seen in Fig. 4.4 are visible.

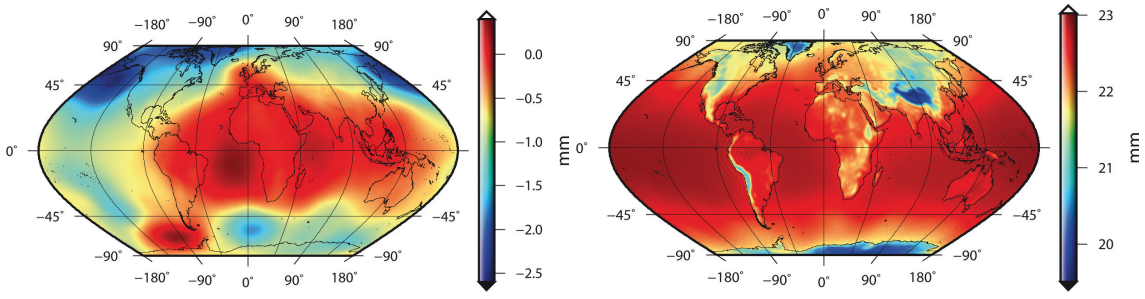

(a) (b)

Figure 4.10: **a)** Difference between VI and TL and **b)** the total atmosphere calculated using VI and TL for January 1, 2008 00 UTC expressed in geoid height in mm.

As an additional test, a surface pressure mean filed consistent with the VI mean field was calculated using the pressure information from the years 2008 and 2009. When calculating the difference of this new mean field and GRP in Fig. 4.11(a) and the VI mean field Fig.

4.11(b) similar features as in Fig. 4.10(a) and 4.4 emerge (minus the VI introduced bias), affirming the effect of the mean field definition on the AGC.

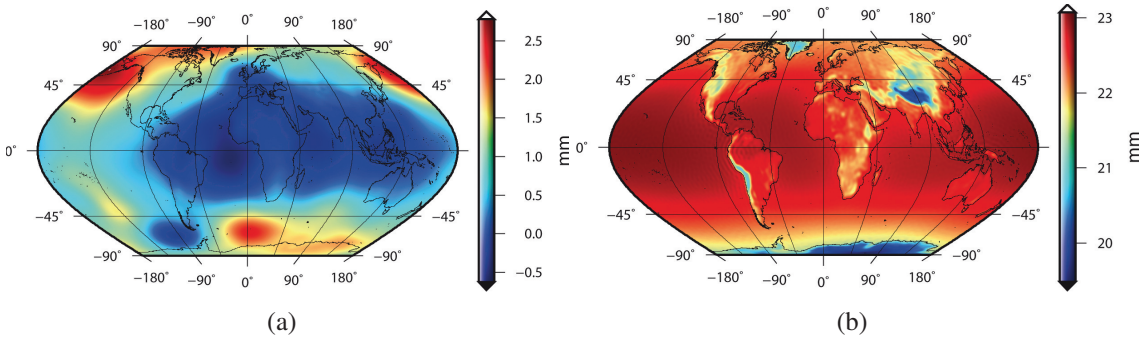

Figure 4.11: **a)** Difference between the surface pressure mean field of 2008 and 2009 and GRP and **b)** the surface pressure mean field of 2008 and 2009 and the VI mean field, expressed in geoid height in mm.

Using the consistent mean fields for the VI and TL comparisons, the differences seen in Fig. 4.10(a) diminish significantly, see. Fig 4.12. Nevertheless calculating the difference in terms of degree standard deviation for both approaches the picture does not change on a significant level compared to 4.9. This leads to the conclusion that the shorter the time resolution of the solution the larger the effect of the mean field, but in general the applied approach has at the current error level no significant impact.

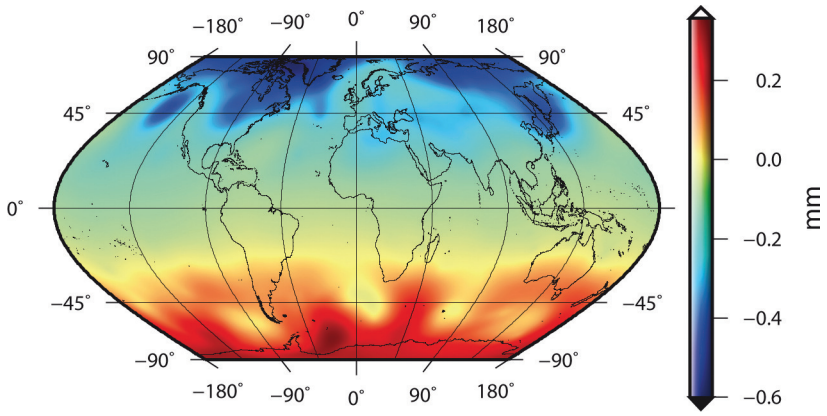

Figure 4.12: Difference between VI and TL using surface pressure mean field of 2008 and 2009 for January 1, 2008 00 UTC expressed in geoid height in mm.

Fig. 4.13 shows exemplarily the geoid height variability for the C_{20} coefficient for 2008, in black for the vertical integration in blue for the thin layer approach, in red the difference.

From this figure the conclusions from above can be confirmed, as the difference between the C_{20} coefficients of both approaches lies always within $\pm$ 0.05 mm. For higher degree and order the differences decrease rapidly.

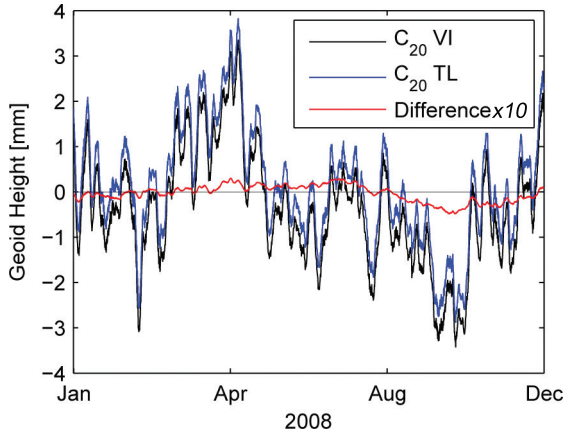

Figure 4.13: Time variation of the C_{20} coefficient in geoid height for the year 2008 in millimeter, in black following the VI approach in blue the TL approach, in red the difference multiplied by 10, bias removed.

4.4.3 Impact of atmospheric loading and atmospheric tides

Comparing the degree standard deviation of the TL approach including the loading effect and the solution without loading (Fig. 4.14) the importance of considering the indirect effect becomes evident. The differences up to degree 4 lie above the RL04 error level and up to degree 15 above the predicted error level, confirming the findings by Flechtner (2007), who recommends to incorporate a correction as they are implemented in the official GRACE AOD1B product. The same conclusion is drawn looking at the difference between introducing and neglecting loading in terms of geoid height variability for low degree coefficients (Fig. 4.15), considering the aimed precision of GRACE to be a few micrometers for degree 3 to 5 (Tapley et al, 2004).

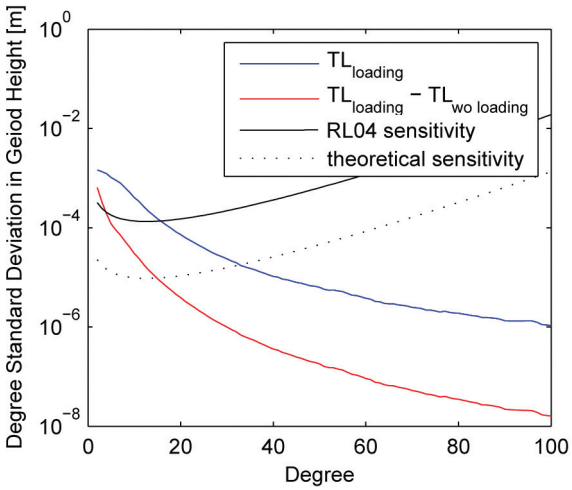

Figure 4.14: Degree standard deviation in terms of geoid height in meter for the year 2008, in blue for the TL approach with loading, in red the corresponding difference of VI without loading. The black line marks the RL04 error level of GRACE, the dashed one the theoretical error as obtained by pre-launch simulations.

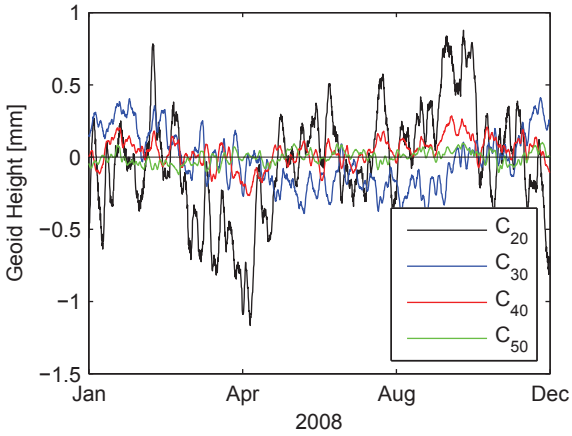

Figure 4.15: Time variations of low degree coefficients expressed in geoid height in millimeter, difference between neglecting and including loading, in black C_{20}, in blue C_{30}, in red C_{40} and in green C_{50}.

When looking at the impact of atmospheric tides, a similar impact on the atmospheric de-aliasing product can be detected (see also Chap. 3.3.2). Figure 4.16 shows the degree standard deviation of the S1, S2 and S3 tides at 00UTC for January 1st 2008 in terms of geoid height in comparison to the error level of GRACE and the corresponding TL solution in- and excluding tidal corrections. It shows that this correction can help significantly to improve the low degree coefficients, so that they can meet the RL04 error level and improve the per-

formance for all degrees of about half an order of magnitude, especially when aiming for sub-monthly solutions (as on a monthly basis some of the effects get averaged out).

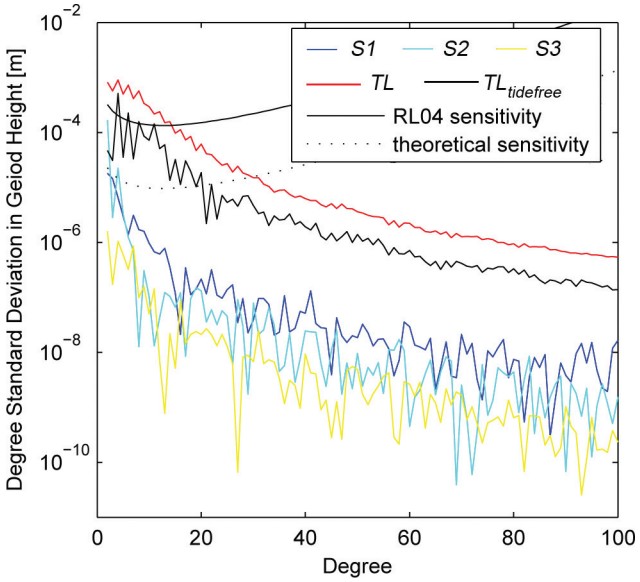

Figure 4.16: Gravity variation signals of the S1 (blue), S2 (cyan) and S3 (yellow) tides in terms of degree standard deviation for January 1st 2008. The black line marks the RL04 error level of GRACE, the dashed the theoretical error as obtained by pre-launch simulations. The red line is the degree standard deviation for the TL approach without tidal correction, the black line with tidal correction.

4.4.4 Comparison of different NWM

As mentioned in Chap. 3.2.1, the model data at ECMWF is available as pressure (PL) or model level (ML) data. The largest difference between those two becomes evident in the method of discretization of the vertical structure of the atmosphere. For the model level data 91 levels are introduced which reflect the density structure of the atmosphere, i.e. near the surface the levels are closer together than in high altitudes where less mass is present. Within the pressure level data the vertical discretization is implemented through 25 levels following surfaces of equal pressure from 1000 hPa to 1 hPa. Whereas the model level data reaches up to approximately 80 km, the pressure level covers around 46 km. The lowest model level, i.e. the one nearest to the surface follows the orography used by ECMWF. The lowest pressure level on the other hand, follows strictly the 1000 hPa isobar, ignoring the topography, so that it can also lay underneath it, as it is the case for mountainous areas such as Austria. In Fig. 4.17(a) and 4.17(b) the progression of the pressure and the gravity acceleration above Vienna

(48° N, 16° E) for January 1 2008, 00 UTC are plotted, in red for the model level data, in blue for the pressure level. Although in both cases the path is almost exactly the same, the difference in the height becomes evident.

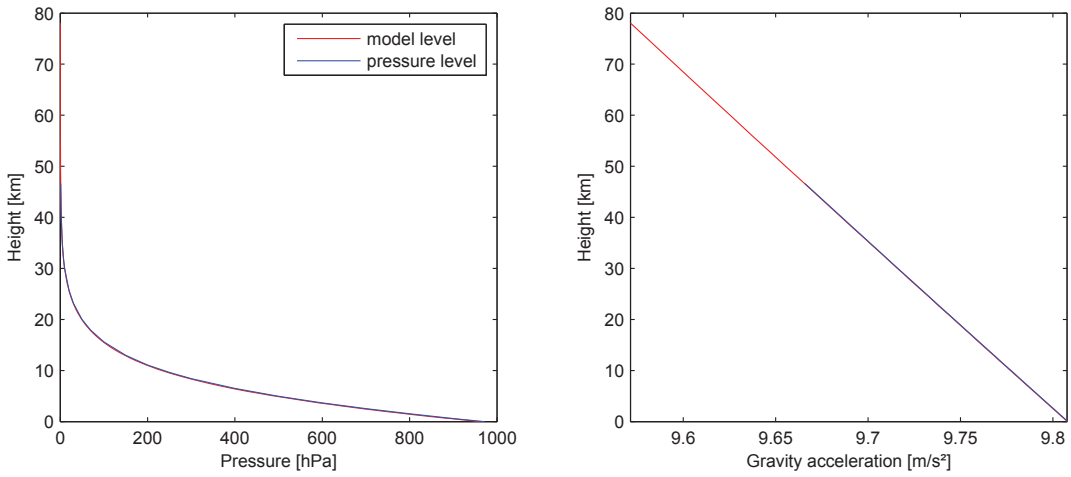

(a) (b)

Figure 4.17: Progress of **a)** pressure and **b)** gravity acceleration above Vienna (48 N, 16E) for January 1st 2008, 00 UTC; in red model level data, in blue pressure level data for January 1, 2008, 00 UTC.

To determine the influence of the data structure on the AGC results, the difference between the solutions computed with PL and ML data is calculated and plotted in Fig. 4.18 in terms of geoid height. To make sure nothing is canceled by averaging out or additional signals are introduced my the mean pressure field, the total atmosphere of the specific epoch is used instead of the difference of actual-mean. Small features over the continents appear, suggesting a topographic influence. When comparing it to Fig. 3.7, where the difference between ECMWF orography and ETOPO5 topography is plotted, this assumption can be confirmed, as similar features are showing up. It shall be mentioned, that ECMWF does not apply the same orography to model and pressure level data. When calculating the variation (actual - mean) the remaining signal has a maximum amplitude of 0.4 mm.

When taking into account only the levels above the 46 km line, i.e. all the masses which are included in the ML data only, one can find a very small signal with an RMS of 7.4 μm including small topographic signals,compared to the ACG calculated by subtracting a mean pressure field, where this signal almost vanishes completely. Hence it can be concluded, that the dominating factor causing the differences between the two datasets is the underlying

topography /orography, the masses above 46 km are to small to have an impact on the geoid.

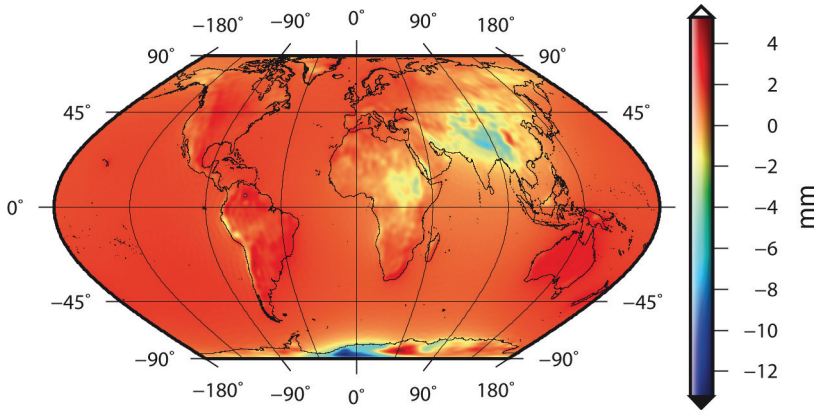

Figure 4.18: Differences of the total atmosphere in geoid height between the solutions with pressure level and model level for January 1st 2008, 00 UTC.

Looking at the degree standard deviation of the coefficients calculated for January 2008 (see Fig. 4.19), it becomes clear that the influence of the model structure is far too small to play a role in the current GRACE processing.

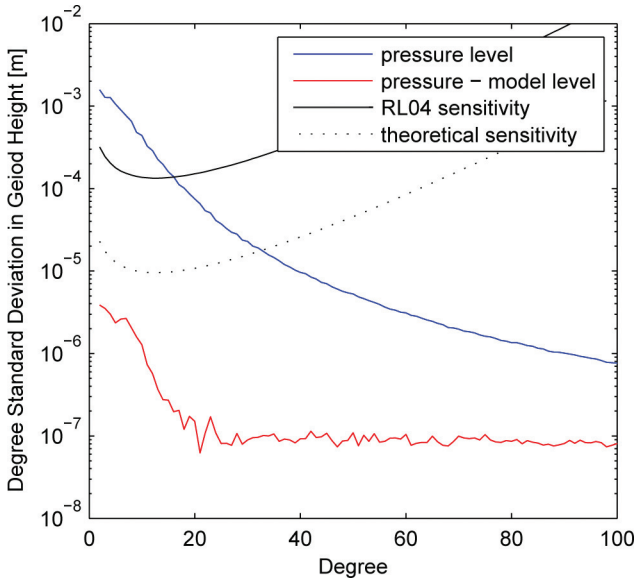

Figure 4.19: Degree standard deviation in terms of geoid height for January 2008, in blue for pressure level data, in red the corresponding difference between pressure level and model level data. The black line marks the RL04 error level of GRACE, the dashed on the theoretical error as obtained by pre-launch simulations.

As mentioned in 3.2.1 the assimilation methods as well as the background models of NWM evolve continuously. This fact can result in problems, especially if the orography

is subject to such changes, too. The reason is the direct link between orography and barotropic pressure, meaning that a change in the orography changes also the pressure of the model levels. This can lead to jumps in the pressure of several hPa as it happened in 1.2.2006 and 26.1.2010 when ECMWF updated the operational analysis (L. Zenner, TU Munich, personal communication 26.09.2012; Elisa Fagiolini, GFZ Potsdam, personal communication 27.11.2012, for details see `http://www-app2.gfz-potsdam.de/pb1/op/grace/aod_issues/issues_aod1b_rl05.html` and `http://www.ecmwf.int/products/data/operational_system/evolution/evolution_2006.html`). While such jumps do not happen on a global scale, but mainly in regions with rapid height changes and also there on very scattered areas, this still adds a further error source to the de-aliasing process. Figure 4.20 shows the surface pressure variation starting from 01.01.2006 00 UTC until 31.03.2010 18 UTC for a point in the Andes (lat:112; lon:291).

This is the main reason why we decided to use pressure level data and to introduce ETOPO5 as our topography. Although the pressure level data is derived from model level data, pressure levels are not connected directly to the orography used by model level, and by reducing the data to our own topography we gain even further independence from the ECMWF orography. This procedure has proven its value as no jumps introduced by changes in the ECMWF processing strategy can be seen in our pressure level data.

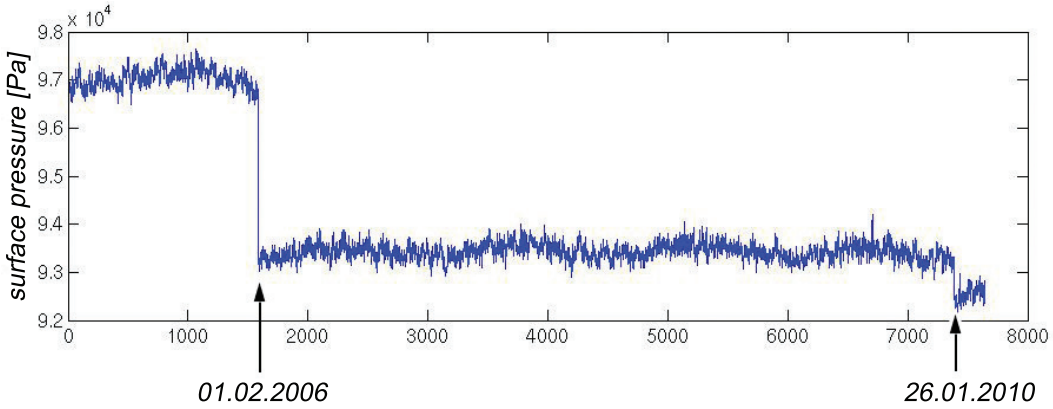

Figure 4.20: Surface pressure variation starting from 01.01.2006 00 UTC until 31.03.2010 18 UTC for a point in the Andes (lat:112; lon:291), courtesy of L. Zenner.

When comparing models provided by different data centers, in this study ECMWF and

NCEP, notable differences, especially at relatively short time scales (Velicogna et al, 2001) and in regions with sparse meteorological data, for example, Antarctica, show up (see. Fig.4.21(b)). NCEP and the National Center for Atmospheric Research (NCAR) have accomplished different re-analysis projects which aim at the generation of global data sets for a long time period for different atmospheric parameters (Kalnay et al, 1996). The re-analysis is created with one model for the whole re-analysis period, similar to the one used for weather forecasts. For this study surface pressure data from the NCEP/NCAR Reanalysis I (1948-present) is used. It has a temporal coverage of 4-times daily, on 2.5° x 2.5° global grids. For the following investigations, the data was interpolated linearly to 1° x 1° grids.

Comparing the orography derived from the geopotential height given in the NCEP/NCAR dataset with the one given by ETOPO5 and introduced into the processing of the ECMWF data, differences up to 2.3 km appear in regions with rapid height changes such as mountains and coast lines (Fig. 4.21(a)). This characteristic is reflected as expected also within the difference between the surface pressures of the two datasets, as it can be seen in Fig. 4.21(b), again January 1, 2008 at 00 UTC is chosen as example. As a mean state of the atmosphere is needed to calculate AGC, for the NCEP/NCAR data a 2 year mean over 2007 and 2008 was calculated. Compared to GRP, it shows a similar result to Fig. 4.21(b) within a margin of ±10 hPa. Further it has to be mentioned that the NCEP/NCAR Reanalysis I is processed on a sphere leading to similar implications discussed in 4.4.1.

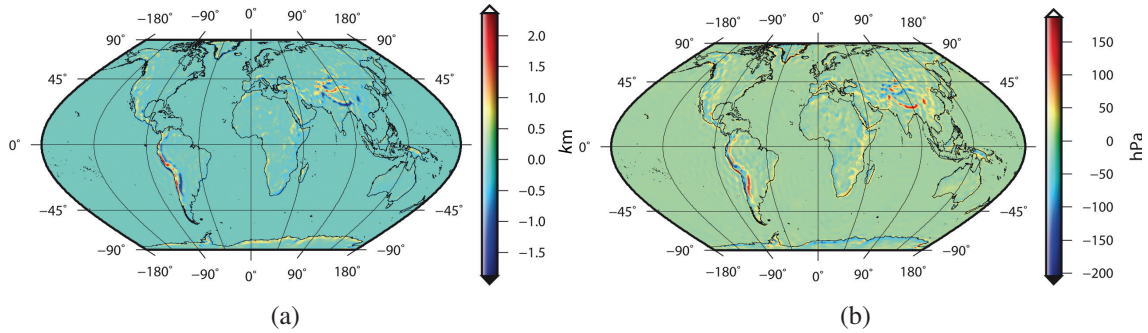

Figure 4.21: **a)** Difference between NCEP/NCAR orography and ETOPO5 topography **b)** Difference between surface pressures taken from NCEP/NCAR and ECMWF on ETOPO5 for January 1st, 00 UTC.

When looking at the pressure variation, i.e. the difference between the actual and the mean

state of the atmosphere, both models show a good agreement within -9.7 and +13.3 hPa for the selected epoch (Fig. 4.22), demonstrating prominent signals of topographical origin in the Himalaya and the Rocky Mountains and smaller signals (±5 hPa). For other epochs the differences lie characteristically between ±15 hPa, demonstrating that the results of the first epoch of January 1st showing a remarkably good agreement between the models. This becomes clearly visible when calculating the ACG and the difference of corresponding geoid height as shown in Fig. 4.23, upper left plot, where the values lie between -1.7 and 2.8 mm.

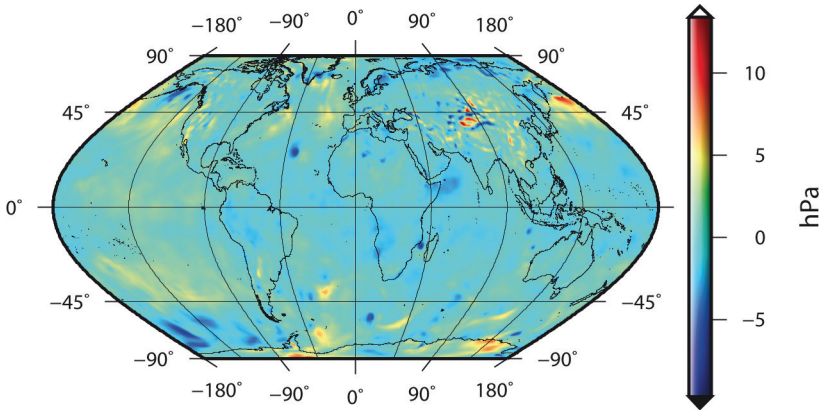

Figure 4.22: Difference between the pressure variation calculated from NCEP/NCAR and ECMWF data in hPa for January 1st, 00 UTC.

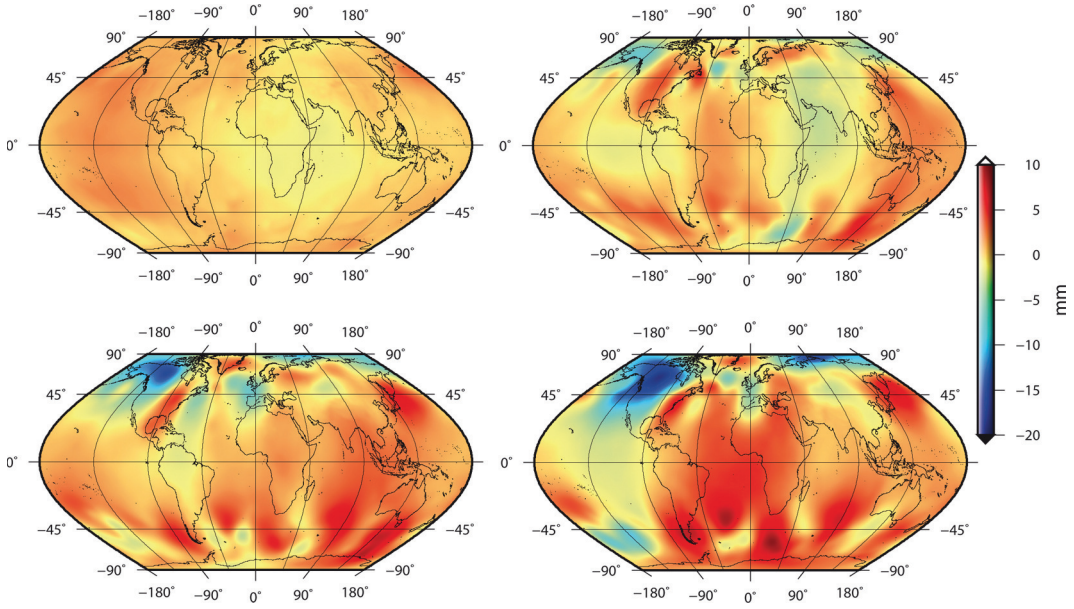

Figure 4.23: Difference between geoid height variation calculated from NCEP/NCAR and ECMWF data using the TL approach in mm for January 1st, 00 (upper left), 06 (upper right), 12 (lower left) and 18 UTC (lower right).

The pattern in the upper left plot of 4.23 depicting the difference at 00 UTC, strongly suggests a tidal wave, but when looking at other epochs shown in 4.23 that assumption can not hold up. Not only show other epochs none such pattern but also the differences are much bigger. As for January 1st, 06 UTC the differences range between -8.09 and 6.19 mm, similar results hold for other epochs and other days, leading to the conclusion, that the small difference (-1.68 to 2.82 mm) for the first epoch of January 1st is coincidental, as is the pattern; or that only when both models agree fairly well the smaller signals of a possible tidal nature become visible.

Finally, looking on the degree standard deviation of the coefficients between the two models calculated for January 2008 in Fig. 4.24(a), it becomes clear that the influence of the model structure is too small to play a role in the current GRACE processing. But again, when aiming at weekly or daily solutions, this difference becomes significant (see Fig. 4.24(b)), confirming the findings considering the NWM data structure looking at different ECMWF products, discussed at the beginning of this section.

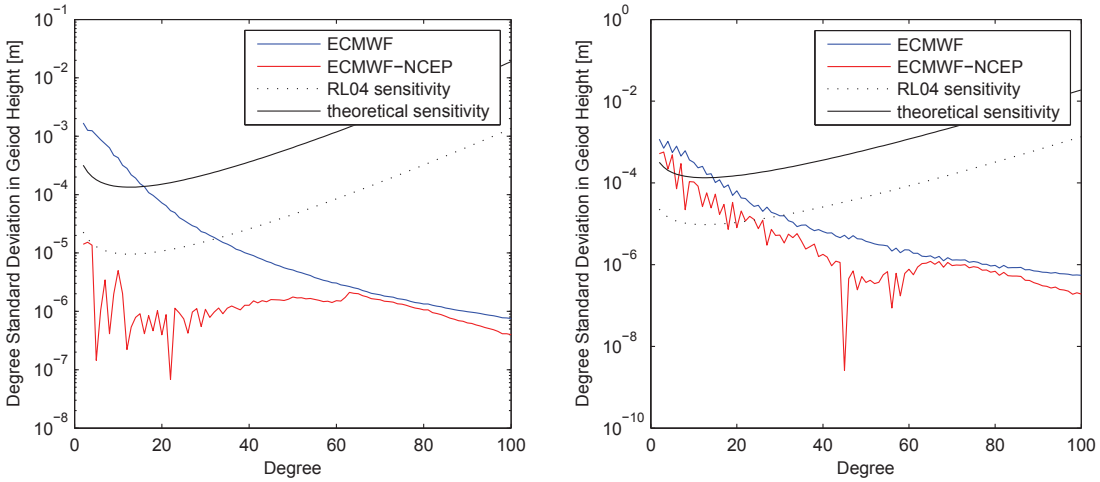

Figure 4.24: Degree standard deviation in terms of geoid height in blue for the ECMWF, in red the difference between ECMWF and NCEP/NCAR for **a)** January 2008 and **b)** the epoch Jnauary 1st, 00 UTC, The black line marks the RL04 error level of GRACE, the dashed on the theoretical error as obtained by pre-launch simulations.

4.4.5 Comparison of different de-aliasing products

Several centers are generating de-aliasing products for GRACE processing. The most widely used is the AOD1B product provided by German Research Centre for Consciences (GFZ) (Flechtner, 2007). It provides 4 datasets: atmosphere (atm), ocean (ocn), ocean bottom pressure (oba) and a global atmosphere and ocean combination (glo). Here only the first (atm) is of interest.

$AOD1B_{atm}$ is based on 6 hourly ECMWF analysis model level data on a gaussian n160 grid which corresponds to 0.5°. The main difference between our approach and the one used for $AOD1B_{atm}$, besides the model level data and it's implied problematics concerning orography and internal model changes, can be found in the calculation of VI. While we abandon the usage of constants like mean radius of the Earth a and mean gravity acceleration g (see Eq. 4.11) in this approach they are used, leading to the same conclusions as shown in Chap. 4.4.1. Further approximations for the mean geoid over the sphere are needed, using the potential height at the Earth surface, i.e. orography, given by ECMWF. A tidal correction for S1 and S2 is applied.

A second center providing de-aliasing products is CNES/GRGS (Centre National d'Etudes Spatiales / Groupe de Recherche de Géodésie Spatiale) (Gegout, 2009). The ECMWF data is based on operational analysis in form of spherical harmonics, truncated at T799 for the time period used here, i.e. January 2008. In contrast to the approach used by GFZ and us, here an up- and downward-continuation is implemented.

For the following comparisons we use AGC calculated with the VI approach and corrected for loading and tides (S1,S2 and S3).

When looking at the degree standard deviation calculated over one month (Fig. 4.25), all solutions show a very good agreement, i.e. the differences for most coefficients lie below the theoretical error line, except for degree 2 for both solutions, and up to degree 8 for $AOD1B_{atm}$. But when looking at singular epochs, e.g. January 1, 2008, 00 UTC (similar behavior confirmed for other epochs), the picture changes significantly.

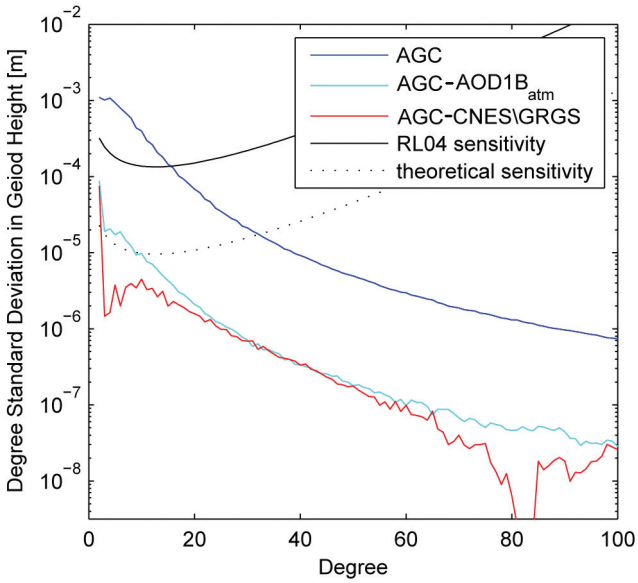

Figure 4.25: Degree standard deviation in terms of geoid height for January 2008, in blue for AGC, in cyan the difference of AGC and AOD1B$_{atm}$ and in red AGC and CNES/GRGS. The black line marks the RL04 error level of GRACE, the dashed one the theoretical error as obtained by pre-launch simulations.

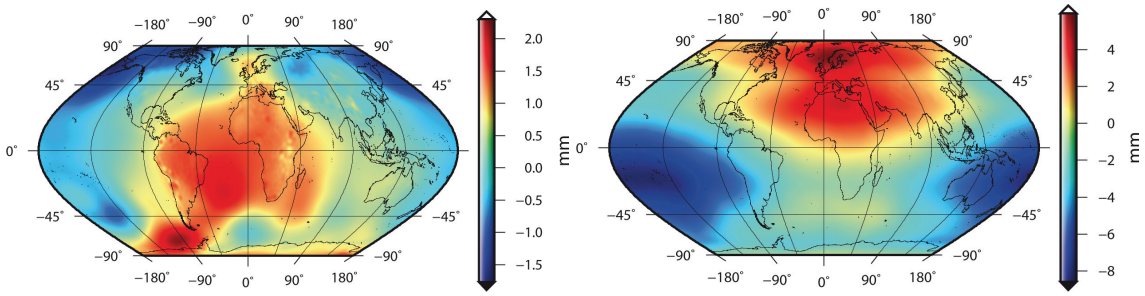

(a) (b)

Figure 4.26: **a)** Difference of AGC and GFZ$_{atm}$ and **b)** AGC and CNES/GSGR for the epoch January 1, 2008, 00 UTC.

Here the differences of both centers differ on a substantial level, as it can be seen in Fig. 4.26(a) for AOD1B$_{atm}$, and in Fig. 4.26(b) for CNES/GRGS. Comparing the difference of AOD1B$_{atm}$ with the difference calculated between GRP and the mean field used for VI (Fig. 4.4), some similarities can be noticed. This leads to the conclusion that the main differences visible here, arise from the different definition of the mean field. Whereas we use a mean over 2008-2009, GFZ calculates its mean field out of 2001 and 2002. But the main contribution can be found in the different processing method of the raw data, see Chap. 4.2. Further

some signals with topographical origin are visible, linking to the different definitions of the orography / topography in both approaches. The differences of AGC to CNES/GRGS are a factor 3-4 larger and of a large scale nature. No topographical signals, which are expected to be much smaller, are therefore visible. The signal shows a similar behavior for all epochs, strongly connected to the n=2, m=1 spherical harmonics, which are associated with the position of the Earth's figure axis. A different definition in AGC and CNES/GRGS concerning this point may be a possible explanation.

Looking at the temporal variation of the C_{20} coefficient in Fig. 4.27, the smoothness of the AGC series (blue) in contrast to the other de-aliasing products sticks out, meaning that in the AGC series the sub daily variations are much smaller. But when comparing the AGC solution without tidal correction (black) to the $\text{AOD1B}_{\text{atm}}$ (cyan) and CNES/GRGS (red), the correlation is much better. The largest contribution to the sub daily variation in the AGC C_{20} is due to the S2 tide, see Fig 4.16, leading to the conclusion, that the applied tidal correction works fairly well.

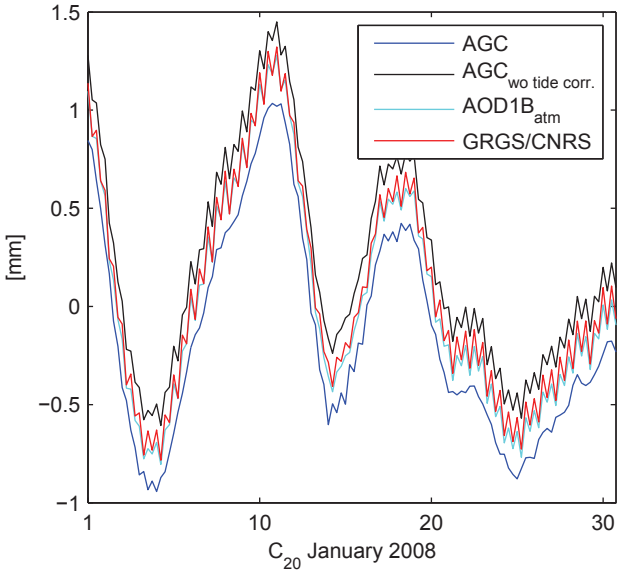

Figure 4.27: C_{20} coefficient for January 2008, in blue AGC, in black AGC without tidal correction, cyan $\text{AOD1B}_{\text{atm}}$ and red CNES/GRGS.

4.4.6 Atmosphere and gradients

As presented in Chap. 2.2.3 GOCE is equipped with a satellite gravity gradiometer (SGG), measuring the gravity gradient (Eq. 2.20 in Chap. 2.1.2) on a global scale. Per design the gradiometer is sensitive to the static gravity field of the Earth and has its highest accuracy at high degree coefficients, whereas the distinct noise characteristics of the gradiometer prohibit the precise determination of lower degree coefficients (Rummel et al, 2011). Previous studies have demonstrated the low sensitivity of GOCE to ocean tides and to temporal gravity field variations at the seasonal scale as well as to long wavelengths of the gravity field, where most of the aliasing signals caused by geophysical mass variations arise from (Jarecki et al, 2005; Han et al, 2006). In this study gravitational gradients of the atmospheric masses are calculated using the AGC at the altitude of the GOCE satellite h=250 km. The resulting gradients are then compared to the specifications of the GOCE gradiometer.

The relation between the GOCE SGG observables, i.e. the gradients, and the time-variable gravity can be expressed through the spherical harmonic functions. For example, the expressions for the diagonal components of the gravity tensor are given by (Petrovskaya and Vershkov, 2006; Kiamehr and Eshagh, 2008):

$$T_{zz} = \frac{GM}{a^3} \sum_{n=2}^{\infty} \sum_{m=0}^{n} (n+1)(n+2) \left(\frac{a}{r}\right)^{n+3} P_{nm}(\sin\phi)(C_{nm}\cos m\lambda + S_{nm}\sin m\lambda)\,, \tag{4.14}$$

$$\begin{aligned} T_{xx} = & \frac{GM}{a^3} \sum_{n=2}^{\infty} \sum_{m=0}^{n} \left(\frac{a}{r}\right)^{n+3} P_{nm}(\sin\phi)(C_{nm}\cos m\lambda + S_{nm}\sin m\lambda) \\ & (a_{nm}P_{nm-2}(sin\phi) + (b_{nm} - (n+1)(n+2))P_{nm}(sin\phi) + (c_{nm}P_{nm+2}(sin\phi))\,, \end{aligned} \tag{4.15}$$

$$\begin{aligned} T_{yy} = & \frac{GM}{a^3} \sum_{n=2}^{\infty} \sum_{m=0}^{n} \left(\frac{a}{r}\right)^{n+3} P_{nm}(\sin\phi)(C_{nm}\cos m\lambda + S_{nm}\sin m\lambda) \\ & (a_{nm}P_{nm-2}(sin\phi) + (b_{nm}P_{nm}(sin\phi)) + (c_{nm}P_{nm+2}(sin\phi))\,, \end{aligned} \tag{4.16}$$

where GM is the gravitational constant times the mass of the Earth, a the mean radius of the Earth, P_{nm} the fully normalized, associated Legendre functions of degree n and order m. r, ϕ and λ are the geocentric distance, latitude and longitude, the coefficients before the Legendre functions a_{nm}, b_{nm}, c_{nm} are numerical constants and can be found in (Petrovskaya and Vershkov, 2006). Similar formulas exist for T_{xy}, T_{xz} and T_{yz} in the given references.

The left picture in (Fig. 4.28(a)) shows the radial gradient component Tzz in Eötvös [$10^{-}9/s^2$] of EGM96 (Earth Gravitational Model 1996) at the Earth surface and the right (Fig. 4.28(b)) T_{zz} at the altitude of GOCE ($r = a + h$).

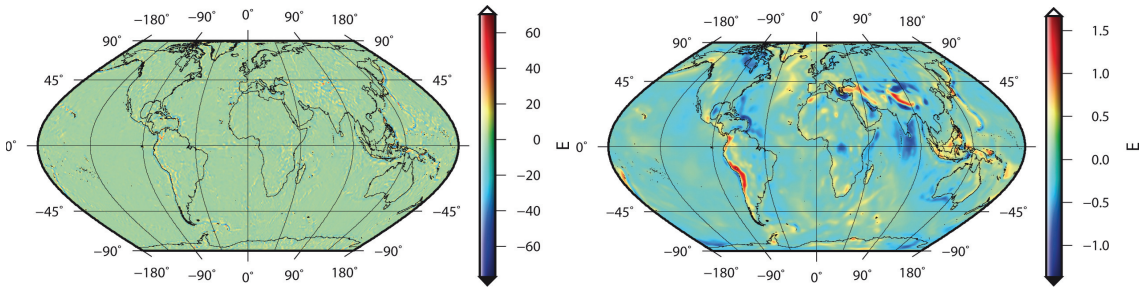

(a) (b)

Figure 4.28: **a)** Gradient component T_{zz} for EGM96 at the surface and **b)** at GOCE altitude in Eötvös.

By introducing the AGC into the Eq. 4.14 - 4.16 the components of the atmospheric Eötvös-tensor can be calculated. Fig. 4.29 shows the resulting global maps of GOCE's highest sensitive components $T_{xx}, T_{yy}, T_{zz}, T_{xz}$ applying the AGC of January 1st, 2008, 00 UTC. Table 4.1 provides the corresponding statistical analysis, all values are given in mE [$10^{-}12/s^2$].

all values in mE	min	max	mean	std
T_{xx}	-0.1324	0.2083	-0.0006	0.0389
T_{yy}	-0.0172	0.0116	-0.0029	0.0037
T_{zz}	-0.2101	0.1377	0.0035	0.0405
T_{xz}	-0.0141	0.0114	0.0001	0.0024

Table 4.1: Statistical analysis of the high sensitive gradient components using the AGC of January 1st, 2008, 00 UTC.

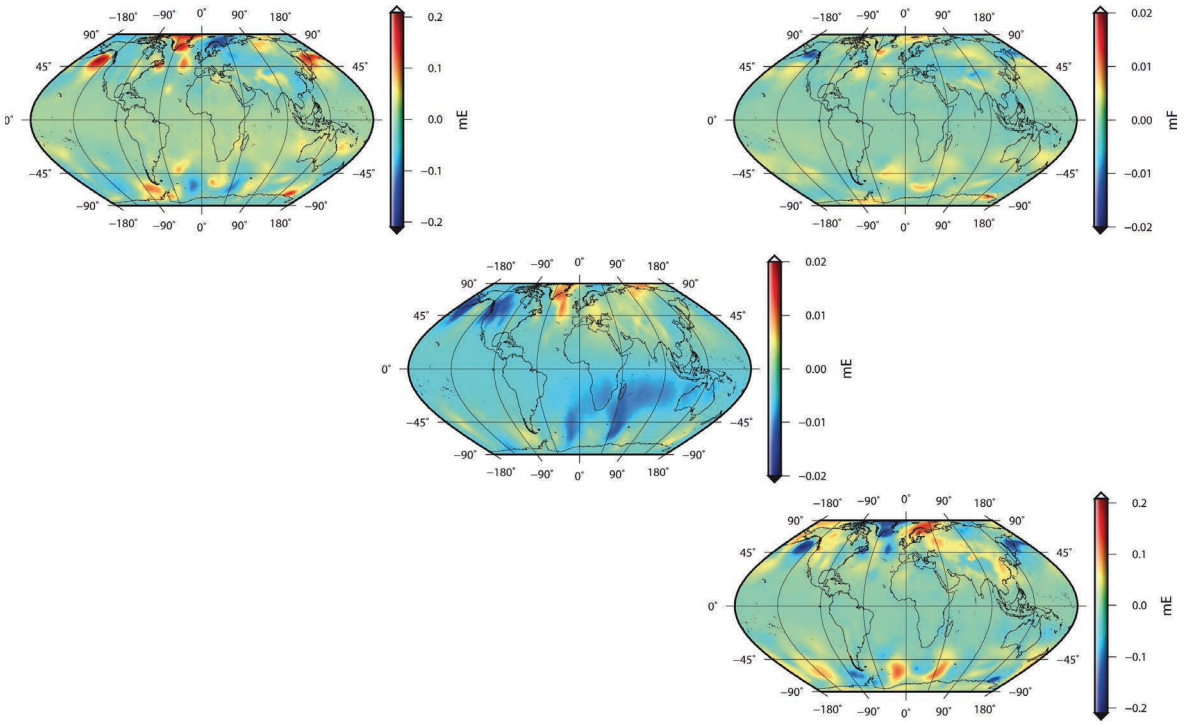

Figure 4.29: $T_{xx}, T_{yy}, T_{zz}, T_{xz}$ using the AGC of January 1st, 2008, 00 UTC.

The values of T_{xx} and T_{zz} range between ± 0.2 mE, the other 3 components are an order of magnitude smaller. Comparing these results with the GOCE specifications (Drinkwater et al, 2003), where it is stated that gravity gradients of the high sensitive components are measured with an accuracy of 3 mE within the measurement bandwidth of 0.5 mHz to 0.1 Hz, it can be concluded that the atmosphere has no significant impact on the GOCE SGG observations, confirming the findings by Abrikosov et al (2006) and Bouman et al (2008). Although is seems unnecessary to apply atmospheric corrections to the SGG data (same holds for other temporal signals like ocean tides) there are also arguments to favor it. The de-aliasing could

improve the stochastic behavior of the observation errors as well as of the gradiometer data itself (Abrikosov et al, 2006). Further on the GOCE SST data needs to be corrected for atmospheric effects, hence to be consistent, this correction should also be applied to the SGG data. In case of the atmospheric correction the same processing strategy as for GRACE is used (Flechtner, 2007), only the static mean field is computed from the years 2004 till 2007, as this time window is closer to the GOCE mission (Bouman et al, 2008). In practice the SGG temporal corrections are given as separate entries in the final gravity gradient product to leave it to the user if this correction shall be applied or not (Gruber and Rummel, 2006). However, using longer time spans of GOCE data (e.g. two 6-month periods), the accuracy of the gravity field is expected to increase, whereas the measurement noise should decrease by several orders, thus making the time varying signals more crucial (Han et al, 2006).

Chapter 5

Atmospheric corrections for superconducting gravimeters

In 1977 the close relation between atmospheric pressure and gravity was demonstrated for the first time by Warburton and Goodkind (1977) and it was demonstrated that the residual noise of superconducting gravimeter measurements are dominated by the atmospheric pressure signal. The mass-redistributions in the atmosphere cause temporal variations of their density and therefore induce changes of the Earth gravity field up to 250 nm s^{-2}. The direct effect, i.e. the attraction of the air masses, is caused mainly by the attraction of the air masses above the instrument within a radius of 50 km (Merriam, 1992). The so-called indirect effect which usually acts reverse to the direct effect and shows a large scale impact and accounts for up to 5% of the total effect (Neumeyer et al, 2004). To correct for these atmospheric effects, various models were established over the past decades. An overview shall be given here.

5.1 Conventional models and new approaches

Over thze last decades various approaches for atmospheric effects have been estabished, each with its own strenght and weaknesses. A short overview on the most commonly used shall be given here.

5.1.1 Admittance models

The use of a single scalar admittance has been well established to correct the gravity signal for atmospheric effects (Warburton and Goodkind, 1977; Torge, 1989; Crossley et al, 1995). The standard regression model assumes that a station recording absolute or relative gravity g [μGal] and pressure p [hPa], can be corrected following the relation

$$g_c(t) = g(t) - \alpha(p(t) - p_0) = g(t) - \alpha\Delta p(t)\,, \tag{5.1}$$

where α is the regression coefficient and p_0 a log-term mean atmosphere pressure, leading to the pressure variation $\Delta p(t)$. Admittance factors obtained from the air pressure records and residuals of tidal analysis usually range between -2 nm s^{-2} and -4 nm s^{-2} per hPa (Spratt, 1982; Rabbel and Zschau, 1985; van Dam and Wahr, 1987; Merriam, 1992), in central Europe usually lies between -3 and -4 nm s^{-2} per hPa.
The corrected gravity residual g_c can be determined by minimizing the differences between the observed gravity residuals g and the observed barometric pressure p in a least square fit and solving for the real coefficient α. Minimizing $|g_c(t)|^2$ assumes that the errors in g and the residuals in g_c are uncorrelated (Crossley et al, 1995).

Following the IAG resolution Nr. 9 (see IGC (1998)) α equals -3 nm s^{-2} per hPa and the long term mean p_0 refers to the standard atmosphere at station height H following DIN 5450:

$$p_0 = 1013.25\left(1 - \frac{0.0065 \cdot H(m)}{288,15}\right)^{5.2559}\,. \tag{5.2}$$

This simple approach is quite effective, it accounts for up to 90% of the total atmospheric effect, and hence is widely used. But especially for monthly and seasonal periods, this method leaves room for improvement, as a measurement of the pressure at the surface reflects the integral effect of mass changes along the vertical atmospheric column only, neglecting the spatial distribution of the masses. Furthermore, the hydrostatic assumption (Eq. 3.3)is not always justified, especially for convective processes or mass transport phenomena (redistribution of air, water vapor, water content); also the passage of a cold front over a gravimeter leads to a more complex behavior (Müller and Zürn, 1983). Additionally the

distinction between the attraction and deformation portion of the total effect is not possible. Thus, the single admittance concept is in many cases insufficient to remove short term air pressure variations and precipitation effects (e.g. Meurers et al (2011)). It was also shown by Warburton and Goodkind (1977) that at near tidal frequencies the single admittance is not reliable.

To make better use of the local pressure several approaches have been suggested, in particular using frequency dependent admittance (Crossley et al, 1995; Kroner and Jentzsch, 1999), showing a good performance at short time scales.
Transforming Eq. (5.1) to the frequency domain we get:

$$G_c(\omega) = g(\omega) - \alpha \Delta p(\omega)\,, \tag{5.3}$$

where α becomes a complex scalar (Crossley et al, 1995). Minimizing $|G_c(\omega)|^2$ over the frequency range $0 < \omega < \omega_n$, where ω_n is the Nyquist frequency, leads to:

$$\alpha^* = \frac{\sum[G^*(\omega)\Delta p(\omega)]}{\sum|\Delta p(\omega)|^2}\,. \tag{5.4}$$

The real and imaginary solutions of Eq. (5.4) are

$$\alpha_R = \frac{\sum[G_R(\omega)\Delta p_R(\omega) + G_I(\omega)\Delta p_I(\omega)]}{\sum|\Delta p(\omega)|^2}\,, \tag{5.5}$$

$$\alpha_I = \frac{\sum[G_I(\omega)\Delta p_R(\omega) - G_R(\omega)\Delta p_I(\omega)]}{\sum|\Delta p(\omega)|^2}\,, \tag{5.6}$$

and can be combined into the admittance amplitude α and the phase ϕ.

Allowing the admittance α to be additionally frequency dependent by modifying Eq. (5.1) to

$$G_c(\omega) = g(\omega) - \alpha(\omega) \Delta p(\omega)\,, \tag{5.7}$$

we get the same solution like in Eqs. (5.5) and (5.6), but now the summation is over an averaging window centered on each individual frequency. The choice of the width of the window is crucial, especially at the ends of the frequency ranges and in vicinity of the

harmonics of the solar tides. Nevertheless no standard can be given, considering the high dependency on the individual time series.

The operations above in the frequency domain have their equivalent in the time domain. Transforming Eq. (5.7) back, we get

$$g_c(t) = g(t) - \alpha(t)\Delta p(t)\,, \tag{5.8}$$

and for the admittance $\alpha(t)$ the coefficients h_n at the data sampling interval:

$$\alpha(t) = [\ldots h_{-1}, h_0, h_1 \ldots]\,. \tag{5.9}$$

The Fourier Transformation of Eq. (5.9) for a simple three term filter $\alpha(t) = (h_{-1}, h_0, h_1)$ yields:

$$\alpha_R = [h_0 + (h_1 + h_{-1})\cos(\omega)]\,, \qquad \text{and} \tag{5.10}$$

$$\phi(\omega) = \arctan\left[\frac{(\mathrm{h}_1 - \mathrm{h}_{-1}\sin(\omega)}{\alpha_\mathrm{R}}\right]. \tag{5.11}$$

5.1.2 Atmospheric Green's functions

Another well established approach to correct for the atmospheric effect is given by Farrell (1972) and followed by many others, including van Dam and Wahr (1987) and Boy et al (2001), using atmospheric Green's functions, which show in combination with a local reduction coefficient similar results to the frequency dependent admittance with a better performance regarding long-period components (Kroner and Jentzsch, 1999).

The direct Newtonian attraction corresponds to a direct gravitational attraction by the air masses above the gravimeter. For a stratified atmosphere of finite thickness and a height-dependent variation of pressure, temperature and humidity, it is defined as (Merriam, 1992):

$$\delta g_{Newtonian}(\theta, \lambda, t) = \iiint_{Atmosphere} GS(\psi, z')\rho_A(\theta', \lambda', z')dv'\,, \tag{5.12}$$

where ψ is the angular distance between the station with the spherical coordinates (θ, λ) and the atmospheric volume element of density ρ_A with coordinates (θ', λ'):

$$\cos\psi = \cos\theta\cos\theta' + \sin\theta\sin\theta'\cos(\lambda - \lambda')\,. \tag{5.13}$$

The Green's function in this case is formulated as:

$$GS(\psi, z) = \frac{G[a - (a+z)\cos\psi]}{[a^2 + (a+z)^2 - 2a(a+z)\cos\psi]^{2/3}}\,, \tag{5.14}$$

where z' is the altitude of the atmospheric volume element ρ_A, a the Earth radius and G the Newtonian constant of gravitation.

Following this approach, it is necessary to estimate the density over the whole three-dimensional atmosphere. Using numerical weather models and considering the relations between temperature T, specific humidity q and pressure p, the atmospheric density ρ_A can be written as

$$\rho_A = \frac{p}{RT(1 - q + \frac{q}{\varepsilon})} = \frac{p}{RT_v}\,, \tag{5.15}$$

where $\varepsilon = 0.62197$ is the quotient of the universal gas constant for dry air and T_v denotes the virtual temperature (Boy et al, 2001), see also Chap.3.1.3:

$$T_v = T(1 - q + \frac{q}{\varepsilon})\,. \tag{5.16}$$

Calculating the density element ρ_A and performing the convolution with the Green's functions $GS(\psi, z)$ for the 3D-atmosphere needs a considerable amount of computational resources. Thus an approximation of the three-dimensional convolution by a two-dimensional convolution, where only the surface pressure is needed, will be introduced.

Assuming that all the atmospheric mass is reduced to a thin layer on the Earth's surface (see also Chap. 4.3.1) the surface atmospheric density $\rho_S(\theta', \lambda')$ can be linked directly to the

surface pressure variation $\Delta p_S(\theta', \lambda')$ through the mean surface gravity g_0 (Boy et al, 2001):

$$\Delta p_S(\theta', \lambda') = \rho_S(\theta', \lambda') g_0 \,. \tag{5.17}$$

In this case the the direct Newtonian attraction equals:

$$\delta g_{Newtonian}(\theta, \lambda, t) = \iint\limits_{Earth} GN(\psi) \Delta p_S(\theta', \lambda', z') \mathrm{d}s' \,, \tag{5.18}$$

with $\mathrm{d}s' = \sin\theta' \mathrm{d}\theta' \mathrm{d}\lambda'$ as surface element.

For this model the Newtonian Green's functions *GN* are defined as:

$$GN(\psi) = -\frac{G}{g_0 a^2} \sum_{n=0}^{+\infty} n P_n(\cos\psi) \,, \tag{5.19}$$

with P_n being the Legendre Polynomial of degree n. A convenient way to calculate the sum over $nP_n(\cos\psi)$ can be found in the Appendix 1 of (Farrell, 1972).

This model allows much shorter calculation times due to neglecting the third dimension of the atmosphere. But also the curvature of the atmosphere is not accounted for, meaning the relative position of the atmospheric masses above or under the local horizon are ignored.

5.1.3 Geometrical approach

Numerical weather models (NWM), describing the density distribution within the whole atmosphere, allow a more comprehensive approach by taking into account the vertical and horizontal expansion and permitting the separation of the direct and indirect effect. Among others Neumeyer et al (2004), Gitlein and Timmen (2006), Sato et al (2006) and Klügel and Wzionek (2009) used three-dimensional global weather data to determine the atmospheric attraction by implementing attraction models based on the point mass attraction or the potential of the air masses.

According to Newton's law, the attraction of a volume element with respect to the station is

dependent on its mass and the distance between the volume element and the station. Assuming that the atmosphere represents an ideal gas and p_b and p_t are the pressure at the bottom and top of each pressure layer, the density of the atmosphere ρ_a can be written as

$$\rho_a = \frac{p_b + p_t}{2R_d T_v}, \tag{5.20}$$

with R_d the universal gas constant for dry air and T_v the virtual temperature (see Sec. 5.1.2). The gravitational attraction of a cell with this density ρ_a and the volume V at the distance d can be calculated as follows Klügel and Wzionek (2009):

$$\delta g_d = \frac{G\rho_a V}{d^2}, \tag{5.21}$$

with G being the gravitational constant.

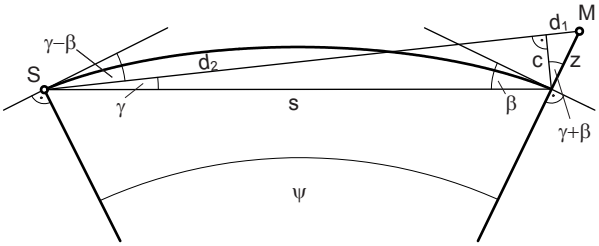

Figure 5.1: Geometric relations between station S and attracting mass M

According to Fig. 5.1 the distance d between the station S and the mass element M can be obtained from the spherical distance ψ, the elevation angle γ, the Earth radius r and the height z of the cell above ground, following:

$$tan(\gamma) = \frac{\cos(\psi/2)}{(2r/z+1)\sin(\psi/2)}, \qquad rmand \tag{5.22}$$

$$d = 2r\sin(\psi/2)\cos(\gamma) + z\sin(\psi/2+\gamma). \tag{5.23}$$

The gravitational attraction in Eq. (5.21) can be split up in the three components of a local coordinate system at the station with x pointing west, y north and z upwards, like:

$$\delta g_x = g_d(\cos(\gamma - \psi/2)\sin\alpha, \tag{5.24}$$

$$\delta g_y = g_d(\cos(\gamma - \psi/2)\cos\alpha\,, \tag{5.25}$$

$$\delta g_z = g_d(\cos(\gamma - \psi/2)\,, \tag{5.26}$$

where α is the azimuth of the mass point.

To model local phenomena properly it might be inadequate to use point masses, but be necessary to take into account the spatial spread of the cell. In such a case the vertical attraction of each cell has to be computed analytically. For example the attraction of a cylinder can be calculated as (Klügel and Wzionek, 2009):

$$\delta g_z = 2\pi G\rho_A\left(z_b - z_t + \sqrt{z_b^2 + r^2} - \sqrt{z_t^2 + r^2}\right), \tag{5.27}$$

where $z_b - z_t$ is the height of one cylinder disc and r the radius. For other geometrical figures see Mader (1951) and Nagy et al (2000).

5.1.4 ATMACS

ATMACS (Klügel and Wzionek, 2009) is a service providing time series of atmospheric vertical mass attraction, computed on the basis of weather models of the German Weather Service (DWD): the regional model COSMO-EU and the global model GME. Differently to the approaches described above, it does not use one, but combines several approaches to compensate for the deficiencies of the singular one and get an optimum result. Therefore both DWD-models are nested forming a regional and a global part, whereas the regional model is adapted around a spherical distance of 10° radius around the station. This one is used for a full 3D attraction computation, whereas from the global model only the surface pressure is used for air mass computation (2D solution). Additionally a local cylinder model is established in the vicinity of the observation point as described in the previous section. The attraction effect of each sub-model is calculated and the sum of the local, regional and global contribution give then the total effect. Additionally also the loading effect is available. The atmospheric corrections are available for 13 European SG-stations with a temporal resolution of 6 hours and can be downloaded at `atmacs.bkg.bund.de`.

5.1.5 Atmospheric Gravity Coefficients for SG

In contrast to the methods introduced before, where the gravity anomaly is determined for a specific point, i.e. station, AGC allow to determine the atmospheric gravity anomalies on a global scale. Following Torge (1989) the gravity anomaly Δg can be expressed using the spherical harmonic coefficients by

$$\Delta g(r) = \frac{GM}{r^2}\left\{\sum_{n=2}^{\infty}(n-1)\left(\frac{a}{r}\right)^n \sum_{m=0}^{n}\overline{P}_{nm}(\cos\theta)(\Delta C_{nm}\cos m\lambda + \Delta S_{nm}\sin m\lambda)\right\}. \quad (5.28)$$

As an example the pressure variation at the surface at 00 UTC of January 1, 2008 (Fig. 5.2(a)) and the corresponding gravity anomaly calculated from AGC following the VI approach (see Chap. 4.3.2) in nm s^{-2} (Fig. 5.2(b)) is shown.

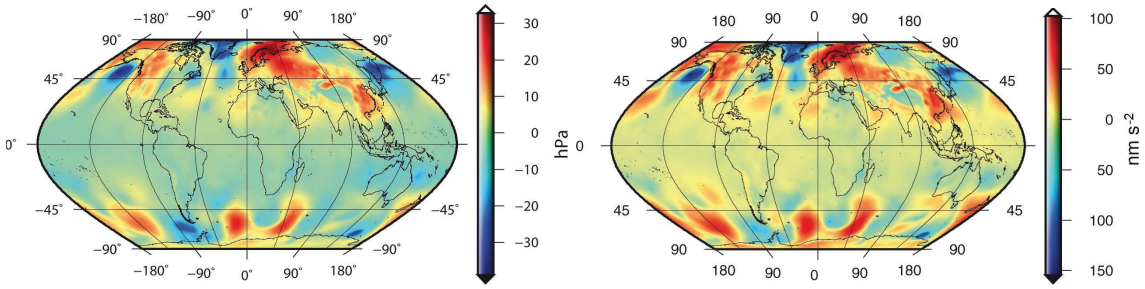

(a) (b)

Figure 5.2: **a)** Pressure variation (actual-mean) in hPa at 1 January 2008, 00 UTC. **b)** corresponding gravity anomaly in nm s^{-2} .

One can notice the high correlation between the surface pressure in Fig. 5.2(a) and the gravity anomaly in Fig. 5.2(b), which is much higher compared to the gravity potential expressed in geoid height as seen in Fig. 4.5(b). This can be explained by the higher waiting of the coefficients of higher degree and order, see Eq. 5.28 for the gravity anomaly and Eq. 2.25 for the gravity potential.

5.1.6 Elastic contribution

The elastic contribution of atmospheric gravity effects δg originate from the deformation due to mass load on the crust and from the resulting redistribution of the masses within the solid Earth. Similar to the approach used for gravity satellite missions in Chap. 4.3.3 the

load Love numbers can be used (Hinderer and Legros, 1989). Following Farrell (1972) and Boy et al (2001) the elastic Green's function equals to

$$GE(\psi) = -\frac{G}{g_0 a^2} \sum_{n=0}^{+\infty} [2h_n - (n+1)k_n] P_n(\cos\psi)\,, \tag{5.29}$$

with

$$\delta g_{Elastic}(\theta,\lambda) = \iint_{Earth} GE(\psi)\Delta p_s(\theta',\lambda')\mathrm{d}s'\,, \tag{5.30}$$

Given that the indirect effect has an amplitude approximately ten times smaller then the direct effect, the vertical expansion of the atmosphere can be neglected and a thin layer loading hypothesis can be assumed. For accurate estimates of the Green's functions the computation of the load Love numbers up to high spherical harmonic degrees (n=9000 corresponding to a spacial resolution of 2 km) are needed. To avoid such immense computational expanses, tabulated values for $GE(\psi)$ are available (see Merriam (1992)).

For both effects, indirect and direct, the introduced change in gravity δg are only functions of the change in surface pressure Δp_s and can be summed up as

$$\delta g_{Newtonian+Elastic}(\theta,\lambda) = \iint_{Earth} (GN(\psi) + GE(\psi))\Delta p_s(\theta',\lambda')\mathrm{d}s'\,. \tag{5.31}$$

5.2 Comparison of the methods and models

In this chapter some of the previously discussed methods will be compared and evaluated using the SG stations at Membach, Belgium and Conrad Observatory, Vienna as test sites. Of special interest are the methods using NWM, i.e. ATMACS and AGC. The following results will be published by Karbon et al (2013).

5.2.1 SG stations and data

For this study data from the SG at Conrad Observatory (CO) and Membach (MB) are used. The Conrad Observatory is located in the Northern Calcareous Alps about 60 km Southwest of Vienna, Austria, at approximately 1000 m above sea level. The SG GWR-C025 is operated by ZAMG (Zentralanstalt für Meteorologie und Geodynamik) and was moved

after 12 years in Vienna to the new station in November 2007 (Meurers, 2010). The Royal Observatory of Belgium installed in August 1995 a SG GWR-C021 at the underground geodynamic station Membach at 250 m above sea level, about 150 km East of Bruxelles (Francis et al, 2004).

The test data set for CO covers the full year 2008, that for MB the year 2006 showing some data gaps; both were processed by B. Meurers at University of Vienna. At every full hour besides metadata like date and time, the following parameters are available:

- gravity anomaly at the station,
- Length of day (LOD) correction,
- Pole tide correction,
- Linear drift,
- Non linear drift,
- air pressure measured at station,
- global and regional pressure correction derived from ATMACS,
- local pressure correction obtained by applying a single admittance factor retrieved through tidal analysis to the remaining pressure difference between ATMACS and the pressure measured at the station, and
- gravity anomaly at the station corrected for all effects: UniVie-final.

5.2.2 Comparison of the surface pressure data

To get a first idea of the quality of models, the surface pressure values given by ECMWF (used in AGC) and by DWD (used in ATMACS) are compared with the pressure measured at the stations. As can be seen in Fig. 5.3 for both stations, MB and CO, the differences of the models with respect to the measurement at the stations are in the range of a few hPa, for CO the range of the deviation of ECMWF is 9.1 hPa with a standard deviation of 0.97 hPa and for DWD 9.3 hPa and 1.3 hPa, respectively. For Membach both models show a better

agreement (ECMWF: 5.3 hPa / 0.7 hPa , DWD: 5.8 hPa / 0.7 hPa), which may be related to the smoother topography around that station.

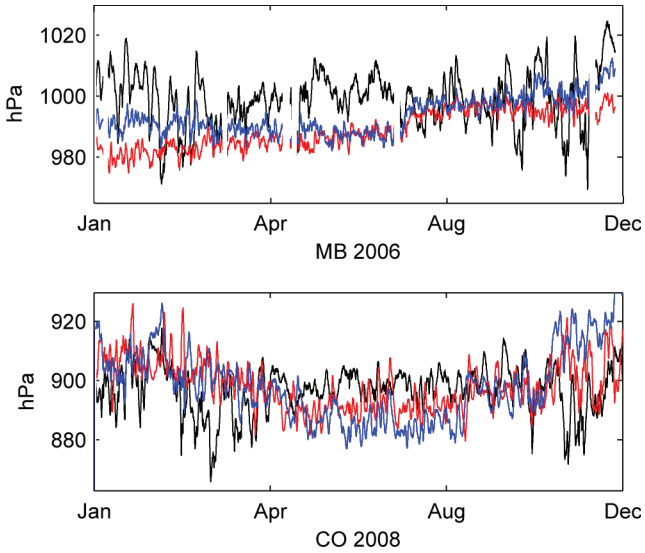

Figure 5.3: Pressure measured at station (black) and the differences with respect to DWD (red) and ECMWF (blue) multiplied by 10, shifted to the mean pressure, filtered with 24h averaging window. Upper plot: Membach (MB), lower plot: Conrad Observatory (CO).

5.2.3 Comparison of different models

As introduced in 5.1.5 the approach using AGC allows to determine the atmospheric gravity anomalies on a global scale. As an example the difference between the gravity anomaly calculated from AGC following the VI approach and the traditional with a regression coefficient of -3 nm s^{-2} per hPa as recommended in the IAG resolution (Chap. 5.1.1) at 00 UTC of January 1, 2008 is shown in Fig. 5.4. The values spread from -53.7 nm s^{-2} to 17.2 nm s^{-2} with an RMS of 6.4 nm s^{-2} over the whole globe. Within central Europe the differences range between -20 nm s^{-2} and -3 nm s^{-2}, a significant difference.

To investigate the performance of the AGC, comparisons with other models are made. Besides a simple admittance approach ATMACS (Chap. 5.1.4) as another model based on NWM is used. Additionally the Newtonian Green's function formalism (GN) (Chap. 5.1.2) is applied for station CO. As a basis for the GN surface pressure fields from ECMWF with a spatial resolution of 0.1° x 0.1° covering a circular area with a radius of 10° around CO are used. The resulting atmospheric gravity corrections are then exchanged with the global and regional portions of the atmospheric corrections given in 5.2.1 and then compared to the

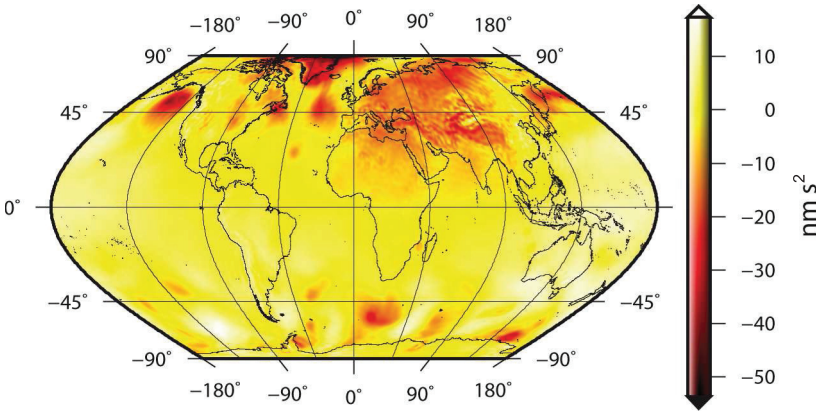

Figure 5.4: Difference between the corresponding gravity anomaly calculated from AGC following the VI approach and the single admittance factor -3nm s^{-2}/hPa at 1 January 2008, 00 UTC.

final gravity anomaly calculated by B. Meurers, called UniVie-final.

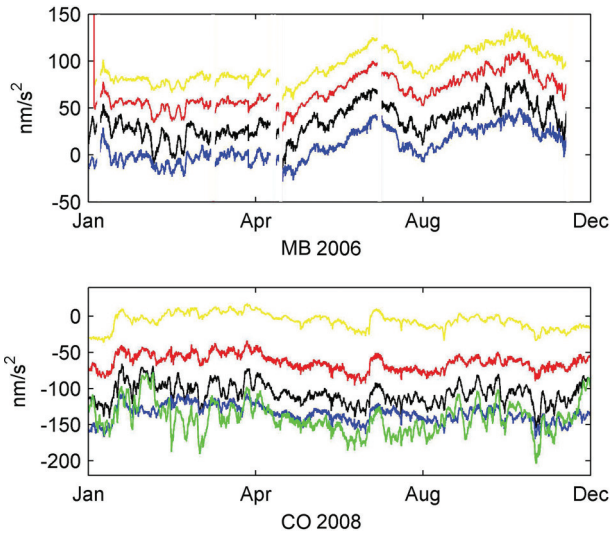

Figure 5.5: Residuals: UniVie-final (yellow), using ATMACS (black), AGC (blue), admittance (red) or GN (CO only, green) as atmospheric correction. Upper plot: Membach (MB), lower plot: Conrad Observatory (CO).

When looking at the resulting residuals (measured gravity anomaly at the stations minus the corrections) in Fig. 5.5, all approaches show good agreement, except the GN-approach used for station CO. This can be explained by the nature of Green's functions which are designed to capture large scale effects, e.g. loading effects; but in the current investigation, where small pressure anomalies should be modeled and also due to the small base area of 10° radius, this approach is less efficient.

Also it becomes evident that ATMACS shows a larger variability at both stations, in MB

always except summer, at CO only except for the time span April to July. This effect can be related to the higher pressure variability within the model used by ATMACS (Fig. 5.3). However, based solely on the comparison of surface pressure data this argumentation cannot be conclusive. A further relation to the topography and the precipitation is possible. As Boy et al (2001) have shown in case of the station of Table Mountain (Boulder, Colorado), high topographic variations around the gravimeter can have a significant effect on the Newtonian attraction. This may also be the case for CO. Further it must be noted that AGC, GN and ATMACS as used in this comparison do not consider the loading effect, whereas the admittance approach includes it indirectly, and in the solution given by UniVie-final it is also considered.

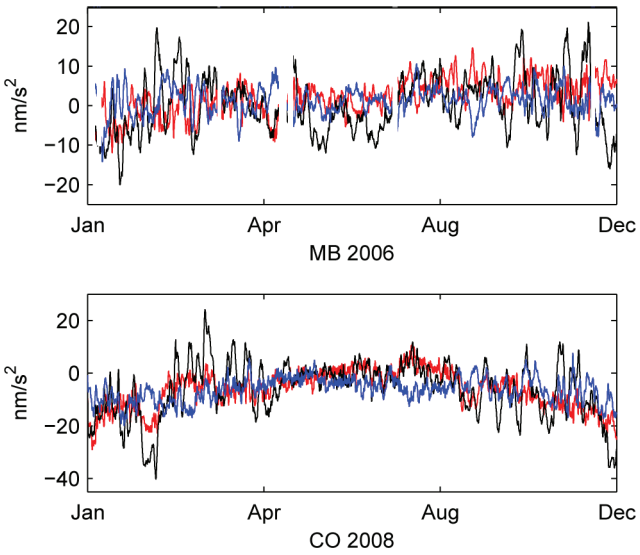

Figure 5.6: Differences of the residuals with respect to UniVie-final using ATMACS (black), AGC (blue) or admittance (red), filtered with 12h averaging window. Upper plot: Membach (MB), lower plot: Conrad Observatory (CO).

Looking at the differences of the various residuals with respect to the ones given by UniVie-final in Fig. 5.6 and their statistical properties listed in Table 5.1, this higher variability becomes even more evident. Despite all time series showing almost the same mean deviation of -2.3 nm s^{-2} for MB and -6.2 nm s^{-2} for CO, the standard deviation of ATMACS amounts to 6.17 nm s^{-2} and is almost twice as large as AGC with 3.25 nm s^{-2}. This is similar for CO where ATMACS shows with 10.56 nm s^{-2} an even higher discrepancy between its standard deviation compared to the one using AGC with 4.81 nm s^{-2}. The admittance approach yields for both stations results between AGC and ATMACS with a standard deviation of 3.54 nm s^{-2} for MB and 7.21 nm s^{-2} for CO.

Table 5.1: Statistical properties of the differences of the various residuals with respect to the ones given by UniVie-final in nm s^{-2}. The first value represents Membach (MB), the second Conrad Observatory (CO).

all values in nm s^{-2}	mean deviation MB / CO	std. deviation MB / CO	correlation MB / CO
ATMACS	-2.3 / -6.2	6.17 / 10.56	0.91 / 0.69
AGC	-2.3 / -6.2	3.25 / 4.81	0.98 / 0.92
GN	xxx / -6.2	xxx / 20.16	xxx / 0.35
admittance	-2.3 / -6.2	3.54 / 7.21	0.96 / 0.79

Interestingly, for CO also the correlation with the result of UniVie-final follows the same pattern; AGC has the highest correlation with 0.92, the admittance approach follows with 0.79 and then ATMACS with 0.69. This result is remarkable considering UniVie-final uses ATMACS to correct the global and regional component of the atmospheric attraction for its final result. For MB on the other hand, no significant differences in the correlation arise (see Table 5.1).

5.2.4 Impact of the vertical expansion of the atmosphere

Regarding the vertical distribution of air masses Klügel and Wzionek (2009) and Abe et al (2012) showed that the 3D mass attraction acting on SG is much smaller than previously estimated by various authors (Boy et al, 2001; Neumeyer et al, 2004). In case of AGC the vertical distribution is taken into account by using VI as it was shown in Chap. 4.4.2 and regarding satellite gravity missions the impact is significant. Concerning the usage of AGC for the determination of gravity corrections for SG the difference between the TL and VI approach is remarkably small.

Figure 5.7 shows the atmospheric gravity corrections at CO derived from the VI approach in blue and the difference with respect to the TL approach in black, multiplied by the factor 10. The mean deviation between both approaches is 1.32 nm s^{-2}, the standard deviation 0.5 nm s^{-2}; for MB it is larger with 1.6 nm s^{-2} and 0.7 nm s^{-2}, respectively. This confirms the findings by Abe et al (2012) who state that the effect of the actual vertical distribution is not obvious.

Further, in contrast to the findings by Merriam (1992), deeming the attraction effect caused by the masses 50 km around the station to be the biggest contributor, it becomes evident, that

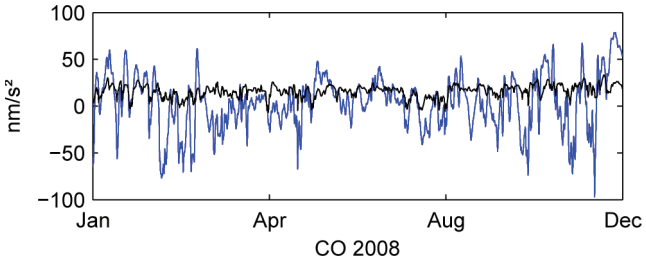

Figure 5.7: Atmospheric gravity following VI (blue) and the difference with respect to TL (black) multiplied by 10.

the AGC developed to degree and order 100, corresponding to horizontal resolution of about 200 km, are sufficient to remove the majority of the atmospheric attraction.

Chapter 6

Summary, conclusions and outlook

Atmospheric mass is only about one millionth of the mass of the solid Earth, but it has the largest temporal variation compared to the hydrological, cryospheric, oceanic and solid earth signals. The amplitude of its mass variation is similar to that of the hydrological signal. Unlike the tidal signals, the atmospheric variation has wide temporal and spatial spectra, making the modeling of this signal and the determination of its error very complicated. On the other side, satellite gravity missions such as GRACE provide an unprecedented accuracy but they require for this also an accurate modeling of the atmosphere to separate other signals of interest.

In this research the state of the art methods for correcting ground based and space borne gravity measurements were investigated. Special attention was paid to a consistent use of the meteorological data, especially the definition of the topography. A procedure was developed which allows to reduce all the NWM-data to ETOPO5 and introduces background information of the geoid to get the corresponding gravity acceleration at all points at all levels. Further a software has been developed, calculating atmospheric gravity coefficients for correcting atmospheric effects on gravity measurements including atmospheric loading and atmospheric tides corrections.

As already mentioned previously it is not possible to estimate the impact of the aliasing effect and other miss-modeling of the atmosphere straightforwardly, as the true state of the atmosphere and thus its impact on the gravity measurements is unknown. Nevertheless we were able to provide valuable insight in the processing strategies and parameterizations, although

many of the discussed issues do not have a significant impact on todays error level. However, it was shown, that when aiming for sub-monthly gravity field solutions and for next generation gravity missions these effects gain in importance and have to be considered thoroughly.

One big error contributor to the gravity change recovered by GRACE are the pressure errors and uncertainties in the NWM. Several studies showed that the pressure error should nor exaggerate 1hPa (Velicogna et al, 2001; Shengjie, 2006). Different realization of one NWM as model and pressure level were examined and models of two different providers, ECMWF and NCEP were compared. Looking at the discrepancies between the models, we found that the main contributer is the underlying orography/topography of the models. Whereas the differences between model level and pressure level of ECMWF amount to 30hPa, for ECMWF and NCEP they can reach several hundred hPa on a daily timescale. Therefore the topographical effect has to be taken care of when NWM adopt different terrain models. This issue gets more important the shorter the timescale, so for monthly solutions the impact seems negligible, where for specific epochs the differences can arise to several cm in geoid height. By subtraction of a mean field these effects of the topography can be reduced significantly, but this does not account for changes of topography within the NWM which occur occasionally. To get rid of these error sources we introduced ETOPO5 as our terrain model and referenced all the meteorological data to it. Doing so we are independent of the models definition of the topography as well as its changes.

Concerning the two different approaches, thin layer and vertical integration, we have shown that on todays error level the difference between the two is too small to have a significant effect. The differences have shown an amplitude of 1 mm for specific epochs, an accuracy not yet reached by GRACE. A reason for that might be a possible compensation of the atmospheric structure and the gravity variations when removing the mean field.

On the other hand the impact of the definition of this mean field, i.e. of the mean state of the atmosphere, was shown clearly. It has a definite effect on the de-aliasing product, as it could also be confirmed by comparison of our de-aliasing product with the GRACE operational product provided by GFZ (AOD1B). The differences here, although not significant for todays processing, can be traced straight back to the mean field. This underlines the necessity of a consistent definition of a atmospheric mean field or at least a detailed description as

to how the mean field was created. Otherwise comparisons between different products get increasingly difficult, as the effects introduced by the mean field dominate all other possible signals. For the CNES/GRGS de-aliasing product the differences are larger and of different nature and could be related to a different definition of the coordinate system, although this assumption could not be confirmed as no concrete information about the processing is available. This again stresses the necessity of a careful documentation of all introduced models and parameters as well processing strategies.

Further it was shown that changes in the approximations of the Earth, i.e. the usage of constants for the radius and gravity acceleration, have a negligible effect on the de-aliasing product, as well as the approximations of the geoid used in the processing of AOD1B. For atmospheric loading, on the other hand we were able to confirm the importance of the correction for atmospheric loading, at least for wavelengths longer than 1500 km for release 05. An important contribution to the GRACE de-aliasing process are the atmospheric tides, where S1 and S2 tides have an measurable effect on the lower degrees and thus their correction can significantly improve the results. The S3 tide on the other hand has a very small impact, but still should be corrected for if possible to help GRACE reaching its baseline performance.

Additionally a quick look at the impact of the atmospheric signals on GOCE was given and could confirm previous findings stating that the SGG is insensitive to such signals at the current level.

In the second part of this work we applied the AGC, originally developed for satellite missions, to ground based gravity measurements given by superconducting gravimeters. Not only was it possible to offer an alternative product supplying atmospheric gravity anomalies, but also to provide a still pending ground proof of the AGC.

The computation of atmospheric gravity anomalies using operational NWM is a valuable method to correct ground based gravity measurements. The main advantage is that NWM allow to introduce the physical processes of mass changes in the atmosphere rather than following an empirical fitting process as used by e.g. admittance models. This approach is also able to account for phenomena where the attraction components do not correlate completely with the pressure at the station. Furthermore the direct and indirect effect can be treated separately. Unfortunately up to now all approaches using three-dimensional NWM (e.g. ATMACS) are available only for specific SG stations which are within the coverage

of the weather model used. We showed in this study that by using AGC this deficiency can be overcome as they provide global coverage. Hence atmospheric corrections can be derived easily for every position on Earth. Further, using the SG at Conrad Observatory and Membach we were able to proove that the AGC model provides smaller residuals than the traditional admittance approach and can also hold up to the much more complex model used by ATMACS.

This disproves partially the theory that the largest effect on SG are due to the masses within 50 km, as the performance of the AGC with a spatial resolution of 200 km is remarkably good. Further, neglecting the vertical expansion when calculating the AGC has a very small effect, with standard deviations smaller than 1 nm s^{-2} on both stations treated in our investigation. This also confirms more resent findings stating that the effect of the vertical mass distribution is not big enough to be considered, allowing much simpler modeling.

We have shown that accurate atmospheric modeling is important for reducing the total errors in GRACE gravity estimation. Improving the atmospheric modeling a as background model for de-aliasing of the high frequency variations is expected to have significant impacts on the GRACE gravity solution, especially over the Antarctic region. Unfortunately no real error of the NWM as well as the de-aliasing modeling are available, thus simulations based on model difference have to be used, which may not reflect the real error distribution. Correlation of the data and models might lead to underestimating these errors. Here the link to SG can give an valuable ground proof.

The NWM operational models on the other hand are continuously improving their skills with better physical and dynamic modeling and by incorporating new satellite observations. Monitoring the change of NWM models can reduce the artificial errors introduced by the new data, e.g. the trends introduced by adding new satellite observations. But all these changes in the models also lead to problems if not treated carefully, this must be kept in mind if using the NWM operational data directly.

Bibliography

Abe M, Kroner C, Neumeyer J, Chen X (2012) Assessement of atmospgheric reductions for terrestrial gravity observations. Bulletin d'Informations Marées Terrestre, 146, pp 11825-11845

Abrikosov O, Jarecki F, Müller J, Petrovic S, Schwintzer P (2006) The impact of temporal gravity variations on GOCE gravity field recovery. Flury et al (eds), Observation of the Earh system from space, Springer, Heidelberg, pp 255269

Ahrens CD (2005) Essentials of Meteorology. Thomson Brooks/Cole

Baker T (1980) Tidal gravity in Britain: tidal loading and the spatial distribution of the marine tide. Geophysical Journal Royal Astronomical Society, 62, pp 249-267

Balton D (1980) The computation of equivalent potential temperature. Monthly Weather Review, 108, pp 1046-1053

Bettadpur S (2007) UTCSR level-2 processing standards document for level-2 product release 0004. CSR Publication GR-03-03

Böhm J, Heinkelmann R, Schuh H (2008) Reference pressure for the global geodetic observing system ggos. IVS Memorandum 2009-002v0-1 URL `ftp://ivscc.gsfc.nasa.gov/pub/memos/ivs-2008-002v01.pdf`

Bouman J, Rispens S, Gruber T, Koop R, Schrama E, Visser P, Tscherning C, Veicherts M (2008) Preprocessing of gravity gradients at the GOCE high-level processing facility. Journal of Geodesy, doi: 101007/s00190-008-0279-9

Boy JP, Chao BF (2005) Precise evaluation of atmospheric loading effects on Earths time-variable gravity field. Journal of Geophysical Research, 110, B08412, doi: 101029/2002JB002333

Boy JP, Gegout P, Hinderer J (2001) Reduction of surface gravity data from global atmospheric pressure loading. Geophysics Journal International, 149, pp 534-545

Boy JP, Longuevergne L, Boudin F, Jacob T, Lyard F, Llubes M, Florsch N, Esnoult MF (2009) Modelling atmospheric and induced non-tidal oceanic loading contributions to surface gravity and tilt measurements. Journal of Geodynamics, 48, pp 182-188

Bruinsma S, Lemoine J, Biancale R, Vals N (2010) CNES/GRGS 10-day gravity field models (release 2) and their evaluation. Advanced Space Research, 45, pp 587-601

Carnal O, Mlynek J (1991) Youngs double-slit experiment with atoms - a simple atom interferometer. Physical Review Letters, 66(21), pp 2689-2692

Chen JL, Wilson CR, Eanes RJ, Nerem RS (1999) Geophysical interpretation of observed geocenter variations. Journal of Geophysical Research, 104, B2, pp 2683-2690

Cheng MK, Shum CK, Tapley BD (1997) Determination of long-term changes in the earth's gravity field from satellite laser ranging observations. Journal of Geophysical Research, 102(B10), 22, pp 377-390, doi:101029/97JB01740

Crossley D, Hinderer J (2009) GGP (Global Geodynamics Project): an international network of superconducting gravimeters to study time-variable gravity. IAG Symposia, Volume 135, pp 627-635, doi: 101007/978-3-642-10634-7-83

Crossley DJ, Jensen OG, Hinderer J (1995) Effective barometric admittance and gravity residuals. Physics of the Earth and Planetary Interiors, 90, pp 221-241

van Dam T, Wahr JM (1987) Displacements of the Earths surface due to atmospheric loading: Effects on gravity and baseline measurements. Journal of Geophysical Research 92(82), pp 1281-1286

Davisson C, Germer LH (1927) Diffraction of electrons by a crystal of nickel. Physical Review 30, 705740

deBroglie L (1924) Recherches sur la théorie des quanta (Researches on the quantum theory). PhD thesis, Paris, Ann. de Physique (10) 3, 22

Dickman SR (1988) Theoretical investigation of the oceanic inverted barometer hypothesis. Geophysical Research, 93, pp 14941-14946

Dobslaw H, Thomas M (2007) Simulation and observation of global ocean mass anomalies. Journal of Geophysical Research, 112, C05040

Dong D, Dickey O, Chao Y, Cheng M (1998) Geocenter variations caused by mass redistribution of surface geophysical processes. IERS Technical Note, 25, pp 47-54

Drewes H, Reigber C (2005) The Global Geodetic Observing System (GGOS) of the International Association of Geodesy. FIG Working Week 2005 and GSDI-8

Drinkwater M, Floberghagen R, Haagmans R, Muzi D, Popescu A (2003) GOCE: ESAs first Earth explorer core mission. Beutler et al (eds), Earth gravity field from Space-from sensors to Earth Science, Space Sciences Series of ISSI, 18, pp 419-432, ISBN:1-4020-1408-2

Egbert GD, Erofeeva L (2002) Efficient inverse modeling of barotropic ocean tides. Journal of Atmospheric and Oceanic Technolgy, 19

Ekholm N (1902) Über die Höhe der homogenen Atmosphäre und die Masse der Atmosphäre. Meteorologische Zeitschrift, 19, pp 249-260

Farrell WE (1972) Deformation of the Earth by Surface Loads. Reviews of Geophysics and Space Physics, 10, 3, pp 761-797

Flechtner F (2007) GRACE AOD1B Product Description Document for Product Releases 01 to 04 (Rev. 3.1, April 13, 2007). URL `http://www.gfz-potsdam.de/aod1b`

Flechtner F, Dahle D, Neumayer K, Koenig R, Foerste C (2010) The release 04 CHAMP and GRACE EIGEN gravity field models. Flechtner, F, Gruber, T, Güntner, A, Mandea, M, Rothacher, M, Schöne, T, Wickert, J (Eds), System Earth via Geodetic-Geophysical Space Techniques, Springer, 41-58

Flechtner F, Morton P, Watkins M, Webb F (2012) Status of the GRACE-FO Mission. accepted for Proceedings of the International Association of Geodesy Symposium "Gravity, Geoid and Height Systems", Venice, Italy, October 9-12, 2012, Manuscript Number IAGS-D-12-00138

Francis O, Van Camp M, van Dam T, Warnant R, Hendrickx M (2004) Indication of the uplift of the Ardenne in long-term gravity variations in Membach (Belgium). Geophysical Journal International, Vol 158, pp 346-352

Fuchs K, Soffel H (1984) Geophysics - Geophysics of the Solid Earth, the Moon and the Planets - Subvolume A. Springer-Verlag

Gegout P (2009) Background models used in geodetic data processing. URL `http://www.igcp565.org/workshops/Graz/pdfs/B3_04_Gegout_BackgroundModels_IAG2009.pdf`

Gitlein O, Timmen L (2006) Atmospheric mass flow reduction for terrestrial absolute gravimetry in the Fennoscandian land uplift network. International Association of Geodesy Symposia, 130, IV, pp 461-466

Grammeltvedt A (1969) A survey of infinite-difference schemes for the primitive equations for a barotropic fluid. Monthly Weather Review, 97, pp 384-404

Gruber T, Flechtner F (2007) Vereinfachte Darstellung der GRACE Datenanalyse. DFG-SPP 1257, Gummersbach

Gruber T, Rummel R (2006) Concept and capability of GOCE. Proceedings of the GOCINA workshop, 25, Cahiers du Centre Europeen de Geodynamique et de Seismologie, pp 31-37

Gruber T, Peters T, Zenner L (2009) The Role of the Atmosphere for Satellite Gravity Field Missions. Observing our Changing Earth, International Association of Geodesy Symposia 133, ed by M Sideris, Springer-Verlag Berlin Heidelberg

Gruber T, emotion Team, Team N (2011) Recent Studies on Future Gravity Field Missions in Europe: e.motion vs. NGGM. GRACE Science Team Meeting: GRACE Follow-On and Data Continuity

Güntner A, Creutzfeldt B, Dill R, Barthelmes F (2012) Die Variabilitt des kontinentalen Wasserkreislaufs in GRACE-Schwerefelddaten. System Erde, Vol 2(1), 26-31 doi:102312/GFZsyserde02015

Han S, Shuma C, Ditmar P, Visser P, vanBeelen C, Schram E (2006) Aliasing effect of high-frequency mass variations on GOCE recovery of the Earth's gravity field. Journal of Geodynamics, 41, pp 69-76

Heikkinen M (1979) On the Honkasalo term in tidal corrections to gravimetric observations. Bull Geod, 53, pp 239-245

Higdon RL (2008) A comparison of two formulations of barotropicbaroclinic splitting for layered models of ocean circulation. Ocean Modelling, 24, 12, pp 29-45

Hinderer J, Legros H (1989) Elasto-gravitational deformation, relative gravity changes and Earth dynamics. Geophysical Journal International, 131, pp 699-723

Hirose N, Fukumori I, Zlotnicki V, Ponte RM (2001) High-frequency barotropic response to atmospheric disturbances: Sensitivity to forcing, topography, and friction. Journal of Geophysical Research

Hofmann-Wellenhof B, Moritz H (2005) Physical Geodesy. Springer, Wien, New York

Hoinka K (2012) Mean global surface pressure series evaluated from ECMWF reanalysis data. Journal Publications Royal Meteorological Society, 124, pp 2291-2297

Honkasalo T (1964) On the tidal gravity correction. Bollettina Geofisica Teorica ed Applicata, 6, 21, pp 34-36

Hurrell JW, van Loon H (1997) Decadal variations in climate associated with the north atlantic oscillation. Climatic Change, 36, pp 301-326

IGC (1998) International Absolute Gravity Basestation Network (IAGBN), Absolute Gravity Observations, Data Processing, Standards and Station Documentation (Int. Grav. Com. - WGII: World Gravity Standards). Bureau Gravimetrique International, Bulletin d Information, 63, pp 51-57

Jacobson M (1999) Atmospheric Modeling. Cambridge University Press

Jarecki F, Müller J, Petrovic S, Schwintzer P (2005) Temporal gravity variations in GOCE gradiometric data. Gravity, geoid and space missions: GGSM 2004, IAG International Symposium Porto, Portugal, August 30September 3, 2004, Springer, pp 333-338

Kalnay E, Kanamitsu M, Kistler R, Collins W, Deaven D, Gandin L, Iredell M, Saha S, White G, Woollen J, Zhu Y, Chelliah M, Ebisuazki W, Higgins W, Janiwiak J, Mo K, Ropelewski C, Wang J, Leetmaa A, Reynolds R, Jenne R, Joseph D (1996) The ncep/ncar 40-year reanalysis project. Bulletin of the American Meteorological Society ,77, pp 437-470

Karbon M, Wijaya D, Schindelegger M, Böhm J, Schuh H (2011) Atmospheric effects on the Earth gravity field featured by TU Vienna. Österreichische Zeitschrift für Vermessung und Geoinformation, 99 Jahrgang, Heft 2/2011, pp 122-130

Karbon M, Böhm J, Meurers B, Schuh H (2013) Atmospheric corrections for superconducting gravimeters using operational weather models. International Association of Geodesy Symposia 139, Earth on the Edge: Science for a Sustainable Planet, Chris Rizos, Pascal Willis (Eds), ISBN 978-3-642-37221-6

Kiamehr R, Eshagh M (2008) EGMlab, a scientific software for determining the gravity and gradient components from global geopotential models. Earth Science Informatics, 1, pp 93-103, doi: 101007/s12145-008-0013-4

Kim J (2000) Simulation Study of a Low-Low Satellite-to-Satellite Tracking Mission. PhD thesis, University of Texas, Austin

Klügel T, Wzionek H (2009) Correcting gravimeters and tiltmeters for atmospheric mass attraction using operational weather models. Journal of Geodynamics 48, pp 204-210

Kroner C (1997) Reduktion von luftdruckeffekten in zeitabhangigen schwerebeobachtungen. PhD thesis, Technische Universität Clausthal

Kroner K, Jentzsch J (1999) Comparison of different barometric pressure reductions for gravity data and resulting consequences. Physics of the Earth and Planetary Interiors, 115, 3-4, pp 205-218

Le Gouet J, Mehlstaeubler T, Kim J, Merlet S, Clairon A, Landragin A, Pereira Dos Santos F (2008) Limits to the sensitivity of a low noise compact atomic gravimeter. Applied Physics, B, 92(2), pp 133144

Liljequist K, Cehak G (2012) Allgemeine Meteorologie. Vieweg

Lindzen R (1979) Atmospheric tides. Annual Review of Earth and Planetary Sciences, 7, pp 199-225, doi: 101146/annurevea07050179001215

Love AEH (1909) The yielding of the earth to distributing forces. Proceedings of the Royal Society, A 82, pp 73-88

Mader K (1951) Das Newtonsche Raumpotential prismatischer Körper und seine Ableitungen bis zur dritten Ordnung. Österreichische Zeitschrift für Vermessungswesen, Sonderheft 11

Maier A, Krauss S, Hausleitner W, Baur O (2012) Contribution of satellite laser ranging to combined gravity field models. Advances in Space Research, 49, 3, pp 556565

McCarthy D, Petit G (2004) Iers conventions (2003) . (iers technical note ; 32) frankfurt am main: Verlag des bundesamts fr kartographie und geodsie, 2004. 127 pp., paperback, isbn 3-89888-884-3 (print version). IERS Technical Note, 32, Verlag des Bundesamts fr Kartographie und Geodsie, pp 127 , ISBN 3-89888-884-3

McGuirk J, Foster J GTand Fixler, Snadden M, Kasevich M (2008) Sensitive absolute-gravity gradiometry using atom interferometry. Physical Review A, 65(3,Part B), p 033608

McPhaden M (2002) El Niño and La Niña: Causes and Global Consequences. Encyclopedia of Global Environmental Change, 1, John Wiley and Sons, LTD, Chichester, UK, pp 353-370

Merriam JB (1992) Atmospheric pressure and gravity. Geophysical Journal International, 109, pp 488-500

Meurers B (2010) Environmental effects on gravity at Conrad Observatory. EGU General Assembly 2010, Geophysical Research Abstracts, 12, EGU2010-3656

Meurers B, Dorninger M, Blaumoser N (2011) Atmospheric signals in the SG gravity record at Conrad Observatory, Austria. EGU General Assembly 2011, Geophysical Research Abstracts, 13, EGU2011-12474

Mueller H, Chiow S, Herrmann S, Chu S, Chung K (2008) Atom-interferometry tests of the isotropy of post-newtonian gravity. Physical Review Letter, 100 (3), p 031101

Müller T, Zürn W (1983) Observation of gravity changes during the passage of cold fronts. Journal of Geophysics, 53, pp 155-162

Nagy D, Papp G, Benedek J (2000) The gravitational potential and its derivatives for the prism. Journal of Geodesy, 74, 7, pp 552-560

Neumeyer J, Hagedorn J, Leitloff J, Schmidt T (2004) Gravity reduction with three-dimentional atmospheric pressure data for precise ground gravity measurements. Journal of Geodynamics, 38, pp 437-450

Newton I (1687) Philosophiae naturalis principia mathematica. London

Pail R, Metzler B, Preimesberger T, Lackner B, Wermuth M (2007) GOCE quick-look gravity field analysis in the framework of HPF. Proceedings 3rd GOCE user workshop, Frascati, ESRIN, November 2006, ESA SP-627 European Space Agency, Noordwijk, pp 325-332

Pail R, Bruinsma S, Migliaccio F, Frste C, Goiginger H, Schuh WD, Höck E, Reguzzoni M, Brockmann JM, Abrikosov O, Veicherts M, Fecher T, Mayrhofer R, Krasbutter I, Sans F, Tscherning C (2011) First GOCE gravity field models derived by three different approaches. Journal of Geodesy, Vol 85, Nr 11, pp 819-843, Springer, ISSN 0949-7714, DOI: 101007/s00190-011-0467-x

Pearlman M, Degnan J, Bosworth J (2002) The international laser ranging service. Advances in Space Research, 30, 2, pp 135-143, doi: 101016/S0273-1177(02)00277-6

Peltier W (2008) Global glacial isostasy and the surface of the ice-age Earth: the ICE-5G (VM2) model and GRACE. Annual Review of Earth and Planetary Sciences 2004 32, pp 111-49, doi: 101146/annurevearth32082503144359

Penna NT, Baker TF, Scherneck HG (2008) Assessing the accuracy of predicted ocean tide loading displacement values. Journal of Geodesy, 82 (12), pp 893-907, doi:101007/s00190-008-0220-2

Peters A, Chung K, , Chu S (2001) High-precision gravity measurements using atom interferometry. Metrologia, 38 (1), pp 25-61

Petit G, Luzum B (2012) Iers conventions (2010). IERS Technical Note, 36, Verlag des Bundesamts fr Kartographie und Geodsie, pp 179, ISBN 3-89888-989-6

Petrov L, Boy J (2004) Study of the atmospheric pressure loading signal in very long baseline interferometry observations. Journal of Geophysical Research, 109, B03405

Petrovskaya M, Vershkov A (2006) Non-singular expressions for the gravity gradients in the local north-oriented and orbital reference frames. Journal of Geodesy 80, pp 117-127, doi: 101007/s00190-006-0031-2

Plag H, Blewitt G, Herring T (2007) Towards a consistent conventional treatment of surface-load induced deformations. Position Paper presented at the IERS Workshop on Conventions, September 20-21, Sevres, France URL `http://cheryl.nbmg.unr.edu/hanspeterplag/publications/pubs/2007plagetaliersposition.pdf`

Ponte R, Gaspa P (1999) Regional Analysis of the Inverted Barometer Effect over the Global Ocean Using TOPEX/POSEIDON Data and Model results. Journal of Geophysical Research, 104, C7, pp 15587-15601

Ponte RM, Ray RD (2002) Atmospheric pressure corrections in geodesy and oceanography: A strategy for handling air tides. Geophysical Research Letters, 29, 2153, doi: 101029/2002GL016340

Rabbel W, Zschau J (1985) Static deformation and gravity changes at the earth's surface due to atmospheric loading. Journal of Geophysics, 56, pp 81-99

Reigber C (1989) Gravity field recovery from satellite tracking data. Lecture Notes in Earth Sciences, vol 25, Springer, pp 197-234

Reigber C, Jochmann H, Wnsch S Jand Petrovic, Schwintzer P, Barthelmes F, Neumayer K, Knig R, Frste C, Balmino G, Biancale R, Lemoine J, Loyer S, Perosanz F (2002a) Earth Gravity Field and Seasonal Variability from CHAMP. Earth Observation with CHAMP - Results from Three Years in Orbit, Springer, Berlin, pp 25-30

Reigber C, Luehr H, Schwintzer P (2002b) CHAMP mission status. Advanced Space Research, 30 (2), pp 129-134

Reigber C, Jochmann H, Wnsch J, Petrovic S, Schwintzer P, Barthelmes F, Neumayer KH, Knig R, Frste C, Balmino G, Biancale R, Lemoine JM, Loyer S, Perosanz F (2004) Earth gravity field and seasonal variability from CHAMP. Earth Observation with CHAMP - Results from three years in orbit, Springer, pp 25-30

Reigber C, Schmidt R, Flechtner F, Knig R, Meyer U, Neumayer K, Schwintzer P, Zhu S (2005) An Earth gravity field model complete to degree and order 150 from GRACE: EIGEN-GRACE02S. Journal of Geodynamics 39(1),pp 1-10

Rummel R, Müller J, Oberndorfer H, Sneeuw N (2000) Satellite Gravity Gradiometry with GOCE. Towards an Integrated Global Geodetic Observing System (IGGOS), IAG symposium 120, pp 66-72

Rummel R, Gruber T, Koop R (2004) High level processing facility for GOCE: products and processing strategy. LaCoste, H (ed) Proceedings of the 2nd international GOCE user workshop GOCE, The Geoid and Oceanography, ESA SP-569, ESA, ISBN:92-9092-880-8, ISSN:1609-042X

Rummel R, Weiyong Y, Stummer C (2011) GOCE gravitytional gradiometry. Journal of Geodesy, 85, pp 777-790, doi:101007/s00190-011-0500-0

Sato T, Rosat S, Tamura Y, Matsumoto K (2006) An attempt to improve the estimation accuracy of the atmospheric pressure effect. Bulletin d'Information des Marées Terrestres, 141, pp 11303-11304

Scherneck HG (1991) A parametrized solid earth tide mode and ocean loading effects for global geodetic base-line measurements. Geophysical Journal International, 106(3), pp 677-694

Schmidt M (2011) A mobile high-precision gravimeter based on atom interferometry. PhD thesis, Humboldt-Universität Berlin

Schmidt R (2006) Zur Bestimmung des cm-Geoids und dessen zeitlicher Variationen mit GRACE. PhD thesis, Friedrich-Wilhelms-Universität, Bonn

Schrödinger E (1926) An undulatory theory of the mechanics of atoms and molecules. Physical Review 28 (6), pp 10491070

Schuh H, Moehlmann L (1989) Ocean loading station displacements observed by vlbi. Geophysical Research Letters, 16, 10, pp 1105-1108, doi: 101029/GL016i010p01105

Shengjie G (2006) GPS radio occultation ans the role of atmospheric pressure on spaceborne gravity estimation over Antarctica. PhD thesis, Ohio State University

Shida T (1912) On the elasticity of the earth and the Earths crust. Memoirs of the College of Science and Engineering, Kyoto Imperial University, 4, pp 1-286

Snadden M, McGuirk M, Bouyer P, Haritos K, Kasevich M (1998) Measurement of the Earths gravity gradient with an atom interferometer-based gravity gradiometer. Physical Review Letter, 81(5), pp 971974

Sneeuw N, Flury J, Rummel R (2005) Science requirements on future missions and simulated mission scenarios. Future Satellite Gravimetry and Earth Dynamics, pp 113-142, doi: 101007/038733185910

Spratt R (1982) Modelling the effects of the atmospheric pressure variations on gravity. Geophysical Journal of the Royal Astronomical Society 71, pp 173-186

Stacey FD, Davis PM (1977) Physics of the Earth. Wiley, New York

Swenson S, Wahr J (2002) Estimated Effects of the Vertical Structure of Atmospheric Mass on the Time- Variable Geoid. Journal of Geophysical Research, 107, 2194, doi: 101029/2000JB000024

Tapley B, Bettadput S, Watkins M, Reigber C (2004) The Gravity recovery and Climate Experiment: Mission overview and early results. Geophysical research Letters, 31, L09607, doi:101029/2004GL019920

Thomas M (2002) Ocean induced variations of Earths rotation Results from a simultaneous model of global circulation and tides. PhD thesis, Univ. of Hamburg, Germany

Thompson PF, Bettadpur S, BD T (2004) Impact of short period, non-tidal, temporal mass variability on GRACE gravity estimates. Geophysical Research Letters, 31, L06619, doi:101029/2003GL019285

Thomson W (1863) On the rigidity of the Earth, shifting of the Earth instantaneous axis of rotation; the irregularities of the Earth as a timekeeper. Philosophical Transactions of the Royal Society

Tino G, Cacciapuoti L, Bongs K, Borde CJ, Bouyer P, Dittus H, Ertmer W, Goerlitz A, Inguscio M, Landragin A, Lemonde P, Lammerzahl C, Peters A, Rasel E, Reichel J, Salomon C, Schiller S, Schleich W, Sengstock K, Sterr U, M W (2007) Atom interferometers and optical atomic clocks: New quantum sensors for fundamental physics experiments in space. Nuclear Physics B, 166, pp 159165

Tomaschek R, Schaffernicht W (1957) Über die periodischen Veränderungen der Vertikalkomponente der Schwerebeschläunigung in Marburg a.d. Lahn. Sitz.Her. Ges. Befrder. Ges. Naturw.

Torge W (1989) Gravimetry. Walter de Gruyter-Berlin-New York, ISBN: 3-11-010702-3

Trenberth K, Guillemot C (1994) The total Mass of the Atmosphere. Journal of Geophysical Research, 99, D11, pp 23079-23088

Trenberth K, Smith L (2005) The Mass of the Atmosphere: A Constraint on Global Analyses. Journal of Climate, 18, 6, pp 864-875

Tscherning C (2001) Computation of spherical harmonic coefficients and their error estimates using least squares collocation. Journal of Geodesy, 75, pp 12-18, doi: 101007-s001900000150

Velicogna I, Wahr J, Van den Dool H (2001) Can Surface Pressure be used to remove atmospheric contributions from GRACE data with sufficient accuracy to recover hydrological signals? Journal of Geophysical Research, 106, B8, pp 16415-16434

Vey S, Calais E, Llubes M, Florsch N, Woppelmann G, Hinderer J, Amalvict M, Lalancette MF, Simon B, Duquenne F, Haase JS (2002) GPS measurements of ocean loading and its impact on zenith tropospheric delay estimates: a case study in Brittany, France. Journal of Geodesy, 76, 8, pp 419-427

Völgyesi L (2001) Geodetic applications of torsion balance measurements in Hungary. Reports on Geodesy, Warsaw University of Technology, 57, 2, pp 203-212

Wahr J, Molenaar M, Bryan F (1998) Time variability of the Earth's gravity Field: hydrological and oceanic effects and their possible detection using GRACE. Journal of Geophysical Research, 103, 30, pp 205-230

Warburton RJ, Goodkind JM (1977) The influence of barometric pressure fluctuations on gravity. Geophys J Roy Astron Soc, 48, pp 281-292

Watkins M, Yuan D (2007) JPL level-2 processing standards document for level-2 product release 04. URL `ftp://podaac.jpl.nasa.gov/pub/grace/doc/`

Wunsch C, Stammer D (1997) Atmospheric loading and the oceanic 'inverted barometer' effect. Reviews of Geophysics, 35, 1, pp 79-107

Yu N, Kohel J, Kellogg J, Maleki L (2006) Development of an atom-interferometer gravity gradiometer for gravity measurements from Space. Applied Physics, B 84, pp 647-652, doi: 101007/s00340-006-2376-x

Zenner L, Gruber T, Jäggi A, Beutler G (2010) Propagation of atmospheric model errors to gravity potential harmonics Impact on GRACE De-Aliasing. Geophysical Journal International, 182(2), pp 797-807

Zenner L, Gruber T, Beutler G, Jäggi A, Flechtner F, Schmidt T, Wickert J, Fagiolini E, Schwarz G, Trautmann T (2011) Using Atmospheric Uncertainties for GRACE De-Aliasing - First Results. Geodesy for Planet Earth, International Association of Geodesy Symposia, Springer, pp 147-152, ISBN 987-3-642-20337-4

Zenner L, Fagiolini E, Daras I, Flechtner F, Gruber T, Schmidt T, Schwarz G (2012) Non-tidal atmospheric and oceanic mass variations and their impact on GRACE data analysis. Journal of Geodynamics, doi:101016/jjog201201010

List of Figures

2.1 Centrifugal Force 18

2.2 Equipotential surfaces and plumb lines 19

2.3 Spherical harmonics: (a) zonal, (b) tesseral, (c) sectoral 22

2.4 Geoid and reference ellipsoid. 24

2.5 Schematics of the FG5 absolute gravimeter 27

2.6 Scheme of an atomic gravimeter, from Schmidt (2011). 29

2.7 General lever spring balance principle 30

2.8 SG principle (modified fromTorge, 1989) 31

2.9 Network of the GPP, status of 2010, source: GGP project homepage `http://www.eas.slu.edu/GGP/ggphome.html` 33

2.10 Scheme of SLR: transmit/receive telescope, puls laser, atomic clock, geodetic satellite equipped with corner cube reflectors. 34

2.11 Temporal variation of the C_{20} coefficient, in red and blue a SLR-solution, in green GRACE (Maier et al, 2012). 34

2.12 Network of SLR stations and ground tracks of seven days of geodetic SLR data, source: ILRS. 35

2.13 Scheme of CHAMP: one on-board 3-axis accelerometer, tracked by GNSS satellites 35

2.14 EIGEN-CHAMP03S Geoid in meter, Reigber et al (2004) 36

2.15 Scheme of GRACE: twin-satellites with one on-board 3-axis accelerometer and microwave ranging system, tracked by GNSS satellites 37

2.16 Mean monthly variability of continental water storage (2002-2011), Güntner et al (2012). , Reigber et al (2005) 37

2.17 Scheme of GOCE: Six on-board 3-axis accelerometers, tracked by GNSS satellites 38

2.18 First GOCE-only gravity field in meter, Pail et al (2011) 39

2.19 Effects of mass signals on spatial and temporal determination of the geoid, from Sneeuw et al (2005). 41

2.20 On the left the geometry for the problem for computing the tidal force on a point on Earth, caused by an external body M. On the right the corresponding field of forces. 43

2.21 Vertical shift of the solid Earth and its level surface caused by tidal potential. 45

3.1 **a)** Progression of the density with height and **b)** of the virtual temperature at Vienna (48N, 16E) 50

3.2 Global mean surface pressure in hPa from ECMWF analysis (1980-2009) pressure level data reduced to surface topography 53

3.3 Global mass change of the atmosphere obtained from C_{00} based on ECMWF operational analysis (1980-2009) pressure level data reduced to surface topography 54

3.4 Degree 1 coefficients using the thin layer approach, based on ECMWF operational analysis (1980-2009) pressure level data reduced to surface topography, in black C_{10}, in blue C_{11} and in red S_{11} 54

3.5 RMS of ECMWF surface pressure over the year 2008 55

3.6 **a)** S1 tide at 00 UTC in hPa. **b)** Corresponding effect on geoid in millimeter 56

3.7 Difference between ETOPO5 topography and ECMWF orography on a 1° x 1° grid. 59

3.8 Surface pressure at the Conrad Observatory for January 2008: in green ECMWF on the orography, in red ECMWF reduced to Etopo5, in blue DWD and in black in-situ measurements. 59

3.9 Global Reference Pressure 61

3.10 Difference between ECMWF and NCEP surface pressure on a 1° x 1° grid. NCEP is interpolated linearly from a 2.5° to a 1° grid. 62

3.11 Gravity variation signals from different sources in terms of degree standard deviation, in cyan daily atmosphere, blue daily ocean, green monthly hydrology, compared to mission sensitivities of CHAMP, GRACE and GOCE, modified from Flechtner (2007). 63

3.12 **a)** S2 and **b)** S3 tide at 00 UTC expressed in geoid height in millimeter. . . 65

3.13 Difference of the geoid height variation in millimeter for the thin layer approach between the variant with and without loading for January 1, 2008, 00 UTC 66

3.14 Newtonian and elastic contributions of the atmosphere to gravity changes (modified from Neumeyer et al, 2004) 66

4.1 Simplified scheme of the GRACE data analysis, modified from Gruber and Flechtner (2007). 70

4.2 On the left the conversion from the sphere to the ellipsoid, on the right the determination of the ellipsoidal height, with the bold solid line depicting the ellipsoid, the dashed one the geoid and the narrow line the topography. . . . 72

4.3 On the left the calculation of block mean values at each level, on the right the inter- and extrapolation scheme to the topography and calculation of the corresponding block mean values. 74

4.4 Difference of GRP and the mean field used for VI expressed in geoid height, in mm. 75

4.5 **a)** Pressure variation (actual-mean) in hPa at 1 January 2008, 00 UTC **b)** Resulting geoid height variation following the thin layer approach in millimeter 77

4.6 **a)**Difference between the geocentric radius to the Earth surface and the radius a = 6371 km of the mean sphere. Latitude dependent gradient removed. **b)** Difference between the gravity acceleration at Earth surface according to EGM96 and the mean gravity acceleration g_0 = 9.80665 m s^{-2}. Latitude dependent gradient removed. 79

4.7 **a)** Differences of the geoid height variation between the thin layer approach with latitude and longitude dependent radii and gravity acceleration and with constant radius a and g_0 for the epochs January 1, 2008, 00 UTC. **b)** Differences of the total atmosphere in terms of geoid height between the thin layer approach with latitude and longitude dependent radii and gravity acceleration and with constant radius a and gravity acceleration g_0 for the epoch January 1, 2008, 00 UTC. Latitude dependent gradient extracted. 80

4.8 Degree standard deviation in terms of geoid height for the year 2008 in meter derived from the thin layer approach, in blue with latitude and longitude dependent radii and gravity acceleration and in red the difference to the solution with constant radius a and constant gravity acceleration g_0. The black line marks the RL04 error level of GRACE, the dashed one the theoretical error as obtained by pre-launch simulations. 81

4.9 Degree standard deviation in terms of geoid height for the year 2008 in meter, in blue for the VI approach, in red the corresponding difference between VI and TL. The black line marks the RL04 error level of GRACE, the dashed one the theoretical error as obtained by pre-launch simulations. 82

4.10 **a)** Difference between VI and TL and **b)** the total atmosphere calculated using VI and TL for January 1, 2008 00 UTC expressed in geoid height in mm. 82

4.11 **a)** Difference between the surface pressure mean field of 2008 and 2009 and GRP and **b)** the surface pressure mean field of 2008 and 2009 and the VI mean field, expressed in geoid height in mm. 83

4.12 Difference between VI and TL using surface pressure mean field of 2008 and 2009 for January 1, 2008 00 UTC expressed in geoid height in mm. 83

4.13 Time variation of the C_{20} coefficient in geoid height for the year 2008 in millimeter, in black following the VI approach in blue the TL approach, in red the difference multiplied by 10, bias removed. 84

4.14 Degree standard deviation in terms of geoid height in meter for the year 2008, in blue for the TL approach with loading, in red the corresponding difference of VI without loading. The black line marks the RL04 error level of GRACE, the dashed one the theoretical error as obtained by pre-launch simulations. 85

4.15 Time variations of low degree coefficients expressed in geoid height in millimeter, difference between neglecting and including loading, in black C_{20}, in blue C_{30}, in red C_{40} and in green C_{50}. 85

4.16 Gravity variation signals of the S1 (blue), S2 (cyan) and S3 (yellow) tides in terms of degree standard deviation for January 1st 2008. The black line marks the RL04 error level of GRACE, the dashed the theoretical error as obtained by pre-launch simulations. The red line is the degree standard deviation for the TL approach without tidal correction, the black line with tidal correction. 86

4.17 Progress of **a)** pressure and **b)** gravity acceleration above Vienna (48 N, 16E) for January 1st 2008, 00 UTC; in red model level data, in blue pressure level data for January 1, 2008, 00 UTC. 87

4.18 Differences of the total atmosphere in geoid height between the solutions with pressure level and model level for January 1st 2008, 00 UTC. 88

4.19 Degree standard deviation in terms of geoid height for January 2008, in blue for pressure level data, in red the corresponding difference between pressure level and model level data. The black line marks the RL04 error level of GRACE, the dashed on the theoretical error as obtained by pre-launch simulations. 88

4.20 Surface pressure variation starting from 01.01.2006 00 UTC until 31.03.2010 18 UTC for a point in the Andes (lat:112; lon:291), courtesy of L. Zenner. . 89

4.21 **a)** Difference between NCEP/NCAR orography and ETOPO5 topography **b)** Difference between surface pressures taken from NCEP/NCAR and ECMWF on ETOPO5 for January 1st, 00 UTC. 90

4.22 Difference between the pressure variation calculated from NCEP/NCAR and ECMWF data in hPa for January 1st, 00 UTC. 91

4.23 Difference between geoid height variation calculated from NCEP/NCAR and ECMWF data using the TL approach in mm for January 1st, 00 (upper left), 06 (upper right), 12 (lower left) and 18 UTC (lower right). 91

4.24 Degree standard deviation in terms of geoid height in blue for the ECMWF, in red the difference between ECMWF and NCEP/NCAR for **a)** January 2008 and **b)** the epoch Jnauary 1st, 00 UTC, The black line marks the RL04 error level of GRACE, the dashed on the theoretical error as obtained by pre-launch simulations. 92

4.25 Degree standard deviation in terms of geoid height for January 2008, in blue for AGC, in cyan the difference of AGC and $\text{AOD1B}_{\text{atm}}$ and in red AGC and CNES/GRGS. The black line marks the RL04 error level of GRACE, the dashed one the theoretical error as obtained by pre-launch simulations. . . 94

4.26 **a)** Difference of AGC and GFZ_{atm} and **b)** AGC and CNES/GSGR for the epoch January 1, 2008, 00 UTC. 94

4.27 C_{20} coefficient for January 2008, in blue AGC, in black AGC without tidal correction, cyan $\text{AOD1B}_{\text{atm}}$ and red CNES/GRGS. 95

4.28 **a)** Gradient component T_{zz} for EGM96 at the surface and **b)** at GOCE altitude in Eötvös. 97

4.29 $T_{xx}, T_{yy}, T_{zz}, T_{xz}$ using the AGC of January 1st, 2008, 00 UTC. 98

5.1 Geometric relations between station S and attracting mass M 107

5.2 **a)** Pressure variation (actual-mean) in hPa at 1 January 2008, 00 UTC. **b)** corresponding gravity anomaly in nm s^{-2} 109

5.3 Pressure measured at station (black) and the differences with respect to DWD (red) and ECMWF (blue) multiplied by 10, shifted to the mean pressure, filtered with 24h averaging window. Upper plot: Membach (MB), lower plot: Conrad Observatory (CO). 112

5.4 Difference between the corresponding gravity anomaly calculated from AGC following the VI approach and the single admittance factor -3nm s^{-2}/hPa at 1 January 2008, 00 UTC. 113

5.5 Residuals: UniVie-final (yellow), using ATMACS (black), AGC (blue), admittance (red) or GN (CO only, green) as atmospheric correction. Upper plot: Membach (MB), lower plot: Conrad Observatory (CO). 113

5.6 Differences of the residuals with respect to UniVie-final using ATMACS (black), AGC (blue) or admittance (red), filtered with 12h averaging window. Upper plot: Membach (MB), lower plot: Conrad Observatory (CO). 114

5.7 Atmospheric gravity following VI (blue) and the difference with respect to TL (black) multiplied by 10. 116

Curriculum vitae

Name:	Karbon Maria
E-mail:	karbon@gfz-potsdam.de
Date of birth:	June 26, 1984
Place of birth:	Bozen/Bolzano, Italy
Nationality:	Italy

Academic Education

04/2009 – 04/2013	Vienna University of Technology, Doctoral program Technical Sciences – Geodesy
10/2003 – 04/2009	Vienna University of Technology, Master program Surveying and Geoinformation – Geodesy and Geophysics

Employment

11/2012 – present	University assistant at the Vienna University of Technology, Department of Geodesy and Geoinformation, Advanced Geodesy
10/2011 – 10/2012	Scientific research assistant at the Vienna University of Technology, Institute of Geodesy and Geophysics, Advanced Geodesy

GEOWISSENSCHAFTLICHE MITTEILUNGEN

Bisher erschienen:

Heft 1 Kolloquium der Assistenten der Studienrichtung Vermessungswesen. 1970 - 1973, Dezember 1973.

Heft 2 EGGER-PERDICH-PLACH-WAGENSOMMERER, Taschenrechner HP 45 und HP 65, Programme und Anwendungen im Vermessungswesen. 1. Auflage, März 1974, Special Edition in English, Juli 1974, 2. verbesserte Auflage, November 1974.

Heft 3 Kolloquium der Assistenten der Studienrichtung Vermessungswesen 1973 - 1974, September 1974.

Heft 4 EGGER-PALFINGER-PERDICH-PLACH-WAGENSOMMERER, Tektronix-Tischrechner TEK 31, Programmbibliothek für den Einsatz im Vermessungswesen, November 1974.

Heft 5 K. LEDERSTEGER, Die horizontale Isostasie und das isostatische Geoid, Februar 1975.

Heft 6 F. REINHART, Katalog von FK4 Horrebow-Paaren für Breiten von +30 bis +60, Oktober 1975.

Heft 7 Arbeiten aus dem Institut für Höhere Geodäsie, Wien, Dezember 1975.

Heft 8 Veröffentlichungen des Instituts für Photogrammetrie zum XIII. Internationalen Kongreß für Photogrammetrie in Helsinki 1976, Wien, Juli 1976.

Heft 9 W. PILLEWIZER, Felsdarstellung aus Orthophotos, Wien, Juni 1976.

Heft 10 PERDICH-PLACH-WAGENSOMMERER, Der Einsatz des programmierbaren Taschenrechners Texas Instruments SR-52 mit Drucker PC100 in ingenieurgeodätischen Rechentechnik, Wien, Mai 1976.

Heft 11 Kolloquium der Assistenten der Studienrichtung Vermessungswesen 1974 - 1976, November 1976.

Heft 12 Kartographische Vorträge der Geodätischen Informationstage 1976, Wien, Mai 1977.

Heft 13 Veröffentlichung des Instituts für Photogrammetrie anläßlich des 80. Geburtstages von Prof. Dr.h.c. K. Neumaier, Wien, Januar 1978.

Heft 14 L. MOLNAR, Self Checking Analytical Relative Orientation and Strip Formation, Wien, Dezember 1978.

Heft 15 Veröffentlichung des Instituts für Landesvermessung anläßlich des 80. Geburtstages von Prof. Dr. Alois Bavir, Wien, Januar 1979.

Heft 16 Kolloquium der Assistenten der Studienrichtung Vermessungswesen 1976 - 1978, Wien, November 1979.

Heft 17 E. VOZIKIS, Die photographische Differentialumbildung gekrümmter Flächen mit Beispielen aus der Architekturbildmessung, Wien, Dezember 1979.

Heft 18 Veröffentlichung des Instituts für Allgemeine Geodäsie anläßlich des 75. Geburtstages von Prof. Dipl.-Ing. Dr. F. Hauer, Die Höhe des Großglockners, Wien, 1981.

Heft 19 H. KAGER, Bündeltriangulation mit indirekt beobachteten Kreiszentren, Wien, April 1981.

Heft 20 Kartographische Vorträge der Geodätischen Informationstage 1980, Wien, Mai 1982.

Heft 21 Veröffentlichung des Instituts für Kartographie anläßlich des 70. Geburtstages von Prof. Dr. Wolfgang Pillewizer: Glaziologie und Kartographie, Wien, Dezember 1982.

Heft 22 K. TEMPFLI, Genauigkeitsschätzung digitaler Höhenmodelle mittels Spektralanalyse, Wien, Mai 1982.

Heft 23 E. CSAPLOVICS, Interpretation von Farbinfrarotbildern, Wien, November 1982.

Heft 24 J. JANSA, Rektifizierung von Multispektral-Scanneraufnahmen - Entwicklung und Erprobung eines EDV-Programms, Wien, Mai 1983.

Heft 25 Zusammenfassung der Diplomarbeiten, Dissertationen und Habilitationen an den geodätischen Instituten der TU Wien, Wien, November 1984.

Heft 26 T. WUNDERLICH, Die voraussetzungsfreie Bestimmung von Refraktionswinkeln, Wien, August 1985.

Heft 27 G. GERSTBACH (Hrsg.), Geowissenschaftliche/geotechnische Daten in Landinformationssystemen - Bedarf und Möglichkeiten in Österreich, Juni 1986.

Heft 28 K. NOVAK, Orientierung von Amateuraufnahmen ohne Paßpunkte, Wien, August 1986.

Heft 29 Veröffentlichung des Instituts für Landesvermessung und Ingenieurgeodäsie, Abt. Ingenieurgeodäsie, anläßlich des 80. Geburtstages von Prof. Dipl.-Ing. Dr. F. Hauer, Wien, Oktober 1986.

Heft 30 K.-H. ROCH, Über die Bedeutung dynamisch ermittelter Parameter für die Bestimmung von Gesteins- und Gebirgseigenschaften, Wien, Februar 1987.

Heft 31 G. HE, Bildverbesserung mittels digitaler Filterung, Wien, April 1989.

Heft 32 F. SCHLÖGELHOFER, Qualitäts- und Wirtschaftlichkeitsmodelle für die Ingenieurphotogrammetrie, Wien, April 1989.

Heft 33 G. GERSTBACH (Hrsg.), Geowissenschaftliche/geotechnische Daten in Landinformationssystemen - Datenbestände und Datenaustausch in Österreich, Wien, Juni 1989.

Heft 34 F. HOCHSTÖGER, Ein Beitrag zur Anwendung und Visualisierung digitaler Geländemodelle, Wien, Dezember 1989.

Heft 35 R. WEBER, Lokale Schwerefeldmodellierung unter Berücksichtigung spektraler Methoden zur Geländereduktion, Wien, April 1990.

Heft 36 o.Prof. Dr. Hans Schmid zum 70. Geburtstag. Veröffentlichung der Abteilung für Landesvermessung, Wien, Oktober 1990.

Heft 37 G. GERSTBACH, H. P. HÖLLRIEGL und R. WEBER, Geowissenschaftliche Informationsbörse - Eine Nachlese zu GeoLIS II, Wien, Oktober 1990.

Heft 38 R. ECKER, Rastergraphische Visualisierungen mittels digitaler Geländemodelle, Wien, August 1991.

Heft 39 Kartographische Forschungen und Anwendungsorientierte Entwicklungen, herausgegeben von W. Stams und F. Kelnhofer zum 80. Geburtstag von Prof. Dr. W. Pillewizer, Wien, Juli 1991.

Heft 39a W. RIEGER, Hydrologische Anwendungen des digitalen Geländemodelles, Wien, Juli 1992.

Heft 40 K. STEINNOCHER, Methodische Erweiterungen der Landnutzungsklassifikation und Implementierung auf einem Transputernetzwerk, Wien, Juli 1994.

Heft 41 G. FORKERT, Die Lösung photogrammetrischer Orientierungs- und Rekonstruktionsaufgaben mittels allgemeiner kurvenförmiger Elemente, Wien, Juli 1994.

Heft 42 M. SCHÖNER, W. SCHÖNER, Photogrammetrische und glaziologische Untersuchungen am Gàsbre (Ergebnisse der Spitzbergenexpedition 1991), Wien, Mai 1996.

Heft 43 M. ROIC. Erfassung von nicht signalisierten 3D-Strukturen mit Videotheodoliten, Wien, April 1996.

Heft 44 G. RETSCHER, 3D-Gleiserfassung mit einem Multisensorsystem und linearen Filterverfahren, Wien, April 1996.

Heft 45 W. DAXINGER, Astrogravimetrische Geoidbestimmung für Ingenieurprojekte, Wien, Juli 1996.

Heft 46 M. PLONER, CCD-Astrometrie von Objekten des geostationären Ringes, Wien, November 1996.

Heft 47 Zum Gedenken an Karl Killian "Ingenieur" und "Geodät" 1903-1991, Veröffentlichung der Fachgruppe Geowissenschaften, Wien, Februar 1997.

Heft 48 A. SINDHUBER, Ergänzung und Fortführung eines digitalen Landschaftsmodelles mit multispektralen und hochauflösenden Fernerkundungsaufnahmen, Wien, Mai 1998.

Heft 49 W. WAGNER, Soil Moisture Retrieval from ERS Scatterometer Data, Wien, Dezember 1998.

Heft 50 R. WEBER, E. FRAGNER (Editoren),Prof. Bretterbauer, Festschrift zum 70. Geburtstag, Wien, Juli 1999.

Heft 51 Ch. ÖHRENEDER, A Similarity Measure for Global Image Matching Based on The Forward Modeling Principle, Wien, April 1999.

Heft 52 M. LECHTHALER, G. GARTNER, Per Aspera ad Astra, Festschrift für Fritz Kelnhofer zum 60. Geburtstag, Wien, Jänner 2000.

Heft 53 F. KELNHOFER, M. LECHTHALER, Interaktive Karten (Atlanten) und Multimedia – Applikationen, Wien, März 2000.

Heft 54 A. MISCHKE, Entwicklung eines Videotheodlit-Meßsystems zur automatischen Richtungsmessung von nicht signalisierten Objektpunkten, Wien, Mai 2000.

Heft 55 Veröffentlichung des I.P.F. anlässlich der Emeritierung von Prof. Dr. Peter Waldhäusl, Wien.

Heft 56 F. ROTTENSTEINER, Semi-automatic Extraction of Buildings Based on Hybrid Adjustment Using 3D Surface Models and Management of Building Data in a TIS, Wien, Juni 2001.

Heft 57 D. LEGENSTEIN, Objektrekonstruktion aus perspektiven Bildern unter Einbeziehung von Umrisslinien, Wien, Mai 2001.

Heft 58 F. KELNHOFER, M. LECHTHALER und K. BRUNNER (Hrsg.), Telekartographie und Location Based Services, Wien, Jänner 2002.

Heft 59 K. BRETTERBAUER, Die runde Erde eben dargestellt: Abbildungslehre und sphärische Kartennetzentwürfe, Wien, 2002.

Heft 60 G. GARTNER, Maps and the Internet 2002, Wien 2002.

Heft 61 L. DORFFNER, Erzeugung von qualitativ hochwertigen 3D Photomodellen für Internetbasierte Anwendungen mit besonderem Augenmerk auf Objekte der Nahbereichsphotogrammetrie, Wien, Jänner 2002.

Heft 62 K. CHMELINA, Wissensbasierte Analyse von Verschiebungsdaten im Tunnelbau, Wien 2002.

Heft 63 A. NIESSNER, Qualitative Deformationsanalase unter Ausnutzung der Farbinformation, Wien 2002.

Heft 64 K. BRETTERBAUER, R. WEBER, A Primer of Geodesy for GIS-Users, Wien 2003.

Heft 65 N. PFEIFER, 3D Terrain Models on the basis of a triangulation, Wien, Jänner 2002.

Heft 66 G. GARTNER (Hrsg), Lacation Based Services & Telecartography, Wien 2004.

Heft 67 I. KABASHI, Gleichzeitig-gegenseitige Zenitwinkelmessung über größere Entfernungen mit automatischen Zielsystemen, Wien 2004.

Heft 68 J. BÖHM, Troposphärische Laufzeitverzögerungen in der VLBI, Wien 2004.

Heft 69 R. WEBER, W. SCHLÜTER, U. SCHREIBER, O. TITOV Evolving Space Geodesy Techniques (EGS XXVII General Assembly, Nice, France, 2002), Wien 2004.

Heft 70 G. WEINWURM, Amalthea's Gravity Field and its Impact on a Spacecraft Trajectory, Wien 2004.

Heft 71 Forschungsgruppe Ingenieurgeodäsie, Festschrift anlässlich des 65. Geburtstages von Herrn o.Univ. Prof. Dr.-Ing. Heribert Kahmen, Wien 2005.

Heft 72 A. REITERER, A Knowledge-Based Decision System for an On-Line Video-Theodolite-Based Multisensor System, Wien 2005.

Heft 73 M. HABERLER, Einsatz von Fuzzy Methoden zur Detektion konsistenter Punktbewegungen, Wien 2005.

Heft 74 G. GARTNER, Location Based Services & Telecartography, Proceedings of the Symposium 2005, Wien 2005.

Heft 75 Th. HOBIGER, VLBI as a tool to probe the ionosphere, Wien 2006.

Heft 76 E. KLAFFENBÖCK, Troposphärische Laufzeitverzögerung von GNSS-Signalen – Nutzen aktiver Referenzstationsnetze für die Meteorologie, Wien 2006.

Heft 76a P. J. MENDES-CERVEIRA, Tidal and non-tidal contributions to surface loading processes on station coordinates, Wien 2006.

Heft 78 G. KOSTOV, G. BOURDA, L. FERNANDEZ, T. KONDO, Research Projects at IGG Reports, Wien 2007.

Heft 79 J. BÖHM, A. PANY, H. SCHUH (Editors), Proceedings of the 18th European VLBI for Geodesy and Astrometry Working Meeting, 12-13 April 2007, Wien 2007.

Heft 80 J. BÖHM, Tropospheric Delay Modelling at Radio Wavelengths for Space Geodetic Techniques, Wien 2007.

Heft 81 G. Retscher, Mobile Multi-sensor Systems for Personal Navigation and Location-based Services, Wien 2007.

Heft 82 R. HEINKELMANN, Bestimmung des atmosphärischen Wasserdampfes mittels VLBI als Beitrag zur Klimaforschung, Wien 2008.

Heft 83 F. ROTTENSTEINER, Automatic extraction of buildings from airborne laserscanner data and aerial images, Wien 2008.

Heft 84 S. TODOROVA, Kombination geodätischer Weltraumverfahren für globale Karten der Ionosphäre, Wien 2009.

Heft 85 J. WRESNIK, Simulationen für die neue Generation von VLBI-Systemen, Wien 2009.

Heft 86 A. KARABATIC, Precise Point Positioning (PPP). An alternative technique for ground based GNSS troposphere monitoring, Wien 2011.

Heft 87 K. TEKE, Sub-daily Parameter Estimation in VLBI Data Analysis, Wien 2011.

Heft 88 G. THALER, Echtzeit Bahn- und Uhrberechnung der GPS-Satellitenkonstellation basierend auf Beobachtungsdaten des RTIGS-Stationsnetzwerkes, Wien.

Heft 89 P. SWATSCHINA, Dynamic and Reduced-Dynamic Precise Orbit Determination of Satellites in Low Earth Orbits, Wien 2012.

Heft 90 S. BÖHM, Tidal excitation of Earth rotation observed by VLBI and GNSS, Wien 2012.

Heft 91 H. KRÁSNÁ, Estimation of solid Earth tidal parameters and FCN with VLBI, Wien 2013.

Heft 92 J. SUN, VLBI scheduling strategies with respect to VLBI2010, Wien 2013.

Heft 93 M.M. ALIZADEH ELIZEI, Multi-Dimensional modeling of the ionospheric parameters, using space geodetic techniques, Wien 2013.

Heft 94 M. KARBON, Atmospheric effects on measurements of the Earth gravity field, Wien 2013.